ION BEAM ANALYSIS OF GEOMETRICALLY STRUCTURED SAMPLES

David Jezeršek

Doctoral Dissertation
Jožef Stefan International Postgraduate School
Ljubljana, Slovenia, August 2011

Evaluation Board:

Dr. Christopher Jeynes, Member, *University of Surrey, Surrey Ion Beam Centre*

Doc. Dr. Primož Pelicon, Member, *Jožef Stefan Institute, Jamova cesta 39, 1000 Ljubljana*

Doc. Dr. Matjaž Žitnik, Member, *Jožef Stefan Institute, Jamova cesta 39, 1000 Ljubljana*

MEDNARODNA PODIPLOMSKA ŠOLA JOŽEFA STEFANA
JOŽEF STEFAN INTERNATIONAL POSTGRADUATE SCHOOL

David Jezeršek

ION BEAM ANALYSIS OF GEOMETRICALLY STRUCTURED SAMPLES

Doctoral Dissertation

ANALIZA GEOMETRIJSKO STRUKTURIRANIH VZORCEV Z IONSKIM ŽARKOM

Doktorska disertacija

Supervisor: Prof. Dr. Žiga Šmit

Ljubljana, Slovenia, August 2011

Index

1 Introduction 1

2 Theoretical introduction, review of experimental methods 7
2.1 Interactions of ions with matter 7
2.1.1 Energy loss and stopping cross-sections 7
2.2 Rutherford backscattering - RBS 8
2.2.1 Depth distribution of scattering 10
2.2.2 Scattering cross-sections 11
2.2.3 Thin and thick target spectrum 13
2.2.4 Analysis of the spectra 16
2.2.5 The scattering angle 16
2.2.6 The units of thickness 18
2.3 Construction of BS experimental setup 18
2.3.1 The helium flux 19
2.3.2 Distance to the target 20
2.3.3 Micro-positioning system 21
2.3.4 Measurement of proton current number 22
2.3.5 The wire-mesh-based charge-collecting device 23
2.3.6 The chopper method 24
2.4 X-Ray emission based methods 27
2.5 The PIXE method 30
2.5.1 The PIXE yield 30
2.5.2 The thick target model 31
2.5.3 Cross-sections for X-ray production 34
2.5.4 The model of a cylindrical target 35
2.5.5 Evaluation of the geometry impact 36
2.5.6 The beam profile 39
2.5.7 Measurement of the beam profile with a metal wire 41
2.5.8 Cylindrical target in a Gaussian-type beam 44
2.5.9 The determination of the instrumental constant *H* 45
2.5.9.1 *H* value calibration at the University of Surrey 45
2.5.9.2 *H* value calibration at the Jožef Stefan Institute 47
2.5.10 The PIXE experimental setup 48
2.5.11 The PIXE measurement uncertainty 50
2.5.12 Reproducibility 52

3 Development of measuring equipment and procedures 53
3.1 Measurements of textile fibres 53
3.1.1 The textile fibre samples 53
3.1.2 PIGE measurements of textile fibres 62
3.1.3 The silicon anomaly 66

3.1.4 White PES fibres 67
3.1.5 Teflon-treated fibres 68
3.1.6 Nano-silver-treated fibres 69
3.1.7 Microbeam mapping of textile fibres 70
3.2 RBS measurements 76
3.2.1 Nuclear scattering cross-sections 76
3.2.2 Calibration of the RBS system 79
3.2.2.1 Beam Energy 79
3.2.2.2 The scattering angle 80
3.2.2.3 The foil in SIMNRA 80
3.2.2.4 Energy calibration with a set of thick targets 80
3.2.2.5 Dose calibration with a set of thick targets 81
3.2.3 The samples for RBS measurements 82
3.2.4 Results of BS measurements of representative samples 82

4 Conclusions 87

5 References 89

V prvi vrsti bi se rad zahvalil mentorju, prof. dr. Žigu Šmitu, za zaupanje in velikodušno potrpežljivost pri procesu izdelave te doktorske naloge.

Za stimulativno okolje, v katerem je bilo veselje delati, gre zahvala vsem sodelavcem Mikroanalitskega centra, Odseka za fiziko nizkih in srednjih energij Instituta "Jožef Stefan". Posebna zahvala gre v obeh pomenih najbližjim sodelavcem Nataši Grlj, dr. Sabini Markelj in doc. dr. Matjažu Kavčiču.

Vodju pospeševalnika doc. dr. Primožu Peliconu hvala za nesebično pomoč, dragocene nasvete in življenjske nauke.

Hvala Franzu Gasserju za pomoč pri projektiranju komore za normalizacijo.

A big thanks goes to dr. Melanie Bailey, who invited me to make the measurements at the Ion Beam Centre at the University of Surrey, and to the SPIRIT consortium that made the measurements financially viable.

I am very grateful to dr. Christopher Jeynes for accepting the task of being a member of the evaluation board and for all the stimulating conversations we had at various meetings and conferences.

Thanks to Paul McGuiness for proofreading the text and correcting all the misplaced articles.

Hvala Ministrstvu za visoko šolstvo, znanost in tehnologijo za financiranje v okviru programa mladih raziskovalcev.

Nenazadnje gre zahvala vsem domačim, staršema, bratu Blažu in bratu Alešu z družino za podporo in spodbudo, brez katere bi bilo težko.

Abstract

An experimental set-up for the detection of scattered projectile ions was constructed at the external (in air) beamline of the Microanalytical Center at the Jožef Stefan Institute. The system is composed of a detector for the analysis of back-scattered projectiles, casually called the RBS detector, a precise positioning system and a meter of impact charge. The RBS detector was placed in a prototype holder made of aluminium with a constant He flush to reduce stopping of the back-scattered protons. The precise proton dose measurement was accomplished with the implementation of an in-vacuum wire-mesh based charge-collecting device. For a possible future implementation of an external micro-beam, an in-vacuum ion-beam chopper device with an RBS detector was constructed. The precise positioning system composed of a laser fixed on a XYZ micro-positioning stage and a camera was utilized to achieve reproducible positioning with a precision of better than 100 μm. Calibration on thick targets was performed at the newly developed RBS setup. A set of representative samples were analysed, some of historical and archaeological value. The experimental setup at this stage was found to be a suitable candidate for the transfer to a digital acquisition system enabling the simultaneous acquisition of two PIXE, one RBS and a PIGE spectrum at high count-rates.

The analysis of geometrically structured samples in particular of cylindrical geometry, has been somehow neglected in the past, probably because of mathematical difficulties in the calculation of matrix effects. A mathematical model for an accurate calculation of X-ray yields induced in cylindrical targets is proposed and the results are compared to more routinely used models that can be applied in commercially available software packages. The light elements emitting fluorescence soft X-rays are in particular affected. A set of measurements was performed on fibres containing detectable elements from Si up, with the proposed mathematical model.

The achievements were published in two articles.

Povzetek

V doktorskem delu je bil izdelan spektroskopski sistem za analizo plastovitih vzorcev z elastičnim povratnim sipanjem. Sistem predstavlja nadgradnjo eksperimentalne postaje žarkovne linije z ionskim žarkom v zraku na Mikroanalitskem centru Instituta Jožef Stefan. Najpomembnejši deli sistema so merilec povratno sipanih ionov, ki ga običajno imenujemo kar RBS detektor, sistem za natančno nastavitev vzorca in merilec števila vpadnih protonov. Detektor je vgrajen v prototipni nosilec, narejen iz aluminija, ki omogoča konstanten pretok plina, v našem primeru helija, kar zmanjša ustavljanje povratno sipanih protonov na poti do detektorja. Natančen način meritve protonske doze je bil izveden z vgraditvijo kovinske mrežice za nabiranje naboja v vakuumu. Za možnost nadgradnje žarka v zunanji mikrožarek smo poskrbeli z izdelavo prekinjevalca ionskega žarka v vakuumu z RBS detektorjem. Natančen sistem za postavitev vzorca, ki omogoča postavitev z natančnostjo, boljšo od 100 μm, sestavljata: laser, pritrjen na mikropozicijsko mizico, premično v treh pravokotnih smereh, in kamera, povezana na računalnik. Umeritev novega sistema je bila izvedena z debelimi tarčami. Delovanje sistema smo potrdili z analizo plastovitih vzorcev, med katerimi so bili tudi predmeti zgodovinskega in arheološkega pomena. Eksperimentalna postaja v sedanjem stanju je primeren kandidat za prehod na digitalni zajem signala, ki bo omogočal sočasen zajem spektrov iz dveh PIXE, enega RBS in enega PIGE detektorja pri velikih hitrostih štetja.

Analiza geometrijsko strukturiranih vzorcev, predvsem vzorcev s cilindrično geometrijo, je bila v preteklosti nekoliko zanemarjena, zelo verjetno zaradi težav pri računanju matričnih učinkov. V disertaciji je predlagan matematični model za pravilen izračun pridelka rentgenskih žarkov pri meritvah tarč z valjasto geometrijo. Rezultat analize smo kritično primerjali z rezultatom analize s komercialno dostopnimi programskimi paketi. Še posebej močan vpliv geometrije je zaznati pri lahkih elementih, ki oddajajo fluorescenčne rentgenske žarke nizkih energij. S predlaganim matematičnim modelom smo opravili meritve tekstilnih vlaken, ki vsebujejo merljive primesi, težje od silicija.

Dosežki so bili objavljeni v dveh člankih.

Abbreviations

List of selected abbreviations used in the thesis in order of appearance:

IBA - Ion-beam analysis
PIXE - Particle-induced X-ray emission
MS - mass spectrometry
BS - back scattering
EBS - elastic back scattering
RBS - Rutherford backscattering
ERDA - Elastic recoiled detection analysis
PIGE - Particle-induced gamma-ray emission
XRF - X-ray fluorescence
ECPSSR (model) - A successful correction of a Plane wave Born approximation (PWBA)
IBANDL - Ion Beam Analysis Nuclear Data Library
EXFOR - A database of Experimental Nuclear Reaction Data, available online at the website maintained by IAEA (http://www-nds.iaea.org/exfor/)
IAEA - International Atomic Energy Agency
SIMNRA - A sowftware program for RBS spectrum simulation
MIC - Microanalytical Center at Jožef Stefan Institute (JSI) in Slovenia
JSI - Jožef Stefan Institute, largest scientific institute in Slovenia
XRF - X-ray fluorescence, a technique for elemental analysis, employing the high energy X-rays for ionisation of target atoms.
SEM - Scanning electron microscope
SEM-EDS - Scanning electron microscope based technique for elemental analysis employing energy-dispersive X-ray spectroscopy
NDF - Nuclear Data Furnace, a software package capable of fitting multiple
DEPTH, GISA, MCERD, RBX, RUMP, SIMNRA - programs for RBS spectrum simulation
SRIM - The stopping and range of ions in matter
PIPS (detector) - Passivated implanted planar silicon (detector)
TPI - Threads per inch (unit of threads density)
SEM - Scanning electron microscope
AGLAE - Accélerateur Grand Louvre d'Analyse Elémentaire in Paris, France
IBC - Ion Beam Centre at University of Surrey
SPIRIT - Support of public and industrial research using ion beam technology
GM (tube) - Geiger-Müller tube
PWBA- Plane wave Born approximation
ECPSSR (theory) - A successful correction of a PWBA
GUPIX - software for PIXE spectra analysis, written by Guelph PIXE group
LN - Liquid nitrogen - used for cooling of X-ray and gamma-ray detectors
NIST - National Institute of Standards and Technology

NIM - Nuclear instrumentation module
MCA - Multi channel analyzer
MS-DOS - Microsoft disk operating system - very common computer operation system
PES - Polyester - polymer from which some artificial textile fibres are produced
FWHM - Full width at half maximum - measure of a peak width
HVEE - High voltage engineering Europa - a producer of ion-beam accelerators
NRA - Nuclear reaction analysis

1 Introduction

Ion-beam analysis (IBA) is a set of analytical methods that can be used on a variety of objects – from the constituents of a living cell employing proton microbeams [1] from electrostatic accelerators, to the composition of minerals on Mars, excited by particles and photons from radioactive sources [2, 3]. In this work we study the use of IBA on geometrically structured targets that are important in the analysis of historical artefacts and in forensics.

The elemental analysis of materials at electrostatic accelerators is made by measuring the X-rays induced in a target. The spectrum of measured X-rays contains characteristic peaks, from which the concentrations of elements in a target can be extracted. This technique is called particle-induced X-ray emission (PIXE) and it is the most often used IBA technique. However, the geometry of a target has a strong influence on the results of the PIXE analysis and requires a special evaluation. In the scope of this work we measured cylindrical targets with an ion-beam of millimetre dimensions. However, when we use a common mathematical model of intermediate thick target [4] for the evaluation of these results, we can make a huge error. We propose a new mathematical model for the calculation of the PIXE concentrations obtained by a milli-beam on cylindrical targets. The need for the new model, especially for light elements, was demonstrated with a calculation on imaginary sample, containing trace elements in a light organic matrix and micro-PIXE mapping measurements. When a new mathematical model is used we can also expect better agreement with the results obtained by absolute methods like mass spectrometry (MS).

Together with PIXE we often also measure the energy spectra of backscattered projectiles (BS, EBS, RBS), or of target atoms elastically recoiled in a forward direction (ERDA). For the PIXE analysis a 3-MeV proton beam is commonly used, since it gives an optimal signal-to-noise ratio, thus presenting the best available sensitivity [5]. At this energy the particle scattering is non-Rutherford for light target elements [6], which means that experimental or evaluated cross-sections have to be used for the particle scattering spectrum evaluation.

Most of ion-beam analysis can be done also in-air. Easy handling of large and sensitive objects is possible at the external beamline. The samples can be changed fast and the impact on the target is relatively small. The PIXE and EBS measurements do not consume the target as some other analytical techniques do (mass spectrometry or gas chromatography); on the other hand, the projectile ions have an energy high enough to ionize atoms and break molecular bonds, thus breaking the structure of organic materials. Special care to minimize the irradiation dose has to be taken when measuring precious organic samples (e.g. old and unique paintings, parchments, ...)

Hitting the light-element atoms with light projectiles, most commonly protons, of high energy (few MeV), triggers nuclear excitation effects due to the weaker Coulomb field of the light-element nucleus. The nuclear excitation in some cases causes the emission of gamma-rays. The analytical technique employing this phenomenon is called particle-induced gamma-ray emission (PIGE) and can be used as a complementary technique with PIXE for light-elements detection.

The three IBA methods that are described in this work have to comply with four requirements to obtain a trustworthy quantitative result:

- *A measurement of a quantity proportional to the projectile dose*. The critical parameter is a product between charge and solid angle, but when the solid angle is kept constant, the projectile dose (charge) is the parameter which has to be measured. The exception is a sample with an internal standard, and a PIXE measurement where RBS is used for the determination of the projectile dose [7].
- *A stable and well defined experimental setup*. The stable (precision) as well as well defined (accuracy) setup has to be known to determine the absolute uncertainty of the results.
- *A suitable mathematical model* to simulate the measured particle or photon yield at a given sample geometry. The mathematical model for a certain geometry is important with the PIXE method, where X-ray absorption in the material is not negligible, as it is with the PIGE method.
- *A well defined cross-section or a measurement of a standardized reference material*. The *X-ray production cross-sections* are calculated according to semi classical and quantum mechanical models, which give rather good results. With PIGE the gamma-ray production cross-sections are not very well known, so we use measured yields of samples with known composition (*standardized reference materials*). The particle spectra typically are non-Rutherford, so the experimental or evaluated *particle scattering cross-sections* have to be used.

Two methods of measuring projectile dose will be described in this work: the wire-mesh charge-collecting device and a chopper-based normalization device (these were published in 2010 [8]). The measured X-ray yield is corrected for the amount of projectiles hitting the target.

The precise geometry of the experimental setup is of great importance. The distance from the exit window to the sample, from the sample to the detector, the filters in front of the detector and their thickness, the composition of the atmosphere (air or He) between the exit foil and the sample, the angle of the detector, the scattering angle for the RBS measurements, the energy and energy spread of the beam: all these parameters greatly influence the result, so they have to be kept in tight tolerances to assure the precision of the measurements. Accuracy of the measurements is achieved by measuring standardized reference materials.

The geometrical effects of a sample with some IBA techniques are more important than with others. With PIXE, the X-ray yield that we measure depends strongly upon the geometry. The curvature of the surface changes the absorption of the induced X-rays in the sample matrix, resulting in a higher or lower X-ray yield (depending on the position of the beam) within the geometrically structured samples (fibres, wires, spheres). For an accurate quantitative result, a mathematical model for a correct type of sample and of the sample orientation should be introduced. The model should include parameters, such as the beam energy, the width and the shape, the geometry of the sample, the energy of the characteristic X-rays and their absorption in the sample. The error caused by using the wrong mathematical model can be significant, we will show that for the most inappropriate set of parameters it may reach 100%.

Another requirement is a well defined cross-section for the X-ray production (PIXE). The cross-sections are commonly calculated according to the ECPSSR model [9], an efficient correction of a plane wave Born approximation. There are several codes for the calculation of the ECPSSR cross-sections, like that of Šmit [10] or Liu and Cipolla [11]; we use the former one. For the purpose of estimating the geometry effect to the

evaluation, which is the main subject of this work, the X-ray production cross-section data is not crucial, since it is the same for each evaluation. Also, the uncertainty of cross-sections compared to geometrical effects is small enough, so no cross-section measurements will be necessary for the purpose of this thesis.

With back-scattered-particle spectra the non-Rutherford scattering cross-sections should be taken into account. The results of measurements of many thick mono-elemental targets are compiled in the databases IBANDL [12] and EXFOR [13]. Gurbich in 2007 published a tool called SigmaCalc [14] to calculate the cross-section data at a selected scattering angle. The output of SigmaCalc [15] is a particle-scattering graph relative to the Rutherford scattering, which can be imported in programs for simulating the scattering spectra, like SIMNRA. With the availability of the SigmaCalc tool online, the evaluation of non-Rutherford particle scattering spectra became much easier a task.

In our study we concentrated on the measurement of layered samples as well as on the measurements of textile fibres of cylindrical geometry.

Layered structures are very common in archaeologically relevant samples. Layers of paint on ceramics [16], or gilded artefacts [17] are often investigated. Other examples of thin metal layers may be silvered or tinned brass, bronze or iron [17]. Glaze, a thin layer of glass, has been used in artistic or common objects for thousands of years [18]. More recently, modern deposition techniques enable the production of sub-micrometer layers and multilayered composites [19]. So the challenges of measuring layered structures and correctly interpreting the results are now as relevant as ever in all kinds of applications. The samples with a layered structure can be analyzed with PIXE for their composition, but the information on the structure can be more easily obtained by measuring the back-scattered projectiles (BS). There were studies of layered samples performed by PIXE alone, where a beam energy of successive measurements was varying, to obtain different projectile penetration depths, thus probing the target at different depths. Earliest reference reaches back to 1972 [20]. This technique was later named the differential PIXE analysis technique [21, 22]. A similar technique for depth-profile determination, employing repeated measurements in the same spot at different impact angles, was proposed by Pabst in 1974 [23]. The technique was later revisited among others by Weber *et al.* [24-26]. An improved depth resolution with the same ion-beam can be achieved by a measurement of the back-scattered ions. The BS measurements in combination with PIXE gives us complementary information on the surface structure, the possible layered structure and also the surface roughness, so a combination of both techniques was shown to be a very suitable tool for the analysis of cultural heritage objects [27-30]. The self-consistent analyses using the BS and PIXE data were neatly done on various targets [31-33] using the DataFurnace simulated annealing [34], representing a major step forward in IBA.

Measurement of cultural heritage objects is one of the main applications at the external beamline setup at the Microanalytical Center (MIC) of the Jožef Stefan Institute in Ljubljana, Slovenia; however, a number of successful measurements were made at MIC in the field of archaeology, conservation and restoration, art and even forensics.

PIXE was used for the analysis of prehistoric stone tools [35, 36]. It was possible to detect elements characteristic for the materials worked by the tools and thus to identify them; typically it was possible to distinguish between cutting bone, wood and soft tissues. PIXE in air was further used for the wide characterization of metals. Gold objects can be measured without preparation [37]; in our work we showed which objects from a 9th century grave belong to the same workmanship. Objects from copper-based alloys have to be prepared for the measurement, carefully removing a few square millimeters of patina [38]. A large number of measurements of this type were made on Roman military equipment [39]; the analysis involves such fine items as the medallion of Augustus [40].

Its core metal is a base lead-silver alloy which was silvered in the front. The detection of brass in scabbard fittings [41] implied a more concise study of brooches, which demonstrated that brass was intensively used in the Roman world after 60 BC [42]. The non-destructive character of PIXE measurements is particularly important for coin analysis, either in combination with XRF for the study of the 3rd century BC coins from Albania [43], or for a systematic study of medieval silver coinage from the territory of Slovenia [44]. The measurements confirmed the historical supposition that silver from today's Carinthia was commercially spread towards east.

PIXE easily identifies plated material; using differential measurements it is possible to detect the plated layer thickness and concentration profiles. For gilding, the presence of mercury reveals the technique of fire gilding [17]. The same measuring technique can be applied to paint layers, though some additional information on the light-element concentration is required [45].

Due to its multi-elemental aspect, PIXE can be successfully applied for the analysis of glass; however, PIGE has to be used for the detection of light elements between sodium and silicon. Sorted by historic periods, the analysis involved glass from the Carolingian period in Slovenia [46] and glass made in the Venetian manner [47, 48, 49, 50] and afterwards [51]. The measurements identified the type of flux necessary for glass production, and several trace elements present as impurities.

PIXE and PIGE are not the most appropriate methods for the analysis of ceramic unless it is homogenized. An exception is cream-colored ceramics produced from a fine white clay since the 18th century. For the ceramics made in Northern Italy and Slovenia it was possible to distinguish between different producers [52].

Analysis by PIXE can be done on modest quantities of materials, so it can be used for determining the composition of iron-gall ink, which acts devastatingly on ancient paper materials [53-58]. In a similar way, it was used for the analysis of the hair of Duke Mirko Petrovič-Njegoš [59], finding the trace elements.

Limited measurements were also performed on textiles: the fragments of lace from Valvasor's tomb were analyzed by PIXE [60, 61], and recently we made a PIXE analysis of textile fibres, which forms the basis of the present work [62].

Objects of nature can also be analyzed by ion-beams. It is possible to follow the elemental variation in the stalagmite growth [63], and to determine the mineral species in meteorites. In a meteorite fallen recently in Slovenia we were able to determine the mineral composition of chondrules, characteristic globular structures formed during the meteorite's (re)crystallization [64].

To continue the tradition of in-air IBA measurements, the instrumentation should keep up with similar laboratories around the world. With this in mind we started an upgrade of the beamline, to accommodate a detector of back-scattered ions. Some BS spectra of layered samples were recorded, providing information on the sample's structure (thickness of the top layers and their roughness) in addition to the composition obtained by a PIXE measurement. A report on the experimental setup used for the BS measurements is presented in the paper [8].

Another extensive field of analyses, possible to perform with an ion-beam in air or in vacuum, is the analysis of textile fibres. The analyses of such samples are very relevant to forensics since much crime scene-investigation evidence consists of fibres. It is recognized that "textile fibres are among the most neglected and undervalued kinds of forensic evidence" [65]. For use in forensics the analysis should be non-destructive, so ion-beam analyses seem to be a promising candidate for these kinds of applications. The ion beams used are typically up to a few millimetres in diameter and penetrate up to 0.1 mm in depth, which results in less than 1 mm^3 of analyzed volume, implying only a

relatively small sample is required for the analysis. The ion-beam analysis techniques, more precisely PIXE, were used for the analysis of textiles only on a few occasions [61, 66, 67]. The scanning electron microscope (SEM) offers a good tool for the identification of textile fibres due to high magnification imaging and an additional elemental analysis [68]; however, compared to SEM-EDS elemental analysis, PIXE features a much higher sensitivity, possibly enabling the measurement of trace elements in fibres. A successful set of trial measurements, indicating a good potential for use in forensic science, was performed on a gunshot-residue sample [69]. The results showed a much higher sensitivity for the trace elements with PIXE than with the conventional SEM-EDS, but the precise quantification is hard due to the geometrical effects [33]. The geometrical effects are also responsible for the difficulties in the quantification of textile fibre measurements. An additional discriminating power could be achieved with PIXE's higher sensitivity to trace elements in textiles; however, for the quantification the geometrical effect should also be taken into account.

The diameters of textile fibres are typically in the range from 50 µm to 500 µm. They are composed of many fibrils, also called monofilaments, with a diameter of 5-50 µm weaved together in a single fibre or a thread. The closest approximation of a thread's geometry is a cylinder. As shown in this work, the quantitative results of a PIXE measurement of a sample with such a geometry are different from the results obtained with a model of a planar intermediately thick target, commonly used in PIXE-evaluation programs (Gupix [70], NDF [71, 72]). This result particularly concerns the measurement of light elements in cylindrical samples with diameters similar to the range of characteristic X-rays. Also, the orientation of the fibre to the beam and the detector axis is important. Thinking about the influential parameters, PIXE measurements of light elements in human hair might be substantially affected by its geometry.

Objects, geometrically similar to fibres, are human hair, for which several experimental and methodological studies exist. Trace elements in hair may reveal biological or environmental impacts on human life [73, 74], such as the influence of life habits, (tobacco smokers [75]), working conditions (exposition of workers to GaAs [76]) or historical events like the potential poisoning of Duke Petrovič [59].

In earlier papers the evaluation of concentrations were rather primitive assuming hair as a thick target, composed of numerous thin layers [76]. A realistic hair shape was considered in the works of Montenegro [77] and Li Hong-Kou [78-80]. Montenegro introduced a correction factor taking into account proton stopping along its trajectory and X-ray attenuation; however, these two effects were estimated using the power approximations for proton stopping power and ionization cross-sections, at that time commonly in use. The correction factors of Li [78] are more refined and include the effects of inhomogeneous elemental distribution, irregular hair shape and different mass density. He also calculated the correction factors for the surface, uniform and central distribution of elements [80]. Measurements were performed for two hair fibres at different impact energies. The variation of X-ray yields was found characteristic for the element distribution. The actual distribution was measured by microbeam mapping, conforming the surface distribution of lead and chlorine and the uniform distribution of sulphur. Li also combined PIXE and RBS, using the latter method to determine the hair diameter [79]. RBS has already been used earlier to determine the irradiated hair mass in PIXE [81]. A detailed elemental distribution in hair is typically obtained by microbeams, scanning the cross-section [82] or analyzing particular hair parts such as follicles [83]. Low concentration levels can be achieved by the complementary use of sensitive chemical methods, such as INAA and STIM [82] or ICP-MS. In our work we expect to obtain better agreement with different analytical results using a dedicated mathematical model for the matrix effects in a fibre, avoiding analytical approximations. The results

that we developed for cylindrical targets are published in the paper [62].

2 Theoretical introduction, review of experimental methods

Fast ions interact with matter in different ways, and the resulting products leaving the target may be used for a number of analytical methods. It is important to understand how the ions interact with matter. Possible methods of analysis that emerge from the interaction phenomena will be discussed. Afterwards each of the methods will be described in detail including the physical background of the method, calculations and an overview of the recent development of the method.

2.1 Interactions of ions with matter

Positive ions with a few MeV energy penetrate the material. Along their paths they interact with electrons and elastically scatter from the nuclei. Electrons bound to the target atoms get a sufficient amount of energy to leave the atom, so the atoms are being ionized. An ion penetrating the material loses its energy in collisions with electrons, thus ionizing the atoms. Each atom which is ionized produces either an X-ray photon or an Auger electron, when a vacancy in the inner electron shell is filled with an electron from the outer shell. What we can detect from this interaction, is X-rays or Auger electrons that are characteristic of a target atom.

A projectile ion can hit the nucleus of a target atom. In this case two things can happen. If the Coulomb barrier around the nucleus is strong (high Z elements), the projectile ion elastically scatters in a different direction, depending on the impact parameter. The first man to observe the scattering of ions in the backward direction was Sir Ernest Rutherford in 1911. The phenomenon is, as a result, called Rutherford backscattering (RBS). These scattered ions can be detected by the particle detector and the spectrum of detected particles as a function of energy is obtained. The art of analysing these spectra has, over the years, developed into a successful analytical technique.

If the Coulomb barrier around the nucleus is not high enough (low Z elements), projectile ions may penetrate it and perturb the nucleus. Two events may result, a nuclear reaction between the projectile and target nucleus or gamma radiation emitted from the nucleus of the target atom.

2.1.1 Energy loss and stopping cross-sections

Knowledge about the deceleration of ions when penetrating matter is of key importance in ion-beam-based atomic spectroscopic methods. Loss of energy is directly related to probing depth and affects both qualitative and quantitative analyses. The physics of energy-loss phenomena is very complex and involves many kinds of interactions between the projectile ion, the electron and the nucleus of the target atom. These interactions have been subject to intense studies for the last century due to their significance in many fields of physics.

The theoretical treatment has been reviewed [84], among many others, by Bohr (1948), Whaling (1958), Fano (1963), Jackson (1962 and 1975), Bichsel(1970), Sigmund (1975),

Ahlen (1980), Littmark and Ziegler (1980), Ziegler (1977, 1980), and in 1985 the program package for calculations of stopping powers and ranges SRIM was developed by Ziegler *et al.* [85].
The experimental methods have been reviewed and investigated by, *e.g.*, Chu [86], Bauer [87], Mertens [88], Powers [89], Paul [90].

The number of experimental studies of ion energy loss is high. This data on ion stopping and ranges are collected in a number of compilations, the most recent and the most commonly used is collected and maintained by Ziegler et. al. and published in a package called "The Stopping and Range of Ions in Matter" (SRIM); at the time of writing SRIM2010 was available online [91], containing over 28000 stopping values with more than 700 scientific citations which are made to SRIM every year [92]. A very widely used version of SRIM was 2003 [93], receiving by now over 400 citations [94].

The relative importance of various interaction processes between the ions and target medium depend mostly on the ion velocity and on the charges of the ion and target atoms. At ion velocities v, significantly lower than the Bohr velocity v_0 of the atomic electrons, the ion carries its electrons and tends to become neutralized by electron capture. At these velocities elastic collisions with the target nuclei, i.e., the nuclear energy loss, dominates.

As the ion velocity is increased the nuclear energy loss diminishes as $1/E$, where E is the energy of the ion. The electronic energy loss, i.e., inelastic collisions with the atomic electrons, soon becomes the main interaction. The total energy loss is obtained as a sum of the nuclear and electronic contributions. In the ion velocity range from $v \sim 0.1 v_0$ to $Z_1^{2/3} v_0$, the electronic energy loss is approximately proportional to the velocity, or $E^{1/2}$. At higher velocities $v >> v_0$ the charge state of the ion increases and finally it becomes fully stripped of its electrons. At a given velocity the energy loss is proportional to the square of the ion charge. The theoretical framework of the energy loss of high-velocity ions originates from the works of Bohr, Bethe and Bloch [84]. The Bethe-Bloch formula has the general form:

$$dE/dx = N Z_2 \left(Z_1 e^2\right)^2 f\left(E / M_1\right), \qquad (1)$$

where e is the electron charge and $f(E/M_1)$ is a function depending on the target, but not on the type of the projectile.

2.2 Rutherford backscattering - RBS

Rutherford backscattering had a major impact on the development of physics. In the year 1911 E. Rutherford showed that the scattering cross-section depends on the scattering angle as $\sin^{-4}\vartheta/2$ [95]. This angular dependence means that all the positive charge is located in a small nucleus. Today, RBS is a spectroscopic method with which we measure the composition and thickness of thin layers. Two phenomena are important here [95]:

a.) The energy of scattered ions depends upon the mass of the atoms in the target. With the energy of the scattered ions we study the composition of a sample in a similar way as with mass spectroscopy.
b.) Ions in the target are slowing down, so we can calculate how deep in the target they scattered back to the detector.

The collision of an ion and an atom can be regarded as an elastic collision in classical

mechanics, since the bonding energy in a crystal lattice is negligible compared to the energy of the collision. For an elastic collision we can assume the conservation of linear momentum and the conservation of kinetic energy. A characteristic parameter of the collision is the scattering angle, which is constant for a certain detector setup. The energy of a projectile E_1 after the collision is lower by the kinematical factor k [96].

$$E_1 = k \cdot E_0 . \tag{2}$$

$$k = \left(\frac{\sqrt{m_2^2 - m_1^2 (\sin \vartheta)^2} + m_1 \cos \vartheta}{m_1 + m_2} \right)^2 . \tag{3}$$

At the set masses m_1 and m_2, k is highest in the backward direction (ϑ=π):

$$k = \left(\frac{m_2 - m_1}{m_2 + m_1} \right)^2 . \tag{4}$$

In the limit, when m_2>>m_1 the k factor is 1. This means that for any scattering angle the energy of a projectile after the collision is the same as the energy before the collision.

For mass analysis it is important that the energies of the ions scattered from atoms with different masses differ as much as possible. With the set Δm_2 the scattered energy differs by:

$$\Delta E = E_0 \left(\frac{dK}{dm_2} \right) \Delta m_2 = E_0 \frac{4 m_1 (m_2 - m_1)}{(m_1 + m_2)^3} \Delta m_2 . \tag{5}$$

From here we get the mass resolution at ϑ=π:

$$\Delta m_2 = \frac{\Delta E}{E_0} \frac{(m_1 + m_2)^3}{4 m_1 (m_2 - m_1)} . \tag{6}$$

We get a good mass resolution with a good energy resolution of the detector (low ΔE), with a high enough energy of the projectiles (E_0) and with the right choice of the projectiles. The second factor in Eqn (6) is minimal at m_2=2m_1. So with protons we get a good resolution for light elements, however with the use of chlorine projectiles (m_1=35) we get the best resolution for atoms around gallium (m_2=70). The experimental conditions are more complicated, since with the use of heavier projectiles we get a worse detector resolution for scattered ions. The typical resolution of a surface barrier detector for alpha particles is 15 keV, with heavier ions it goes to a few tens of keV. For an example of alpha particle with an energy of 1 MeV, the mass resolution for m_2=16 is 0.63 mass units and with m_2=100 the mass resolution increases to 11 mass units [95].

2.2.1 Depth distribution of scattering

The relation $E_1 = k \cdot E_0$ can be used just for collisions on the surface of the sample. If the collision takes place deeper in the sample the ion loses a part of its energy along its path to the atom and part along the path back to the detector. A useful estimation of the energy shift $\Delta E = kE_0 - E(\mathrm{h})$ is obtained if we only partially consider the energy dependence of the stopping power dE/dx [96].

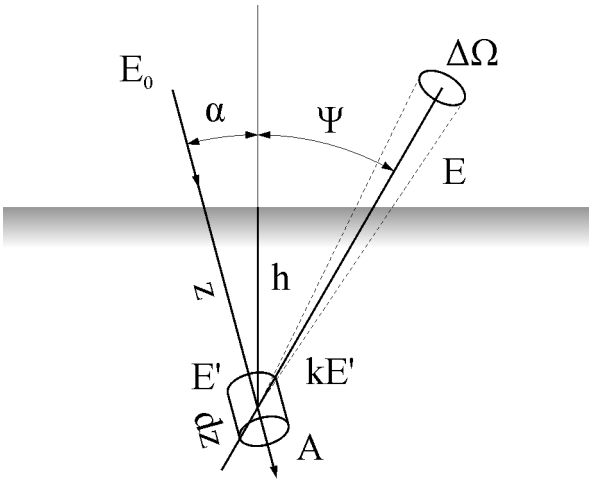

Figure 1: *The scattering geometry of Rutherford backscattering*. The energy of the incoming projectiles is E_0, the energy just before scattering from the atom is E', immediately after scattering it is kE', and the energy of an outgoing projectile when leaving the target is E. [12]

Ions are hitting the target with energy E_0 at an impact angle α (see Figure 1) with respect to the normal of the sample surface. Just before scattering they have energy $E' = E_0 - \rho S(E_0)h/\cos\alpha$, and just after scattering kE'. Here we applied the density independent expression for the stopping power $\mathrm{d}E/\mathrm{d}x = -\rho S$ and inserted only S for energies of the incoming and outgoing projectiles. We assumed a linear dependence between the loss of energy ΔE and the depth h, which gives:

$$\Delta E = \rho\left(k\frac{S(E_0)}{\cos\alpha} + \frac{S(E)}{\cos\psi}\right)h\,. \qquad (7)$$

This relation is often written in the form $\Delta E = [S]h$, where $[S]$ is the average stopping power. This linear dependence is, despite a rough approximation, quite accurate and it is frequently used on account of its simplicity.

2.2.2 Scattering cross-sections

The cross-sections for Rutherford backscattering can be calculated in classical and quantum approximations. In the limiting case $m_1 << m_2$, a projectile with the collision parameter b scatters from an atom with an angle ϑ [97].

$$\tan\tfrac{\vartheta}{2} = \frac{Z_1 Z_2}{4\pi\varepsilon_0 b}\frac{1}{2E_0} \ . \tag{8}$$

Ions that have parameters of the collision in the interval from b to $b + \mathrm{d}b$ scatter into a solid angle $\mathrm{d}\Omega = 2\pi\sin\vartheta\,\mathrm{d}\vartheta$. So we get an equation for the scattering cross-section:

$$\frac{d\sigma}{d\Omega} = \frac{2\pi b\,db}{2\pi\,d(\cos\vartheta)} = \frac{b}{4\sin\frac{\vartheta}{2}\cos^3\frac{\vartheta}{2}}\frac{db}{d\left(\tan\frac{\vartheta}{2}\right)} = \left(\frac{Z_1 Z_2}{4\pi\varepsilon_0\cdot 4E_0}\right)^2 \frac{1}{\sin^4\frac{\vartheta}{2}} \ . \tag{9}$$

The Born approximation yields the same result. The scattering cross-section can be more compactly written in the following form [98]:

$$\frac{d\sigma}{d\Omega} = \left(\frac{d}{1-\cos\vartheta}\right)^2, \tag{10}$$

where d is a known half distance to which the projectile approaches the nucleus in a head-on collision.

When the projectile is significantly massive compared to the mass of the target atom, the scattering cross-section equation also includes both masses:

$$\frac{d\sigma}{d\Omega} = \left(\frac{Z_1 Z_2}{4\pi\varepsilon_0\cdot 4E_0}\right)^2 \frac{4\left[\left(m_2^2 - m_1^2\sin^2\vartheta\right)^{\frac{1}{2}} + m_2\cos\vartheta\right]^2}{m_2\sin^4\vartheta\left(m_2^2 - m_1^2\sin^2\vartheta\right)^{\frac{1}{2}}} \ . \tag{11}$$

The cross-section (Eqn (11)) is not valid at very low projectile energies, when the projectile scattering also depends on the electron cloud, and at high projectile energies when scattering is affected by the nuclear force.

The influence of the electron field changes the scattering cross-section only for a few percent, so we can use a correction factor. For example, the Andersen correction factor f [99] looks like this:

$$f = \frac{1}{1+\frac{V}{E_0}}; \quad V = 1.586\frac{Z_1 Z_2 e_0^2}{4\pi\varepsilon_0\cdot 0.8853 a_B}\sqrt{Z_1^{\frac{2}{3}} + Z_2^{\frac{2}{3}}} \ . \tag{12}$$

Ions that due to their high energy penetrate the Coulomb barrier in light atoms, scatter on the nucleus potential. The cross-section for the nuclear scattering can be few tens or hundreds of times higher than the Rutherford backscattering cross-section. In this way we can increase the sensitivity of the method for light elements. The scattering cross-section relative to Rutherford (elastic) backscattering for protons on He atoms is shown in Figure

2 [100]. At some combinations of projectile and target atoms sharp resonances can be observed. We can use them for measuring the concentration profiles. A typical example is the resonance of alpha particles with an energy of 3.04 MeV on ^{16}O atoms (Figure 3) [101]. The cross-sections from Figure 2, 3 were calculated for a scattering angle of 151° using the SigmaCalc [15] program. The original experimental data on which the correction is calculated is from the IBANDL database [12], which is the most extensive and comprehensive collection of nuclear scattering cross-sections (or non-Rutherford cross-sections as they are also called). In the scattering simulation programs, the use of cross-sections is limited by the present not yet complete understanding of the scattering processes, so we must rely on the use of experimental tables [96].

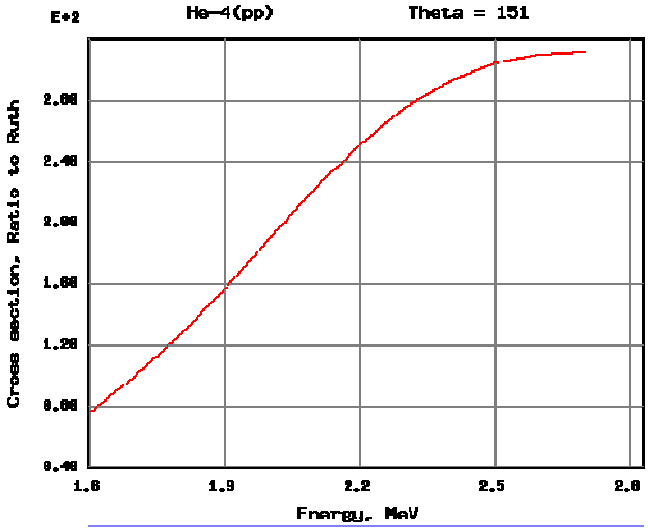

Figure 2: The scattering cross-section relative to the Rutherford backscattering cross-section for collisions of protons on He atoms corrected with the SigmaCalc program for an angle of 151°. Continuous increase from 80 to 310 times at energies from 1.6 to 2.7 MeV is shown. [15]

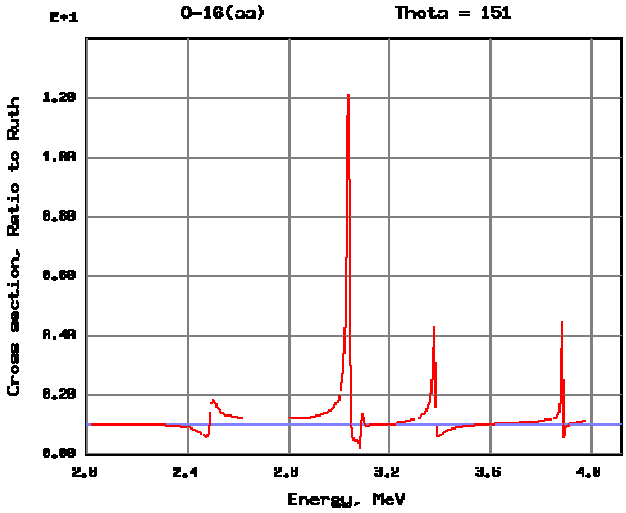

Figure 3: The scattering cross-section relative to the Rutherford backscattering for an (α,α) reaction on ^{16}O atom corrected with the SigmaCalc program for an angle of 151°. A sharp non-Rutherford resonance (12 times larger cross-section compared to the Rutherford value) at an energy of 3.038 MeV can be observed. [15]

2.2.3 Thin and thick target spectrum

An ion beam with energy E_0 is hitting a thin layer with thickness d. The layer should be thin enough to allow us to neglect stopping of ions in the layer, so the scattering cross-section is not changing with depth. The angle between the incident ion and the target normal is α, the outgoing ion leaves the target at the angle ψ to the target normal and the scattering angle ϑ is then the angle between the incident projectiles and the detector directions (Figure 1). We denote the mass fractions of separate compounds in the layer as x_i and the atomic densities as n_i. In time t the detector with a solid angle $\Delta\Omega$ detects the yield of scattered ions Y_i [95]:

$$Y_i = \frac{d\sigma}{d\Omega}(E_0)\Delta\Omega\ j_p t\ n_i \frac{Ad}{\cos\alpha}\ . \tag{13}$$

Here j_p was the current density of the incoming beam. With its geometrical cross-section of area A, the number of all the incoming ions is: $N_p = j_p A t$. The product $n_i d$ is the areal density of the atoms i:

$$q_i = n_i\, d = \frac{Y_i \cos\alpha}{N_p\ \Delta\Omega\ \sigma_i(E_0)} \tag{14}$$

We have written the scattering cross-section $d\sigma/d\Omega$ (11) at an angle ϑ in the short form $\sigma_i(E_0)$ and with that adopted that we are talking about scattering on the atom i.

In a layer which is a simple chemical compound, the areal densities of atoms are in the stoichiometric ratios. If that is not known, we determine it experimentally from the yields [95]:

$$\frac{n_i}{n_j} = \frac{Y_i}{Y_i}\frac{\sigma_j(E_0)}{\sigma_i(E_0)}\,. \tag{15}$$

The only value which we have to know is the ratio of the scattering cross-sections. If we have the Rutherford scattering regime, the cross-section ratio is approximately proportional to the ratio of the squares of the atomic numbers Z_j^2/Z_i^2. Eqn (15) also works for slightly thicker targets where we calculate the cross-sections at the middle of the layer.

From Eqn (14) we can calculate an estimation of the layer thickness d, if we insert the atomic density n_i:

$$n_i = \frac{\rho N_A}{M_i} x_i\,; \tag{16}$$

where N_A is Avogadro's number and ρ is the density of a sample. We calculate the yield of the scattered ions from a thick target by slicing the sample into layers, where z is the coordinate along the incoming beam. From the layer dz at the depth z we get the yield:

$$dY_i = \sigma_i(E')\Delta\Omega\ j_p\ t\frac{\rho N_A}{M_i} x_i\, A\, dz\ . \tag{17}$$

We used the shortened equation for a differential scattering cross-section and inserted the density of atoms n_i (Eqn (16)). As in Eqn (14), the number of incoming ions is: $N_p = j_p A t$. The scattering cross-section is a function of the energy squared [95]:

$$\sigma_i(E') = \sigma_i(E_0)\left(\frac{E_0}{E'}\right)^2 \tag{18}$$

With thick targets we cannot neglect the stopping of the projectiles in the target. Also the outgoing ions get a wider energy distribution, so instead of yield Y_i we measure the spectrum dY_i/dE:

$$\frac{dY_i}{dE} = \sigma_i(E_0)\left(\frac{E_0}{E'}\right)^2 \Delta\Omega\, N_p \frac{\rho\, N_A}{M_i} x_i \frac{dz}{dE} \tag{19}$$

Further solving of Eqn (19) is done either numerically or with analytical approximations. In the simplest approximation we calculate the derivative dz/dE using the Eqn (7), since $h = z\cos(\alpha)$:

$$\frac{\rho\, dz}{dE} = \left[k_i\, S(E_0) + \frac{\cos\alpha}{\cos\psi} S(E_i)\right]^{-1} \tag{20}$$

In an approximation which is valid only at the surface of the target, we can also neglect the factor E_0/E'. For a shape of the spectrum (yield as a function of energy) we get [95]:

$$\frac{dY_i}{dE} = \sigma_i(E_0)\,\Delta\Omega\, N_p \frac{N_A}{M_i} \frac{x_i}{k_i\, S(E_0) + \frac{\cos\alpha}{\cos\psi} S(E)} \tag{21}$$

Some simple examples of the scattered ion spectra, simulated with the program SIMNRA [102] are shown in Figure 4 and Figure 5. The spectrum of a mono-elemental target has an edge at kE_0 (Figure 4a). With multi-elemental target (Figure 4b) there are many steps in a spectrum which all correspond to k_iE_0 for the ions scattered from the surface. The multiple-scattering calculation [103] was used to get better agreement at low energies. In Figure 5a and 5b we can see a two-elemental thin layer on a mono-elemental substrate. The atoms of a thin layer are much heavier then the atoms in the surface, so we can distinguish them very well from the substrate. If the mass resolution is a bit worse (*e.g.* with lower energies of incoming ions), then both signals from the top layer can "melt" together (Figure 5b). This spectrum is much harder to interpret than the one in Figure 5a, so it is worth finding the best mass resolution for a given case by choosing the optimal type and energy of the projectiles.

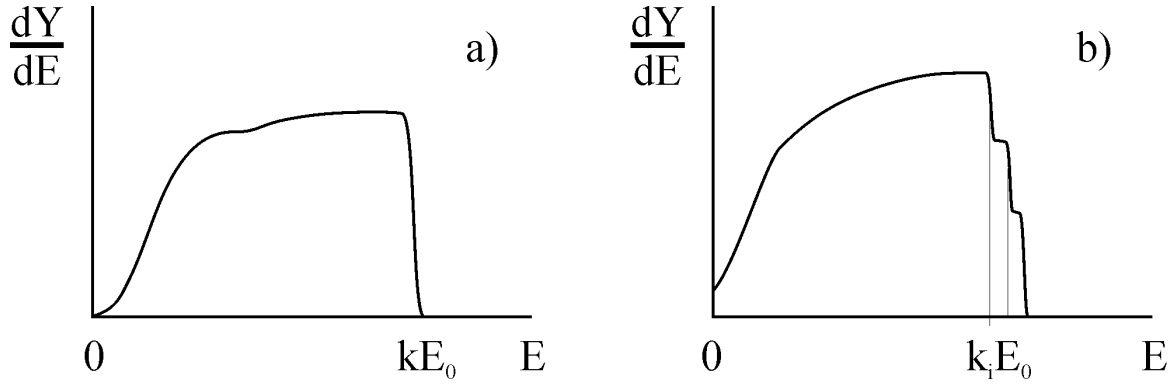

Figure 4: *RBS spectra of a homogeneous sample simulated by SIMNRA program* [102]. Spectrum of a thick mono-elemental target (copper) (a), thick homogeneous multi-element target (Al77Fe20Pb3) (b). Spectra are calculated for scattering of 3 MeV protons with geometry (α=0, ψ=45°, θ=135°) in the full energy range with a cut-off energy of 10 keV. In graph (b) a multiple-scattering calculation was used to get better agreement at low energies.

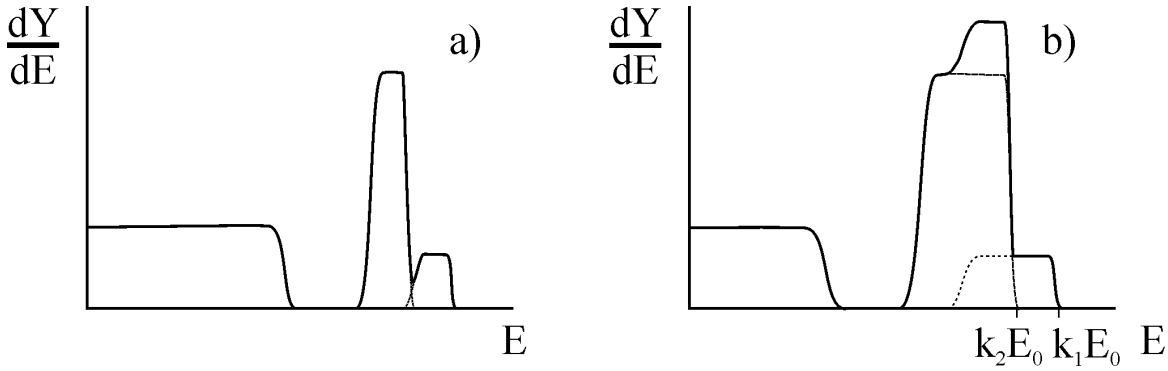

Figure 5: *RBS spectra of a two-layered sample simulated in the SIMNRA program* [102]. The top layer consisting of two sorts of atoms and the second layer being a light mono-elemental substrate (a, b). Spectra are calculated for scattering of 3 MeV protons with geometry (α=0, ψ=45°, θ=135°). The horizontal energy axis is limited to the highest 30% of the whole spectrum to zoom in the affected part. Spectrum (a) is calculated for a 5000e15 at/cm^2 layer of Zn97Pb3 on top of the aluminium substrate and spectrum (b) is calculated for a thicker layer (12000e15 at/cm^2) on the same substrate. The detector resolution and the energy spread of the incident beam were set to zero to simplify the understanding. Some energy spread still remains as a consequence of the energy straggling of protons in a helium atmosphere along the path to the detector.

The method is less successful for thin layers of light matter on top of a heavy substrate, because in this case the spectrum of the top-layer is always superimposed on the low-energy part of the heavy substrate spectrum.

2.2.4 Analysis of the spectra

The quantity which we measure experimentally is not dY/dE, but $(dY/dE)\Delta E_c$, where ΔE_c is the energy width of a channel in the spectrum. We determine it with the energy calibration of the scattered ions. This can be most easily achieved by measuring a few spectra of thick targets, which have high-energy edges at the energies $k_i E_0$. The measured spectra are a convolution of the distribution dY_i/dE (Eqn (19)) and the response function of the detector (usually approximated simply by the Gaussian distribution). For this reason the spectra have more round edges, as shown schematically in Figure 4. The shape of the spectrum at the low-energy part is determined by multiple-scattering [103].

Nowadays there exist many simulation programs that try to determine the thicknesses and composition of layers by fitting the simulated spectra to the measured spectra. A few of them were tested and compared under an IAEA intercomparison study [104, 105].

For any spectrum simulation program it is important that the scattering and stopping cross-sections as well as the stopping powers of the ions in matter which are both used for simulation, can be updated by the user. At the time of writing the latest set of stopping powers and ranges of ions in matter was SRIM2010, which can be freely downloaded from www.srim.org. The measured non-Rutherford scattering cross-sections, for various particle/atom combinations can be obtained through the IBANDL database [12] with evaluated EBS cross-sections for selected reaction using the SigmaCalc online program [15].

In the frame of the IAEA intercomparison the codes have been tested in two ways. First by simulating the scattering spectrum with the same parameters and second on a set of realistic experimental spectra. The intercomparison showed that all of the codes give good results within the limits of their design, and that the largest difference in the results is due to the differences in the fundamental databases used (stopping power and scattering cross-section). Agreement between the codes for the Rutherford backscattering spectrum simulation, including energy resolution convolution, energy straggling and the pileup effect is at the 0.1% level. This agreement can also be extended to the extraction of the information from real data [104]. With the use of the same scattering cross-section data also the non-Rutherford scattering can be simulated within this agreement. There are two codes which stand out in the Intercomparison, regarding the amount of features and implemented calculations. These two codes are SIMNRA [102] and NDF [106], called “new generation codes” in the Intercomparison. They both feature a pulse pileup calculation algorithm by Wielopolski and Gardner [107, 108], a dual and multiple-scattering calculation [109, 110], a straggling calculation using the model by Bohr, Chu or Chu/Yang, which are reviewed in Szilagi *et al.* [109, 111], and also a screening correction of the Rutherford cross-section by Andersen [99] or L'Ecuyer [112]. Both codes are also able to simulate the sample roughness [113, 114]. A good overview of the phenomena of surface roughness can be found in the SIMNRA User's Guide [102], and from a different point of view for NDF [115].

For the purpose of the analysis of the RBS spectra in this work, SIMNRA software was used.

2.2.5 The scattering angle

The scattering angle is the angle between the direction of the incoming and outgoing projectile velocities, and is defined by the position of the detector. It is parameter of the measurement that has to be set during the simulation of an RBS spectrum. The geometry of the scattering experiment as used in the SIMNRA program is shown in Figure 6 [116].

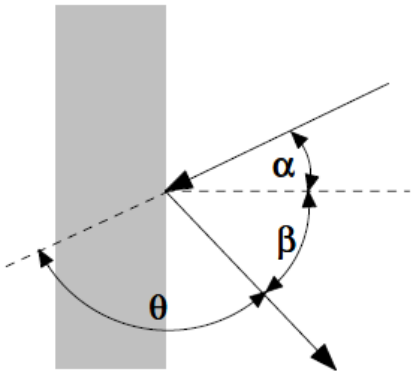

Figure 6: *Geometry of a scattering experiment as treated by SIMNRA* [102]. Incident angle α, exit angle β and scattering angle θ. Angles α and β are always positive and always measured from the target normal.

The scattering angle is usually fixed by the position of the RBS detector, however incident angle α and exit angle β can be changed with the position of a target. Both α and β are always positive and relative to the normal of the target.

Thin layers can be measured with a larger incident angles to increase the sensitivity. Changing the incident angle from 0° to 60° increases the signal from a layer by a factor of two. A change to the incident angle of 89° increases the signal of a thin layer by a factor of 60, however the effects of surface topography are substantial at the grazing angles [117]. A fit to the simulated data shows that an increase can be described perfectly by the longer path which the beam makes through the layer (Figure 7). This path is proportional to 1/cos(α). The scattering angle during this simulation was fixed at 151°.

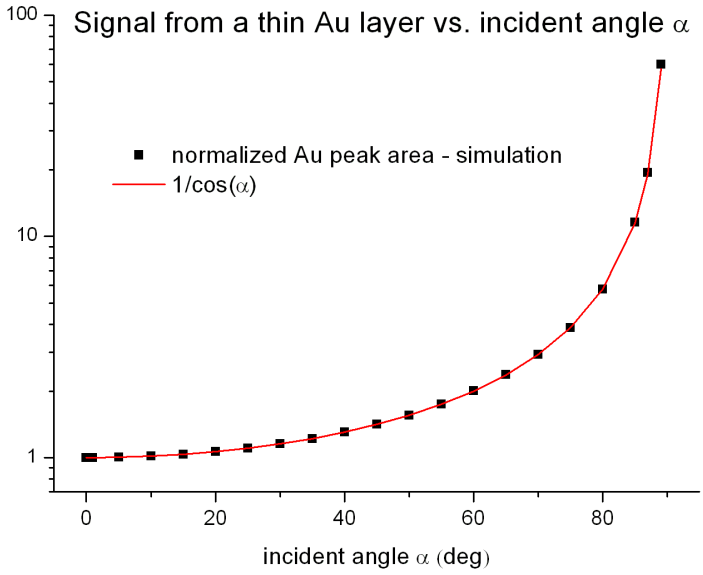

Figure 7: *A simulated signal from a thin layer vs. incident angle*. Detection of a thin layer can be increased up to a factor of 60 when the incident angle reaches 89°.

The detection of a thin layer can be improved by an order of magnitude by a change of the incident angle.

2.2.6 The units of thickness

The thicknesses d in SIMNRA are always written in the units of 10^{15} atoms/cm^2. But this unit can be translated into the linear thickness d_l in nanometres when the density is known, which is the case for all pure elements. When a polycrystalline material is formed, the density is not necessarily an average of the consisting single components. However, the result of an RBS analysis written in 1e15 at/cm^2 units is intrinsically correct since it is not affected by the transformation using the uncertain data of the density.

When a calculation of linear thickness is necessary, the atomic density ρ_{AT} should be first calculated from the density ρ, Avogadro's number N_A and the molar mass M:

$$\rho = \frac{m}{V} = \frac{n \cdot M}{V} = \frac{N}{N_A}\frac{M}{V} \quad \Rightarrow \quad \rho_{AT} = \frac{N}{V} = \frac{\rho \cdot N_A}{M} \tag{22}$$

The linear thickness d_l in nanometres is then:

$$d_l = \frac{d\left[10^{15}\,at/cm^2\right]}{\rho_{AT}\left[10^{15}\,at/cm^3\right]} = \frac{d}{\rho_{AT}}\left[10^7\,nm\right] \tag{23}$$

In this way we get a linear thickness which we can observe using an optical or electron microscope.

2.3 Construction of BS experimental setup

The BS experimental setup was a new implementation at the external beamline at the Microanalytical Center at the Jožef Stefan Institute. There are many laboratories with external (in-air) ion beams worldwide, among them Great Britain (Guildford) [118] France (Louvre in Paris, Bordeaux) [119-120, 121], Italy (Firenze, Lecce) [122, 123], Germany (Berlin) [124], Croatia (Zagreb) [125] Greece (Athens) [126], Spain (Seville, Madrid) [127, 128] Mexico (Mexico) [129], USA (Annapolis, Albuquerque) [130, 131], Japan (Takasaki, Tsuruga) [132, 133-134], most of them but not all also adopted the RBS technique. A very good "Review of external microbeams for ion beam analyses" by Giuntini was recently published [135].

The passivated implanted planar silicon (PIPS) [136] detector by Cannberra PD100-13-100AM was used as the particle detector at ambient pressure. Helium was used to reduce the absorption of the back-scattered particles along their path to the detector. The schematics of the RBS setup can be seen in Figure 8. The experimental setup with some measurements was described in [8].

The setup enables us to rotate the detector around the beam axis at a constant scattering angle. Since we have a He flush, it is preferable to use the detector in an upward position since in this way He, which is lighter than air, stays in the RBS nozzle. If the detector was positioned below the horizontal plane of the beam, the measurement would depend much more on a constant helium flux, however, the part of the path between the end of the nozzle and the target would get better filling with helium in the lower position. In any case it is important to keep the conditions constant during the whole set of experiments.

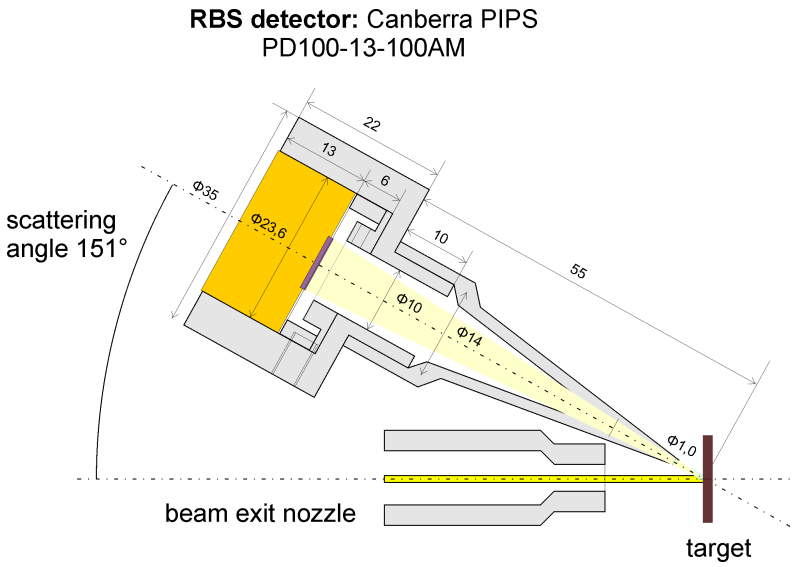

Figure 8: *The schematics of the RBS experimental setup*. The incident angle is 0° and the scattering angle is 151°. [8]

2.3.1 The helium flux

A flux of helium significantly reduces the stopping of backscattered projectiles as well as the attenuation of X-rays [137] along their path to the detector. A much better energy resolution is obtained using helium instead of air. A comparison of the simulated spectra of a thin Au layer on a copper-tin alloy sample, with and without a He flush, is shown in Figure 9. The He flux has a great influence on the spectrum, so its flow has to be kept constant during the measurement.

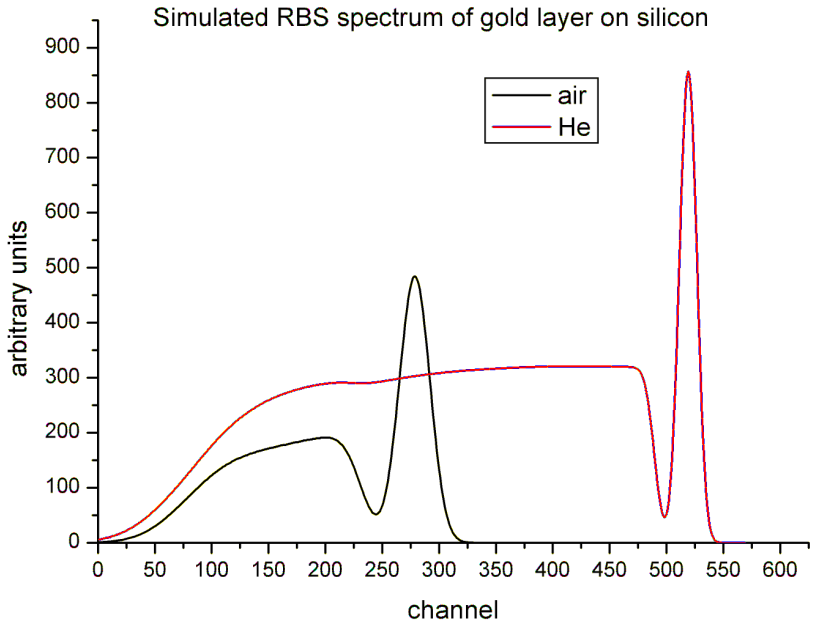

Figure 9: *An RBS spectrum simulated in a SIMNRA program, with realistic parameters*. The red line is a simulated graph of particles backscattered from a gold plated silicon with helium filling the space between the target and the detector and the black line is the same sample with the same setup, the only difference is that the gap is filled with air. A much worse energy resolution can be observed.

A constant flux was achieved by a standard reduction valve which changed the pressure from a cylinder (~200 bar at full cylinder) to a pressure of 2-3 bar at the secondary side of the valve (Figure 10). After that a flow-meter with a valve was used to set the flux of helium to a level of around 1 litre/min. In this way the conditions became stable, also stabilizing the helium flux.

Figure 10: *A flow-meter with precision needle valve at external beamline at Microanalytical center at Jožef Stefan Institute*. The flow-meter is necessary to ensure the constant flow of helium gas to the target.

2.3.2 Distance to the target

The optimal distance from the exit window to the target was set by the measurements of a thick target at various distances. The alignment was optimal when the count-rate for the specific target was maximal. That means the RBS detector was aimed directly at the surface of the target. The total counts of the spectrum were taken as a measure of the spectrum quality. The spectrum integral versus the distance of the target from the exit window can be seen in Figure 11. The interval of the acceptable working distance (count-rate in the 95% max. interval) is marked as d_{opt}+/-Δd.

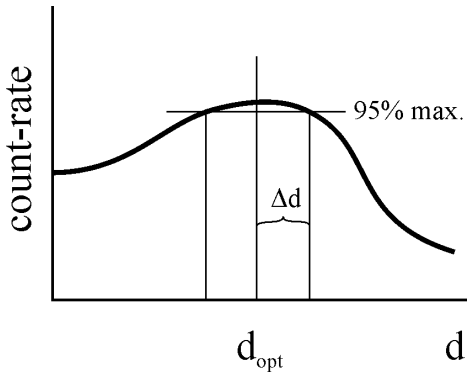

Figure 11: *Count-rate vs. distance to the target.* Optimal distance d_{opt} was determined in the region of the count-rate maximum.

The procedure for measuring the optimal distance should be repeated each time a

geometry is changed.

A simple calculation in SRIM gives us the result that a 3 MeV proton in 1 mm of air loses 12.1 keV of energy, whereas a 1 MeV proton losses 26.1 keV of energy. This means the positioning of the target should be repeatable to 100 µm to ensure the reproducibility of measurements within a 3 keV interval. The positioning system with a laser triangulation was developed for the purpose of reproducible positioning [8].

2.3.3 Micro-positioning system

Positioning of the sample is very important for RBS. It has to be accurate and reproducible. The system which enables us a satisfactory accuracy and reproducibility of positioning is based on laser triangulation. The system consists of a camera connected to a computer with an adjustable marker and a focused laser with a spot diameter of 100 µm. The laser focus was set to the distance of a target. Further improvement was achieved by the addition of the aperture at the laser tube exit, which decreases the amount of scattered photons around the spot, thus further narrowing the spot diameter.

The laser is mounted on a micro-positioning 3D stage with a 80 TPI (threads per inch) screw, which results in a displacement of 317 µm per turn. The laser spot can thus be positioned with an accuracy of better than 20 µm in the desired coordinates. The positioning system with the camera and laser on a micro-positioning stage is shown in Figure 12. The laser is focused on the target and an additional collimator is fixed at the exit of the laser to achieve a spot diameter of less than 100 µm on the target, without the ring of scattered photons at the edge of the spot.

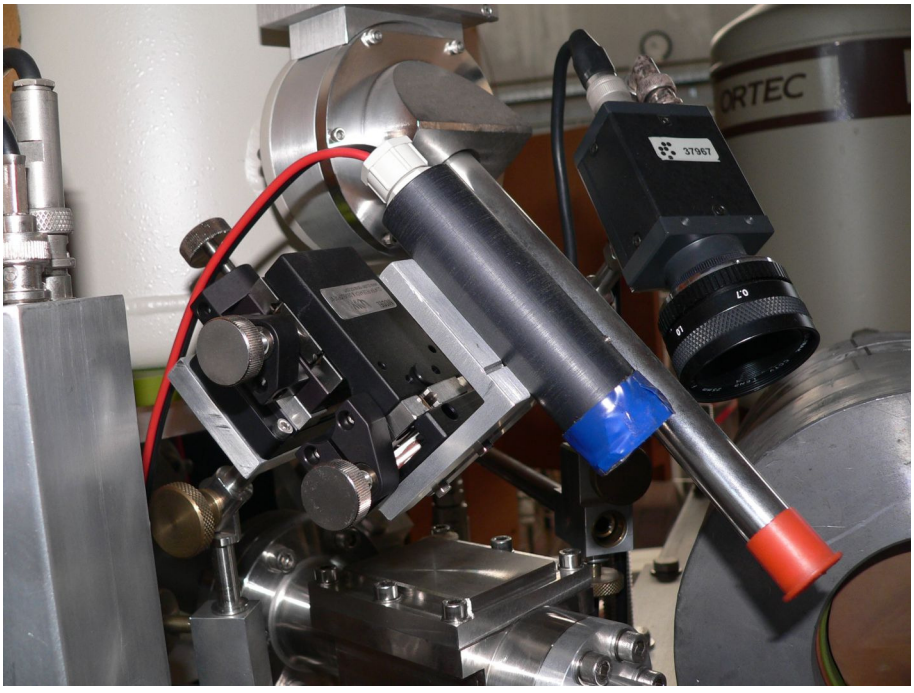

Figure 12: *The positioning system at Microanalytical center at Jožef Stefan Institut*. A focused laser mounted on a micro-positioning stage and a camera connected to the computer are parts of the laser-triangulation positioning system.

2.3.4 Measurement of proton current number

The basic parameter for obtaining quantitative results is the number of ions (protons) which hit the target. There are many approaches for measuring the proton dose in the external beam. The first and the most straightforward is measuring the charge on the target. But in this case the target must be conductive, and special care should be taken to avoid the effect of a local charge build-up and a charge increase due to the leakage of secondary electrons [138]. A review of charge measurements in external applications is available in Šmit *et al.*[45].

A very commonly used method for measuring the ion dose is a chopper which periodically intersects the beam [139, 140, 141, 142]. Particles elastically backscattered from the chopper covered with a thin Au foil are detected by the particle detector. Since the angular speed is constant the ratio between the transmitted and back-scattered protons depends on the angle covered by the chopper. The chopper is typically a section of a circle in order to keep the time the beam spends on the chopper constant, regardless of the beam position. The problem with the chopper method is that the chopper has to move. Moving causes vibrations, the vibrations are transferred to the other parts of the beamline. For a milli-beam these vibrations are not reported in the literature to present a problem. However, they contribute to a worse resolution of the micro-beam experimental setups. The vibrations can be reduced by precisely balancing the propeller, which is possible, but hard to do. Another problem with the chopper method is that a motor running in vacuum has a problem with cooling. The heat transfer through the vacuum is possible only through radiation, so thermal equilibrium is achieved at a high temperature at which the lifetime of the motor is significantly reduced. The situation can be improved by increasing the size and thermal conductivity of the contact between the motor and chamber, but even with an optimal thermal contact, a motor might fail after running constantly for a long period of time.

The most recent improvement of the chopper method is based on periodical deflecting of the beam to a gold target [119] or a Faraday cup [143] in vacuum and measuring the signal of the recoiled ions (RBS). By measuring the RBS signal and knowing the precise time when the beam has been deflected to the gold target and the time when the beam was irradiating the measured sample, we can calculate the dose of ions on the sample. This system was developed and is used in the Accélerateur Grand Louvre d'Analyse Elémentaire (AGLAE) facility in Paris, France [119]. Its major improvement over a motorized chopper is that it does not have movable parts, however the magnet field fluctuation to achieve proper deflection of the beam might present a new source of error.

For an external beamline, a good system is detection of the X-ray or RBS signal from a thin exit foil [122, 144], separating the vacuum in the beamline from the surrounding air. The foil can be a few μm thick metal foil (Al, Be, Au, Ta, ...) or a 100 nm thin Si_3N_4 membrane, produced by semiconductor technologies. This system is practical since it does not require movable parts, but the problem is that the target X-rays can reach the detector and interfere with the signal from the window. As the foil thickness may change due to irradiation, the system requires frequent recalibration. Also the detector can get damaged in the case of a sudden exit window failure.

An efficient solution for proton current measurement is to intercept a fraction of the beam by a metal wire-mesh in vacuum [145]. A system based on this principle was implemented at the external beamline at MIC and is described in the next chapter.

2.3.5 The wire-mesh-based charge-collecting device

The system for measuring proton dose by collecting charge with a wire-mesh intersecting the beam (Figure 13) was developed and is installed at the external beamline at MIC (Figure 14). The device does not have any moving parts. It is constructed in such a way that the secondary electrons are suppressed by a negative voltage on the shield electrodes in front of and behind the central wire mesh, which collects the positively charged projectiles. The construction and testing of the device is described in an article by El Bouanani *et al.* [145]

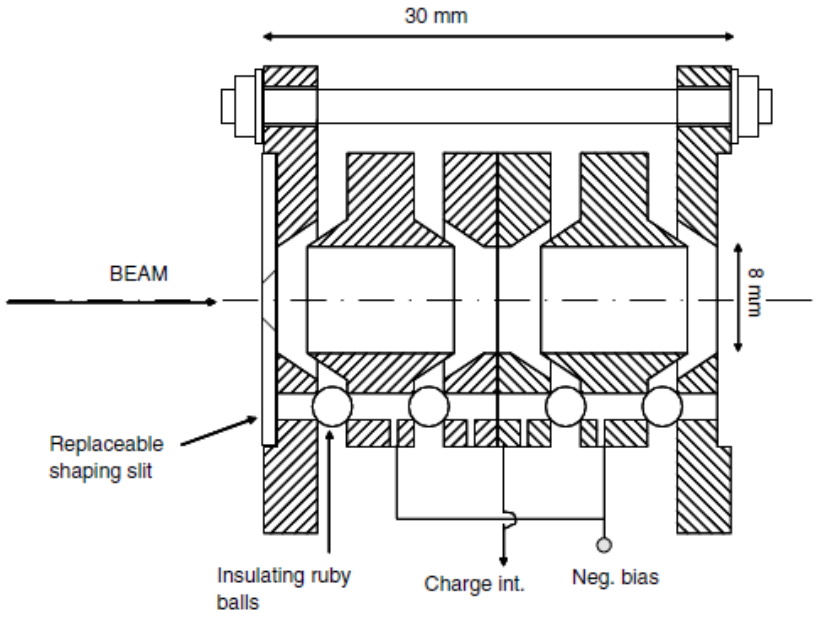

Figure 13: *The wire-mesh based charge-collecting normalization device*. The negative bias at the shield electrodes in front and behind the central wire-mesh prevents variation of the positive current on account of the emission of secondary electrons. [145]

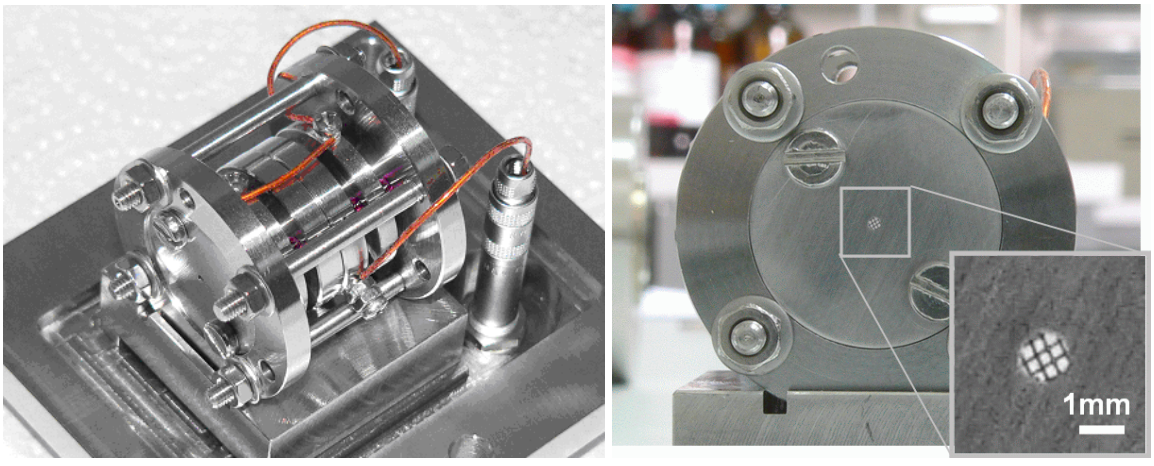

Figure 14: *The wire-mesh charge-collecting device installed on external beamline at Microanalytical center at Jožef Stefan Institut*. The collimator is made of tantalum, with a hole of 0.7 mm diameter. Wire-mesh is Pt-Rh alloy 80 x 80 mesh, the wire diameter is 0.003 inch (76.2 µm). [8]

To prevent current leakage between the wire mesh and the shield electrodes, ruby balls are used. The beam is shaped with a tantalum collimator with a hole of 0.7 mm diameter.

The 3 MeV protons should be stopped in the wire-mesh, and for this reason the alloy of 90 % Pt and 10 % Rh was chosen, which has good proton stopping power characteristics, besides exceptional mechanical properties and high melting point (1850 °C). The wire diameter is 0.003 inch (76.2 μm). The density of the mesh is 80 x 80 mesh, which means 80 wires at a distance of one inch in the horizontal and vertical directions, giving an aperture of 57.76 %. The range of 3 MeV protons in the alloy according to SRIM 2008 is 25.84 μm. The diameter of the wire is thus almost three times wider than the range. From this we can calculate the area of the mesh where the protons can penetrate the wire of a round cross-section. This area is 1.2 % of the whole area of the wire mesh and represents a negligible part of all the protons, so the wire-mesh has a small perturbation on the energy distribution of the probing beam. However, there is a downside of using this method. The beam has to uniformly cover the area of the wire mesh limited by the collimator. Reducing the beam current by slightly deflecting the beam (which is a current practice at the beamline, results in a wrong current reading since the wire-to-opening area ratio of the mesh changes drastically with the beam position, whenever the current density over the collimator area is not homogeneous. For the same reason the device cannot be used for the measurements of the particle dose of a micro-beam. To preserve the homogeneity, a beam current has to be regulated by defocusing of the beam at the injector.

2.3.6 The chopper method

The chopper method measures the projectile dose by periodically intersecting the beam. The intersection is commonly accomplished with a rotating propeller, typically reducing the current by less than 10%. The beam can also be arbitrarily small, which is especially suitable for micro-beam current measurement. The beam's position can be changed without affecting the current measurement thus permitting the mapping technique based on the beam displacement.

There are many chopper systems reported to be used in literature [138, 139-142, 146, 147, 148]. However, during my work I encountered three different systems for particle dose measurement using the chopper method. At MIC, JSI, there are two choppers, and the third one is at the external beamline at Ion Beam Centre (IBC) at University of Surrey where I performed some measurements of textile fibres in the frame of the SPIRIT project (Figure 15).

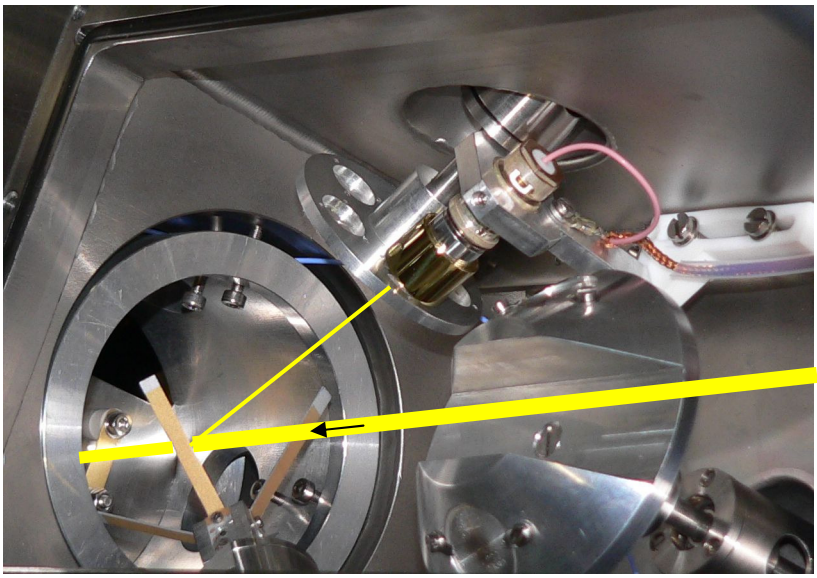

Figure 15: *The chamber with a chopper propeller at the external beamline at the University of Surrey with a projected path of the beam*. RBS detector with the possibility of changing filters and a turn table for observing the beam on a quartz screen.

The chopper unit at the external beamline [118] at the University of Surrey is relatively massive, it is about half a meter long with a cover made of a few centimetres thick and rather heavy glass plate, which enables a view inside, to check if the chopper is turning. When the chamber is evacuated the air pressure pushes the plate to the chamber and prevents any lateral moving of the plate. The motor turning the chopper is outside in the air and the transmission is made with a help of a ferrofluid (a magnetic fluid). The transmission sometimes, after a long time of no use, gets stuck and the glass cover has to be removed and the propeller is kick-started manually.

At the external beamline at MIC, a much smaller normalization chamber contains an in-vacuum motor which can be interchanged with a wire-mesh charge collection device. It uses two carbon pieces plated with gold which are hit by the beam. The gold peak of the RBS spectrum is then integrated and used as a measure of the total particle dose in the beam. The upper cover with a chopper motor and a lower cover with an RBS detector of the normalization chamber is shown in Figure 16. The particle beam is entering from the left, partly scattering back to the RBS detector. The amount of the beam lost by the chopper is proportional to the angle covered by the two carbon pieces. In our case this is 2x20°, which means that 11% of the beam is lost. This number is favourable compared to the wire mash, where 42% of the beam is lost.

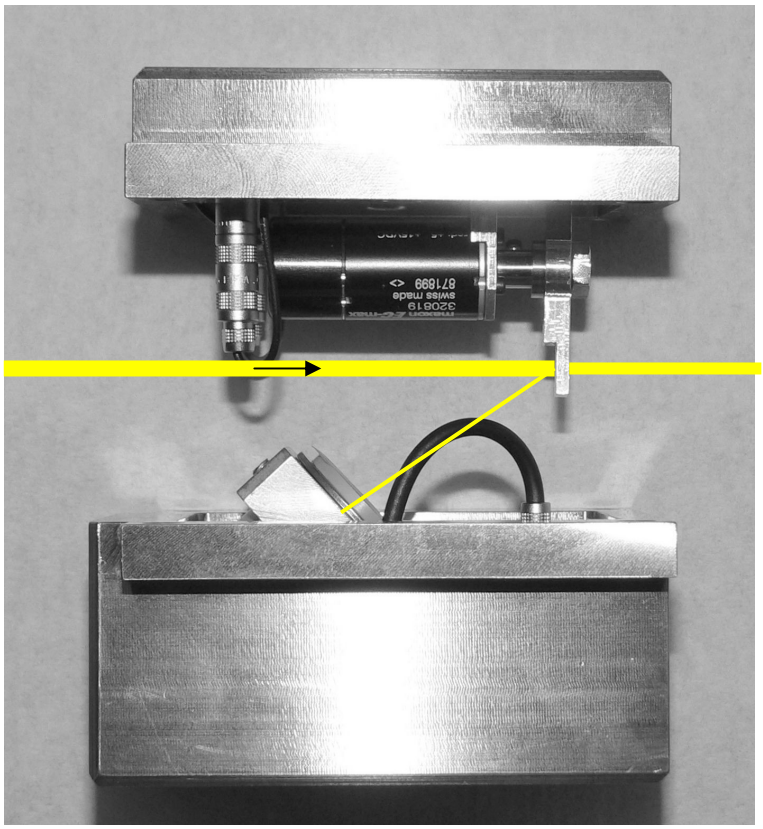

Figure 16: *Upper and lower cover of the chopper-based normalization device at MIC with a projected path of the beam.* An in-vacuum motor with a chopper propeller is fixed to the upper cover and an RBS detector on the lower cover of the normalization chamber. The gold plated carbon pieces on the chopper propeller are missing.

2.4 X-Ray emission based methods

X-rays were discovered by Wilhelm Conrad Roentgen on the 8th of November 1895 [149], since than a huge impact of this new technology can be observed. This new type of rays ("eine neue Art von Strahlen") led to further investigation and the discovery of radioactivity from uranium by Becquerel in 1896, as well as radiation from radium and polonium discovered by Marie and Pierre Curie in 1898. Soon afterwards in 1906 Barkla discovered the polarization of X-rays, bands in atomic absorption (1909) and characteristic X-rays, the so called K, L, M... series were discovered in 1911. The wave properties of X-rays were investigated by von Laue who in 1912 observed the diffraction of X-rays in three-dimensional structures with a regular repeating pattern. But it was W. H. Bragg who derived the famous Bragg formula and using the Bragg spectrometer observed reflection patterns from single crystals of NaCl and KCl. X-ray diffraction analysis was born.

Following the investigation of the properties of X-rays by Barkla, Moseley with an exchange of communications with W.L. and W.H. Bragg continued with a study of characteristic X-rays. Siegbahn measured the wavelengths of characteristic X-rays with his new spectrometer, and precisely and classified them into α, β, γ ... according to the X-ray intensities in the respective series. X-ray spectroscopy was established with his work in 1913-1923. During these years only the gas ionization chamber invented by Perrin in 1896 was used as a detector, until Geiger and Müller produced a new useful counter for the detection of X-rays (and γ rays) called the Geiger-Müller counter. With the development of the high-power X-ray tube, the GM counter and goniometer with a Si monocrystal, measurement of fluorescent X-rays were possible. The first commercial X-ray fluorescence spectrometer was produced by Friedman and Birks in 1948. This was the start of modern X-ray spectrometry.

XRF is a spectroscopic method where high-energy X-rays or gamma-rays are used to achieve the emission of secondary X-ray photons also called fluorescent X-rays. With this technique we can perform the chemical analysis of metals, ceramics, glass, or other materials. The method is extensively used in geochemistry, archaeology, forensics and recently in live sciences. The apparatus used for XRF analysis can be made portable which enables quick in-situ measurements.

An incident X-ray photon (Figure 17 [150]) ionizes the atom by ejecting an electron from the inner shell of the atom. A vacancy is filled by an electron from an outer shell. This electron displacement causes the emission of a secondary X-ray, which is detected by the X-ray detector. Each element has a specific energy of electron transitions, so the secondary X-rays are characteristics of a specific element. A representative XRF spectrum of a multi-elemental target can be seen in Figure 18 [151]. The spectrum consists of characteristic lines, also called "peaks", indicating the presence of a particular element. The amount of an element is not directly proportional to the area of the peak, it also depends on the X-ray production cross-section and absorption in the filter in front of the detector and in the sample itself.

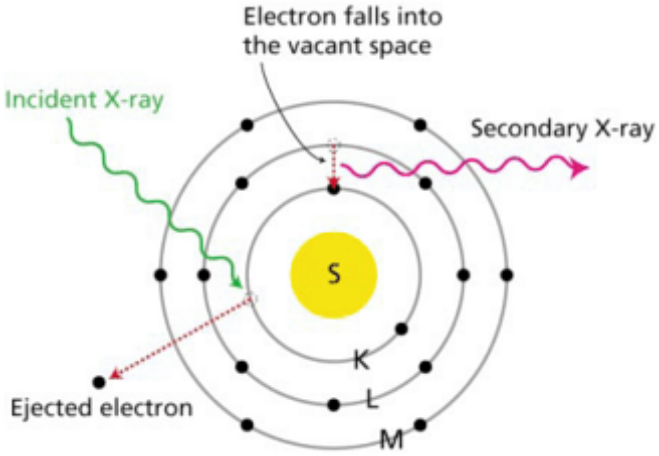

Figure 17: *Secondary X-ray production scheme.* XRF is based on detection of secondary X-rays induced by incident X-rays. [150]

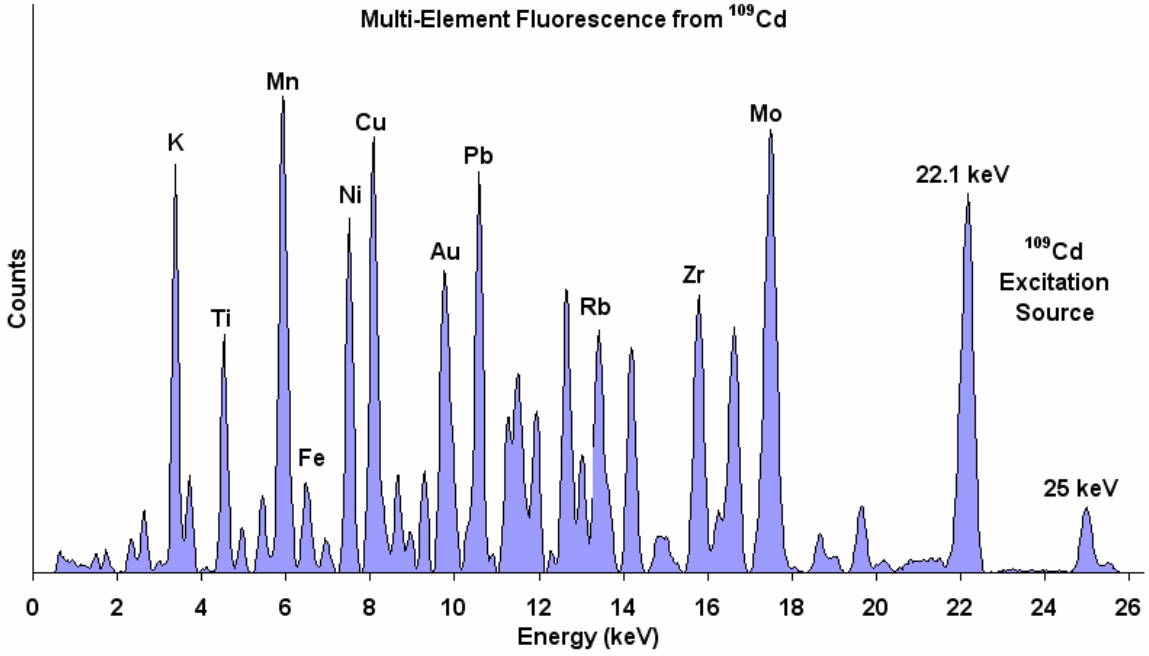

Figure 18: *X-ray fluorescence (XRF) of multi-element sample from ^{109}Cd cathode.* Spectrum is in linear scale. It depictures the capability of simultaneous multi-elemental analyses of XRF method. [151]

X-rays produced by the transition of an electron from the L shell to the K shell is called K-alpha, and X-rays produced by the transition of an electron from the M shell to the K shell are called K-beta. The peaks induced by transitions to the L shell are called L lines and according to their intensities called L-alpha, L-beta, L-gamma and so on.

The levels of detection for most elements with this spectroscopic method are around 10-100 ppm and depend on the cross-section for a certain element. The cross-sections for the production of characteristic X-rays depend on the energy of incident X-rays (Figure 19).

Secondary X-rays can also be induced with particles i.e. electrons, protons or other ions. Electrons with a few ten keV energies are used for the chemical analysis of targets in electron microscopes. But electrons, which have relatively low mass compared to

protons or other ions are stopped in the material quickly. At energies of 20 keV they penetrate up to 1 µm of material. This means they are stopped from a velocity of a few tenths of the speed of light to zero over a distance of 1 µm. This rapid deceleration results in huge bremsstrahlung, which is not desirable for the resolution of the spectrometer, since secondary X-ray peaks are lost in the bremsstrahlung background, if the concentration of an element is below, for example, 0.1%. The linear scale is more suitable for displaying the spectra induced by electrons due to the intense bremsstrahlung background, however logarithmic scale is more informative for spectra induced by protons (Figure 19).

Bremsstrahlung can be reduced for many orders of magnitude by the use of heavier particles. Protons are especially suitable for this purpose. The higher mass of projectiles means the penetration depth will be higher and the deceleration will be slower, which induces lower bremsstrahlung. But in order to achieve an efficient ionization in the target, projectiles should be accelerated to higher energies, typically above 1 MeV. In this case the spectroscopic method based on the analysis of induced secondary X-rays is called PIXE - particle induced X-ray emission. With the use of ~1 MeV protons or other ions, the penetration depth in the solid matter ranges from ~10 µm to ~100 µm, depending on the density and atomic number of the analyzed material. With a significantly reduced bremsstrahlung (Figure 19) a higher resolution can be achieved and the level of detection drops to an impressive ~10 ppm for most elements.

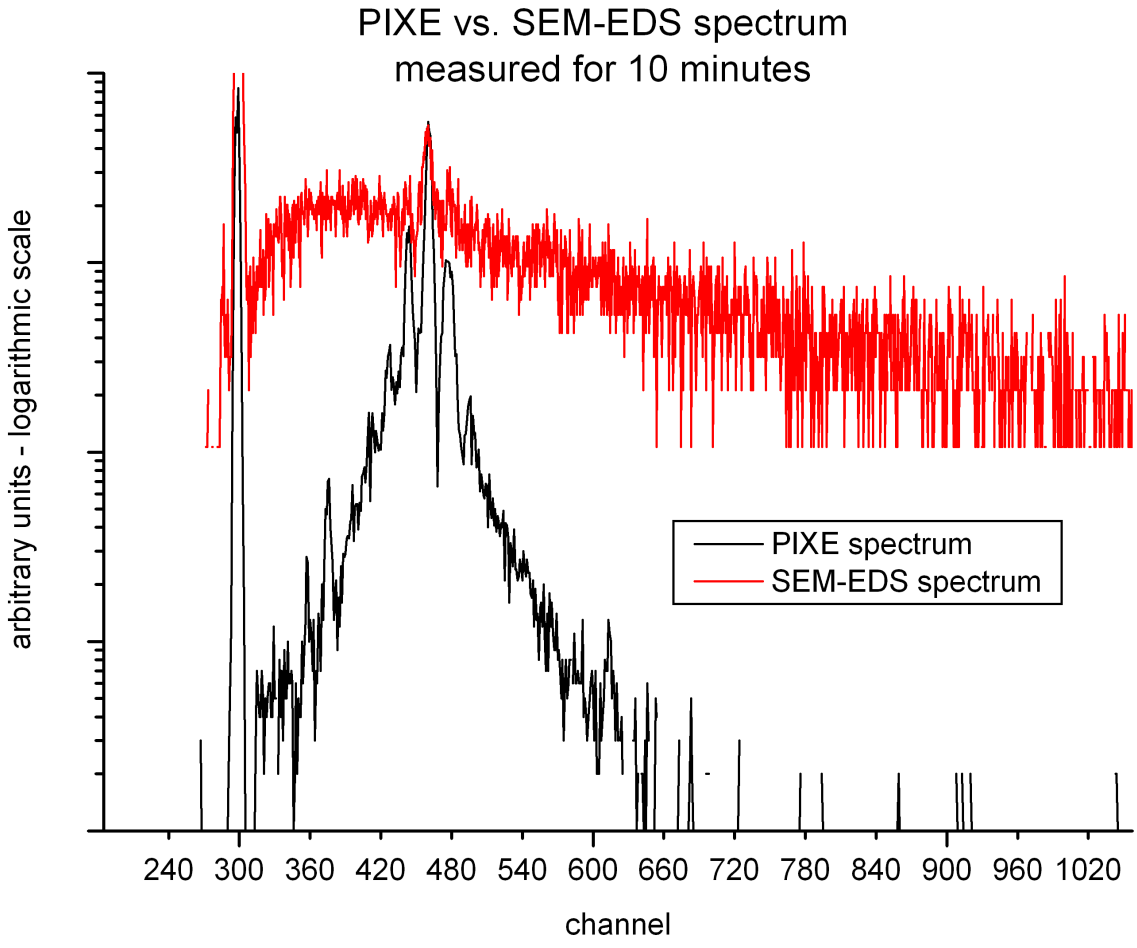

Figure 19: *SEM-EDS vs. PIXE spectrum.* Comparison of SEM-EDS and PIXE spectrum of textile fibre in a logarithmic scale. Both spectra were measured for 10 minutes. Spectra are normalized to the height of the highest identified peak, however the height of a detected peak in a SEM-EDS spectrum was 106 times lower than the height of a peak in PIXE spectrum.

2.5 The PIXE method

PIXE measurements have a long tradition with important applications in archaeology, environment sciences, aerosol measurements and biomedicine. Recently an interest from the forensics community was observed to perform PIXE measurements of gunshot residue [69], glass fragments [152, 153] and other types of evidence used in a criminal investigation [154, 155, 156]. One of a most commonly found evidence is fibres. The quantitative results of fibre analysis would be the most useful for forensics. The fibres are typically threads of woven fibrils (mono-fibres) and are in one dimension very long (infinite), however in the other two dimensions (in cross-section) their dimensions are similar to the range of a few MeV protons. The geometrical cross-section of a fibre is a bundle of fibrils, which have a shape of their own, usually their cross-section is circular, but also other shapes exist. Measuring such a bundle of fibrils is obviously very different from measuring a thick target. The fibrils are tightly woven, thus forming an approximately close packed lattice in the cross-section. However, the first-order approximation of the fibre geometry is a cylinder.

The effect of cylindrical geometry was accessed before in the literature [78, 80]. It has been shown that the result of the measurement depends upon many parameters. The most important parameters are: the radius of the measured fibre, the orientation of the fibre, the density and structure of the fibre, and the trace elements present in the fibre. A mathematical model which takes into account these parameters was developed to obtain the quantitative results of fibre measurements. The model is described in a separate chapter of the thesis. Measurements made at the University of Surrey and at MIC are presented and calculated using the cylindrical target model. The PIXE results were extended with PIGE measurements and compared with other independent methods.

2.5.1 The PIXE yield

The yield of photons upon irradiation with protons depends on the cross-section for X-ray production σ_i^x, the density of particle current j_p, the time t, and the number of atoms impacted by projectiles N_i:

$$Y_i^{tot} = \sigma_i^x j_p t N_i . \qquad (24)$$

The fraction of X-rays detected by the X-ray detector is $(\Delta\Omega/4\pi)\,\varepsilon_i\,\eta_i$, where $\Delta\Omega/4\pi$ is the solid angle, ε_i is the efficiency of the detector for photons which hit its entrance window, and η_i is the transmission of filters between the target and detector. The number of atoms N_i inside the beam is proportional to the mass: $N_i = \frac{m_i N_A}{M_i}$, where M_i is the molar mass of the atoms i, N_A is Avogadro's number and the mass m_i is expressed with the partial mass density ρ_i and volume of the irradiated part of the target: $N_i = \frac{\rho_i N_A A\, d}{M_i \cos\alpha}$. The target is in general inclined by an angle α relative to the beam, so its effective thickness is $d/\cos(\alpha)$. N_i is inserted in Eqn (24), the product $\rho_i d$ is replaced with the area density q_i and $j_p A t$ is the number of protons N_p. The X-ray yield Y_i for element i is then proportional to q_i:

$$Y_i = \frac{\Delta\Omega}{4\pi} N_p N_A \frac{\varepsilon_i \eta_i \sigma_i^x}{M_i} \frac{q_i}{\cos\alpha} . \quad (25)$$

To determine the area density q_i, we have to know the efficiency and the solid angle of the detector, the transmission of the absorbers in front of the detector, the cross-section σ^x, and we have to measure the number of protons N_p.

The area density is very rarely derived directly from Eqn (25), since the solid angle $\Delta\Omega$ is hard to measure. Instead, we prefer to use standards, which are samples of very well known composition and area density and are available commercially. During the calibration procedure we measure the product of the invariable parameters and mark it as $1/F_i$:

$$\frac{\Delta\Omega}{4\pi} N_A \varepsilon_i \eta_i \sigma_i^x \equiv F_i^{-1} = \frac{Y_i^s}{N_p^s} \frac{M_i}{q_i^s} \cos\alpha , \quad (26)$$

where the Y_i^s and N_p^s are the X-ray yield and proton dose, measured for the standard. The area density is then:

$$q_i \equiv F_i M_i \cos\alpha \frac{Y_i}{N_p} . \quad (27)$$

The parameters F_i need not be calibrated for each element separately. The function F is changing continuously with the atomic number Z, so 7 to 10 points are sufficient. Between those points we use interpolation. A separate calibration for the K and L shells has to be used. This calibration procedure using standards has to also be applied with strong absorbers. The transmission of X-rays can be calculated with an error lower than 5% only if it is higher than 19%. For lower transmissions it is better to use a calibration.

We can avoid the measurement of a proton dose by adding an internal standard to the sample.

2.5.2 The thick target model

In a thick target, we are interested in the mass percents x_i of single components. With partial densities ρ_i they are related as $x_i = \rho_i / \rho$; where ρ is the density of the sample. Charged projectiles decelerate in the sample, so with depth also the ionization cross-section decreases. When calculating the yield, we split the target into layers with a thickness dz (Figure 20). If we measure the coordinate z in a direction of the beam, the contribution of a single layer is [95]:

$$dY_i = \frac{\Delta\Omega}{4\pi} N_p N_A \frac{\varepsilon_i \eta_i}{M_i} \sigma_i^x(z) \exp(-\mu_i \xi(z)) \rho_i dz . \quad (28)$$

In Eqn (28) we took into account the cross-section energy dependence and absorption of X-rays along their escape path through the target. With a smooth thick target model, the escape length ξ is simply a function of coordinate z:

$$\xi = \frac{\cos\alpha}{\cos\psi} z \,. \tag{29}$$

Here ψ is the exit angle of the X-rays (Figure 20).

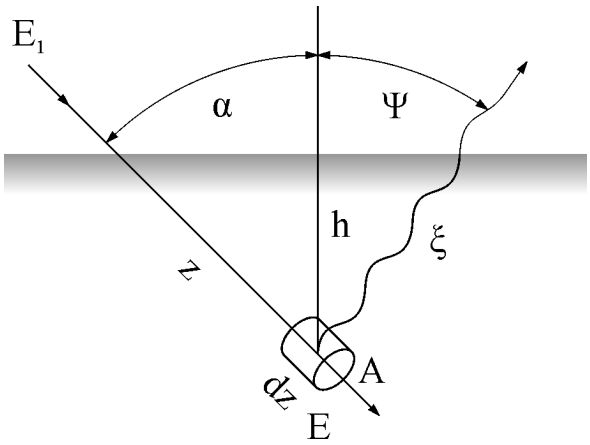

Figure 20: *The schematics of PIXE thick target geometry*. The energy of the incident projectiles E_1 decreases to E along the path z. Absorption along the escape path ξ is taken into account in Eqn (28). [95]

In the samples with irregular surface, $\xi(z)$ is not a simple linear function, but rather a probability distribution function. The X-ray yield Y_i is obtained by the integration of Eqn (28). As the cross-section σ_i^x is a function of proton energy, we have to translate the integration along z to the integration along energy E. We achieve this with the transformation:

$$dz = \frac{dz}{dE} dE = dE / (dE / dz) = -\frac{dE}{\rho\, S(E)} \,. \tag{30}$$

Here, $S(E)$ is the stopping power which is independent of density. Eqn (30) serves us also for the calculation of the path along which the proton energy decreases from the incident value E_1, to $E(z)$:

$$z = \frac{1}{\rho} \int_{E(z)}^{E_1} \frac{dE}{S(E)} \,. \tag{31}$$

Energy-dependent factors in Eqn (28) are combined in the thick target factor:

$$T_i = \int_0^{E_1} \frac{\sigma_i^x(E)}{S(E)} \exp\left(-\mu_i\, \xi(E)\right) dE \,. \tag{32}$$

Now the yield Y_i of an element i can be written:

$$Y_i = \frac{\Delta\Omega}{4\pi} N_p N_A \frac{\varepsilon_i \eta_i T_i}{M_i} x_i . \qquad (33)$$

The yield seemingly depends only on the mass fraction x_i; actually it is a function of the concentration of all the elements in the target, which determine the value of the stopping power *S(E)* and the attenuation coefficient μ_i in the thick target factor T_i (Eqn (32)). Values x_i can thus be calculated with an iterative procedure.

The measurement of the solid angle $\Delta\Omega$ can be avoided in one of four ways [95]:

a.) By the use of an internal standard.

A known amount (determined by a precise balance) of an element which is not present in the sample is intermixed with the sample and homogenized. Thus the measurement of the proton dose can be avoided as well. A popular internal standard is Y_2O_3, since it is almost never present in the samples.

b.) Calibration with standards.

We can use standards in a shape of thin or thick targets. We can make use of many pure compounds which we find in the laboratory. However the surface should be cleaned and polished. With this method it is critical to measure the proton dose, which is a bridge between the compositions of the standard and unknown sample. A calibration using thick targets is in general slightly less accurate than with thin targets, since with thick targets the energy dependence of the cross-section and the attenuation coefficient has to be known.

c.) Normalization to $\Sigma_i x_i = 1$.

In a sample where all the elements emit measurable X-rays the statement that the sum of all the mass fractions x_i is one (100%) holds. With this we eliminate the need to know the solid angle as well as measurements of the proton dose, since the constant factors don't influence the normalization procedure. We can use the method when measuring the metal alloys, and also with the analysis of glasses where 100% is the sum of all the mass fractions of metal oxides [39, 46]. With strong absorbers, the use of standards with similar compositions to the samples is advisable. The calibration consists of a trial and error procedure to determine the correction factors for X-ray yields, until the values of the standard are reproduced.

Algorithms based on the normalization procedure are numerically very stable, so the calculated concentrations converge already in a few steps to the final values. With normalization the influence of errors, due to the statistical fluctuations and uncertainties in the databases, are also reduced.

d.) Combination of PIXE and RBS

Both PIXE and RBS spectra are proportional to the proton dose, so with a simultaneous measurement of X-rays and back-scattered projectiles and correlated fitting of both spectra to the model values we can eliminate the need to measure the proton dose [157]. However, we should know the ratio of solid angles of both detectors.

The procedures described in this chapter can be used for a thick target, but when a geometrically structured target is measured, the physical model should be changed. The model of a cylindrical target, which can be used for the calculation of the X-ray yields and finally the concentrations in the targets of a cylindrical shape will be described in the next chapter. The efficiency of the cylindrical target compared to a thick target model will be evaluated. There is a lack of standards of cylindrical shape, the only samples we could find with a known composition were metal wires. We used metal wires of various elements as standards to calibrate the system for cylindrical geometry.

2.5.3 Cross-sections for X-ray production

The uncertainty of the results of the best performed measurements still depend upon how well the cross-sections have been measured in the first place. Most of the cross-sections for interactions with protons have been meticulously measured many times, so the data is accurate up to a few percent. Some other reactions with more exotic beams have not been measured so frequently, so the cross-sections might be much different than found in the literature. However for PIXE measurements with a proton beam of few MeV we can safely say the X-ray production cross-sections are accurate to within 5% uncertainty [158].

The physical process of atomic ionization with a heavy projectile and the accompanied X-ray production can be theoretically modelled. The most simple model approximates the wave function of the projectile far from the atom with a plane wave. The ionization is calculated as a scattering of a plane wave on a bound electron. The calculation is made using the Born approximation, so the method is named with the acronym PWBA (Plane wave Born approximation). The PWBA method was widely spread with the review article [159] and due to its simplicity, it was widely adopted. Much effort was put into the method's improvement by the inclusion of factors compensating for phenomena not included in the basic model. The most successful and widely accepted set of corrections of the PWBA method is called ECPSSR theory, which is still used in work with experimental data and databases. The theory was developed by W. Brandt and G. Lapicki [9]. The name of the theory is an acronym of the effects taken into the account:

1. Energy loss of the projectile (E)
2. The movement of a projectile in a Coulomb field of the nucleus (C)
3. Change of a binding energy in a perturbed stationary state model (PSS)
4. Relativistic effects (R)

A program for the calculation of X-ray production cross-sections using the ECPSSR theory is not very complex since the integration can be avoided with the use of tables. The cross-sections used for data quantification in this thesis were calculated by the direct integration method [10] applied to the ECPSSR model as stated in the original version from 1981 [9].

2.5.4 The model of a cylindrical target

The model of a cylindrical target is used for targets of cylindrical geometry when the beam is homogeneous, the surface is smooth, and the elements are distributed homogeneously. A schematic of the geometry is shown in Figure 21 [62]. The discrepancies from real samples will be discussed further on in the thesis.

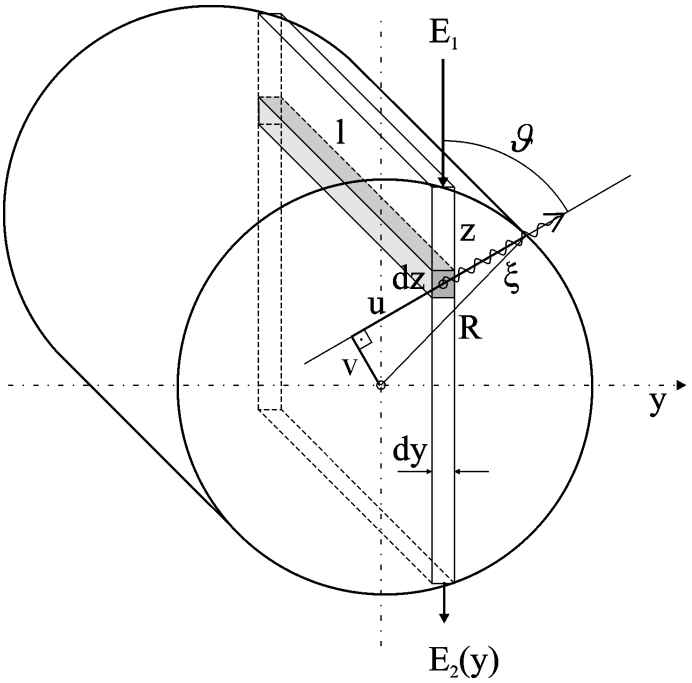

Figure 21: *A schematic for the integration of a cylindrical target.* Exit length ξ varies across the diameter of the cylinder. [62]

The target of radius R is sliced into layers of thickness d*y,* perpendicular to the axis *y*. In a particular layer the local coordinate *z* is measured along the proton path. The number of X-rays excited in the differential volume $l \cdot dz \cdot dy$ and detected by an X-ray detector with a solid angle $\Delta\Omega$, efficiency ε_i (for a particular line *i*), and equipped with an absorber of transitivity η_i is given by:

$$dN_x^i = \frac{\Delta\Omega}{4\pi}\sigma_i\, j_p\, t\, N_{at} e^{-\mu_i \xi} \qquad (34)$$

where σ_i is the X-ray production cross-section, *t* is the measuring time and N_{at} is the number of atoms in the layer: $N_{at} = \frac{\rho_i}{M_i} N_A\, dV$ with M_i the atomic mass of the atoms *i* and N_A the Avogadro's number. The partial density ρ_i is a fraction of the total sample densityρ: $\rho_i = x_i \rho$. Using the usual transformation $dz = (dz/dE) \cdot dE$ and the density independent stopping power $dE/dz = \rho S(E)$, and realizing that $N_p = j_p 2Rlt$ is the total number of protons that hit the target segment *l*, we obtain for the detected number of X-rays *i*:

$$N_x^i = N_p \frac{\Delta\Omega}{4\pi} \varepsilon_i \eta_i \frac{N_A}{M_i} x_i \frac{1}{2R} \int_{-R}^{R} dy \int_{E_2(y)}^{E_1} \frac{\sigma_i(E) \exp(-\mu_i \xi)}{S(E)} dE \,. \qquad (35)$$

The double integral is essentially a typical thick target factor, averaged transversally (in y direction) for a cylindrical target. $E_2(y)$ is the proton exit energy; if the target is sufficiently thick, the protons may stop in the target and E_2 is set to zero. The calculation of E_2 requires (besides the radius R) also a knowledge of the total target density ρ, which has to be determined by some other method. As the stopping powers and attenuation coefficients in Eqn (35) are matrix dependent, the concentrations x_i are evaluated from Eqn (35) by an iterative procedure.

The X-ray detector is positioned at an angle ϑ with respect to the beam. X-rays are leaving the target along the escape length ξ, which depends on the radius of the cylinder R, and the coordinates u and v in the rotated coordinate system:

$$\xi = \sqrt{R^2 - v^2} - u \,. \qquad (36)$$

To get the coordinates u and v we have to rotate the coordinate system counter-clockwise by the angle $\pi - \vartheta$. The coordinates u and v are obtained by multiplying the coordinate (y, $\sqrt{R^2 - y^2} - z$) by the rotation matrix:

$$\begin{vmatrix} v \\ u \end{vmatrix} = \begin{vmatrix} \cos(\pi - \vartheta) & -\sin(\pi - \vartheta) \\ \sin(\pi - \vartheta) & \cos(\pi - \vartheta) \end{vmatrix} \begin{vmatrix} y \\ \sqrt{R^2 - y^2} - z \end{vmatrix} . \qquad (37)$$

The integration in Eqn (35) was performed by an 8-point Gaussian integration using the transformation [39] which densifies the integration points in the region where the integrand is large. If the proton beam is not homogeneous, the integrand in Eqn (35) should also contain the normalized transverse distribution of the proton current. The limiting cases of Eqn (35) are a very thin cylinder with no matrix effects, and a thick cylinder with a radius that surpasses the proton range by several orders of magnitude. The thick target factor in this case is then an average of the thick target factors obtained by slowly rotating a large plane target perpendicular to the beam. The thick target factor in Eqn (35) is typically larger than for a flat target.

2.5.5 Evaluation of the geometry impact

The cylindrical geometry influences only two parameters in Eqn (35). That is the escape length ξ and the exit energy E_2. Three sets of simulations have been done to evaluate the influence of these two parameters:

a.) A concise cylindrical model as presented in Eqn (35) using Eqn (36) for the calculation of the escape length ξ and the calculation of E_2 for each dy.

b.) A calculation of the ribbon geometry. The escape length ξ is calculated as in a thick target (Eqn (29)). The exit energy E_2 corresponds to E_2 in a model a) at a depth of $2R$ and is constant across the ribbon. The geometrical cross-section is a square. The edge effects for absorption are not calculated.

c.) Calculation of a reduced ribbon geometry. The escape length ξ is calculated as in

a thick target (Eqn (29)). The area of the geometrical cross-section is the same as the area of a circle used in the model a). The energy E_2 corresponds to E_2 in a model a) at a depth of $\sqrt{\pi}\,R$ and is constant across the ribbon. The cross-section is a square. The edge effects for absorption are not calculated.

The advantage of models b) and c) is that they can be implemented in the programs for the calculation of concentrations like Gupix [70] or NDF [160], since they represent a section of the layer with an intermediate thickness: the thin layer target at one end and the thick layer target at the other end.

Obviously all three models will give different results for different diameters of the fibre. Also the orientation of the fibre with respect to the detector is important. The highest influence of the cylindrical geometry is in the case where the fibre is perpendicular to the plane stretched by the beam and detector directions. When a fibre lies in this plane and perpendicular to the beam, the model b) describes the geometry influence adequately.

For the purpose of simulation, an imaginary sample of cotton with a few percent of trace elements (Si, Ca, Ti, Fe, Cu, Br) was selected. The concentrations were calculated using the models a), b), and c). The ratio between concentrations is shown in Figure 22 (b vs. a) and Figure 24 (c vs. a).

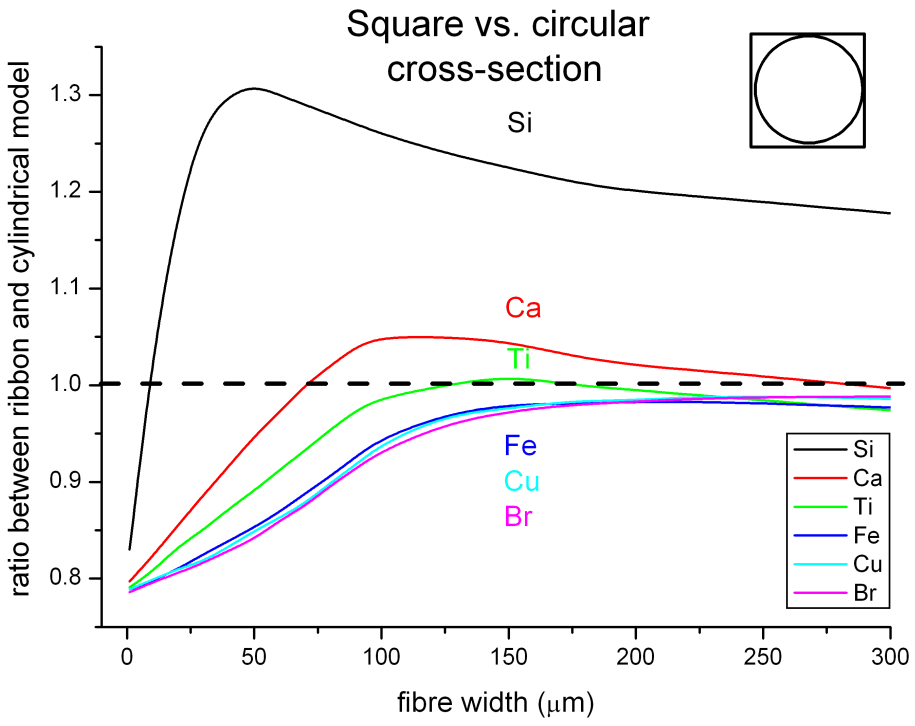

Figure 22: *The influence of cylindrical geometry*. The model for the cylindrical target was compared to the simpler model of ribbon geometry, assuming a square cross-section with a side of 2*R*. Much higher concentrations in a target are assumed with the light elements (Si, Ca) when the ribbon geometry model is used, however when the diameter of a cylindrical target approaches zero, the concentrations calculated with ribbon geometry model are underestimated due to difference in the area of the cross-section (square vs. circle area, where side of a square is a diameter of a circle).

The largest difference in the ratios between the concentrations of Si and Br at 50 μm fibre width is 56%. The maximum difference for calcium was lower, 14% at a fibre width of 90 μm. The range of 3 MeV protons in the sample (cotton matrix with trace elements) calculated with SRIM2008 is 101 μm, which is twice the diameter of the fibre.

At the diameters of the cylinder close to zero, the effect of X-ray absorption diminishes, so only the amount of material irradiated is important. Thus the ratio between both models for all elements approaches the number 0.785 which is the ratio between the areas of a circle with radius R and a square with a side $2R$. The model of a ribbon for thicknesses much smaller than the range of projectiles thus translates into the model of a thin target. To avoid the effect of a larger cross-section of ribbon model compared to the model of a cylinder at dimensions close to zero, we should equal the cross-sectional area of both models (Figure 23). We repeat the calculation for the square ribbon of the dimensions:

$$a^2 = \pi R^2 = \pi D^2 / 4 \Rightarrow a = \sqrt{\pi}\, R = \tfrac{1}{2}\sqrt{\pi}\, D\,.$$

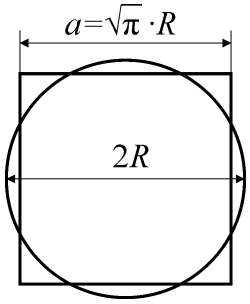

Figure 23: *The improved ribbon model vs. model of cylindrical geometry*. The area of both cross-sections are the same.

The ratio of concentrations of the improved ribbon model versus the cylindrical model is shown in Figure 24.

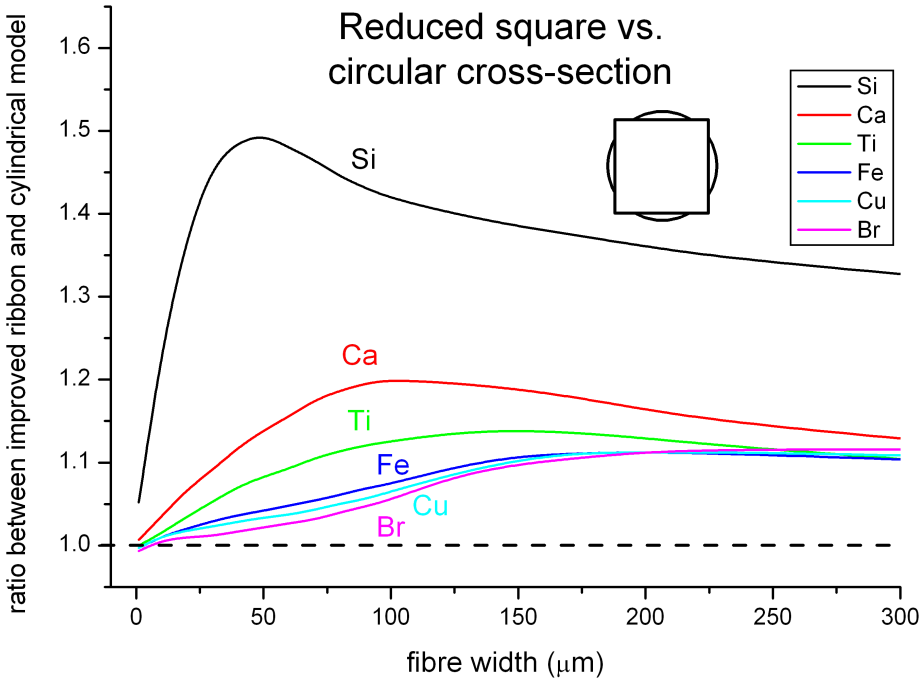

Figure 24: *The improved ribbon model vs. cylindrical geometry model*. The model for a cylindrical target was compared to an improved ribbon model. The cross-section area of both mathematical models are the same. The concentrations calculated with the improved ribbon model are overestimated, but accurate when the diameter approaches zero. The largest difference is with lightest elements (Si, Ca).

The evaluated concentrations in fibres of diameters close to zero in the improved ribbon model are practically the same as in the rigorous cylindrical geometry model. The differences increase with a fibre thickness and attain a maximum at a radius of 50 μm. For thicker fibres they are smaller, as we approach the plane thick target geometry. At the maximum, the highest difference of 47% was found for silicon that emits soft X-rays of 1.74 keV energy, 12% for calcium emitting 3.69 keV photon.

The improved ribbon model can in principle be improved further with the inclusion of the edge effects; this is correction of the absorption due to the limited width of the fibre, but in this case the use of a dedicated program is required. When a dedicated program is used, it is better to implement a more appropriate cylindrical geometry model described earlier. However, such dedicated programs are much more complex than the cylindrical model, as they require more geometrical parameters.

2.5.6 The beam profile

For a model as close to the real parameters as possible it is necessary to take into account also the shape of the beam. The beam is collimated in vacuum either by a square or by a circular collimator. After the collimation the beam passes a thin metal foil separating the vacuum and the air at room pressure, resulting in a substantial angular straggling, which is further increased in the air path between the foil and the target. An infinitely small beam with N_p projectiles would spread into a spot with the corresponding projectile areal density $P' = j_p \cdot t$ with a Gaussian profile of the width σ':

$$P' = \frac{N_p}{2\pi\sigma'^2} e^{-\frac{r^2}{2\sigma'^2}} \tag{38}$$

The areal density P for a broad primary beam is then obtained by a convolution of the distributions (Eqn (38)) across the beam area before the exit foil. For a circular collimator, the integration across the beam area is straight forward. The complete circle is divided into small areas dS that contribute dN_p projectiles to the projectile areal density P (Figure 25 [62]).

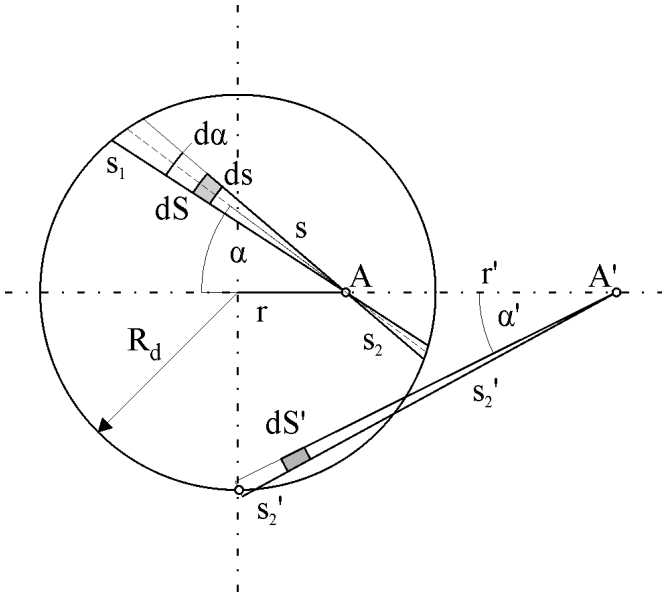

Figure 25: *The model for the calculation of the projectile density P* on the target for a broad exit collimator of radius R_d. Area fractions dS contribute dN_p to the projectile areal density. [62]

The radius of the collimator (diaphragm) is R_d. The proton density distribution is assumed to be homogeneous, so each dS emits dN_p = N_p dS/πR_d^2 projectiles. After an integration by dS = s ds dα (Figure 25), we find that the projectile areal density at the target depends only on the distance from the centre r:

$$P = \frac{N_p}{\pi R_d^2}\frac{1}{\pi}\begin{cases} \displaystyle\int_0^{\pi/2}\left(2-\exp\left(-\frac{s_1^2}{2\sigma'^2}\right)-\exp\left(-\frac{s_2^2}{2\sigma'^2}\right)\right)d\alpha \\ s_{1,2} = \sqrt{R_d^2 - r^2\sin^2\alpha} \pm r\cos\alpha \qquad r \geq R \\ \displaystyle\int_0^{\arcsin(R_d/r)}\left(\exp\left(-\frac{s_2^2}{2\sigma'^2}\right)-\exp\left(-\frac{s_1^2}{2\sigma'^2}\right)\right)d\alpha \\ s_{1,2} = \pm\sqrt{R_d^2 - r^2\sin^2\alpha} + r\cos\alpha \qquad r \geq R_d \end{cases} \tag{39}$$

Eqn (39) distinguishes two cases, one is where the spot A is in the geometrical shade of the primary beam ($r \leq R_d$), and the other is where the spot A' of the target is out of the geometrical shade of the primary beam ($r \geq R_d$). An integration over α is done numerically. The distribution P from Eqn (38) tends towards the Gaussian with decreasing values of R_d/σ' (Figure 26). The experimental beam profiles were measured by scanning a thin metal wire across the beam and detecting the induced rays. The values can

be well fitted with a Gaussian function. Consequently, a pure Gaussian distribution was assumed in the subsequent evaluation of the measured data. The width of the beam always depends upon σ', which is influenced by the thickness and the material of the exit window, as well as the air gap.

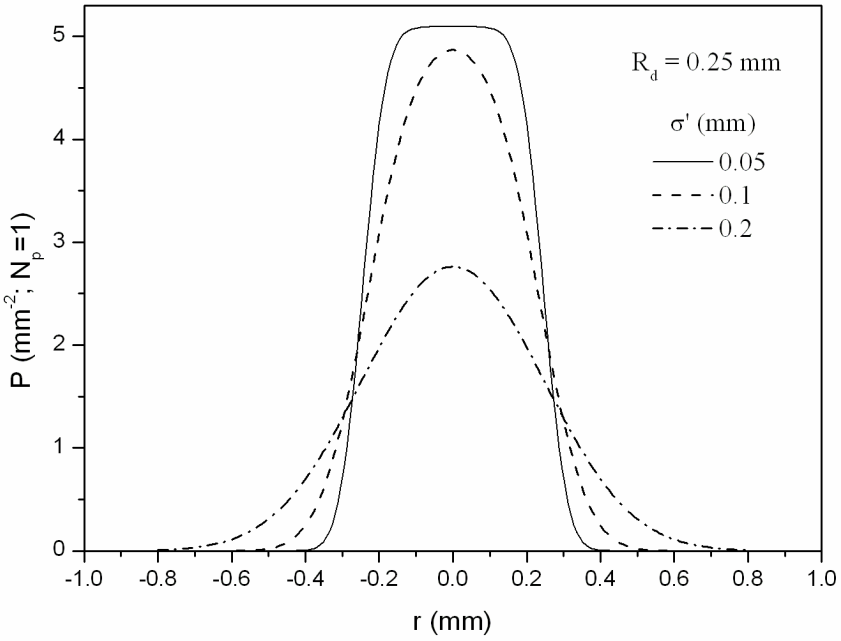

Figure 26: *The calculated projectile areal density at the target.* The primary beam diameter was 0.5 mm and three different values of σ' were assumed. The distribution tends towards a Gaussian with a decreasing R_d/σ' ratio. [62]

2.5.7 Measurement of the beam profile with a metal wire

The beam profile was measured by scanning a 250 µm metal wire across the beam. The controlled horizontal displacement of the wire was done with a motorized XYZ stage. The smallest step of the motors was 1/125 mm. Two sets of measurements were made: 2.5 MeV protons were extracted into the air through two different windows. At a distance of 10 mm the protons hit a 0.25 mm thick copper wire. At the distance 5.5 cm from the target the X-rays were measured with a Si(Li) detector. No additional absorber was used. The results show that the beam-intensity profile is Gaussian with a fitted width (2σ) of 0.483 ± 0.005 mm for an 8 µm thick Al exit window (Figure 28) and 1.029 ± 0.003 mm for a 2 µm thick Ta exit window (Figure 29). The beam profile obtained with the Ta window was normalized using two different methods, with Ar in the air and with a chopper intersecting the beam between the exit window and the target (Figure 27), revolving with a frequency of approximately 2 Hz. The normalization did not cause much difference in the measured width of the beam (1.029 ± 0.003 mm vs. 1.070 ± 0.004 mm with normalization according to the chopper), however, Ar normalization was affected by the wire geometrically shadowing the beam and thus reducing the Ar signal (Figure 30). The wire was also preventing a part of the Ar signal, in its geometrical shadow towards the detector, from being measured.

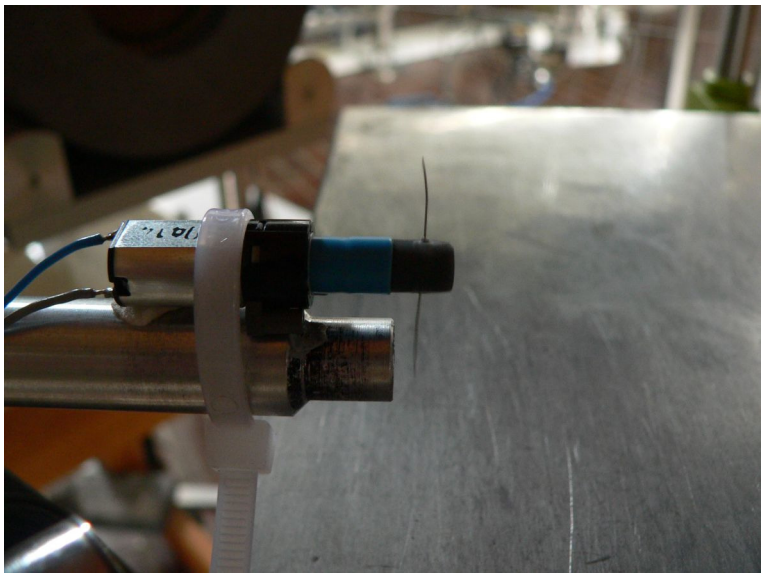

Figure 27: *The external chopper with Ti wire at MIC, JSI*, used as an alternative to the Ar dose measurement, before the in-vacuum wire-mesh was installed.

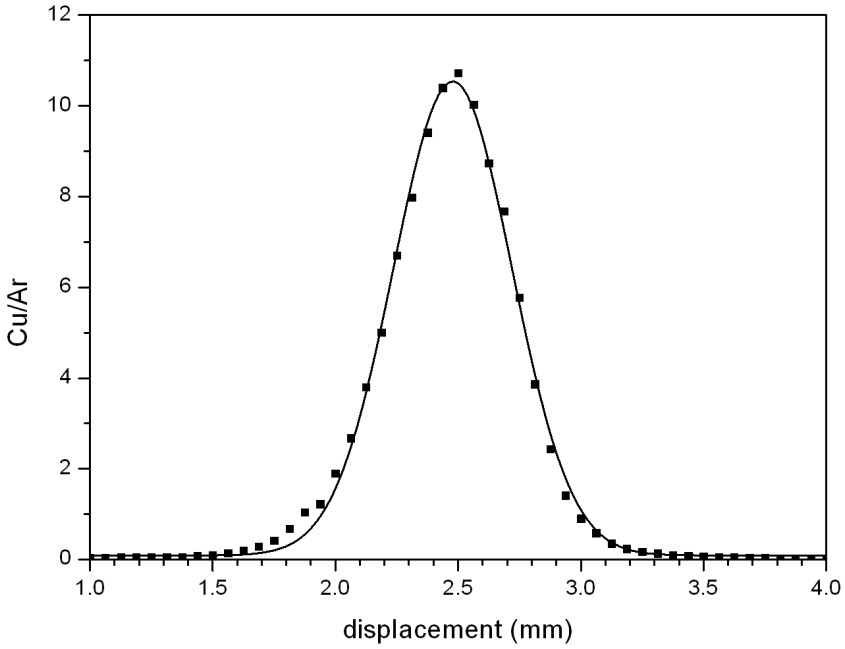

Figure 28: *The measured beam profile for an 8 μm aluminium exit window* and a 1 cm air gap at the position of the target. Fitted width (2σ) is 0.483 ± 0.005 mm. [62]

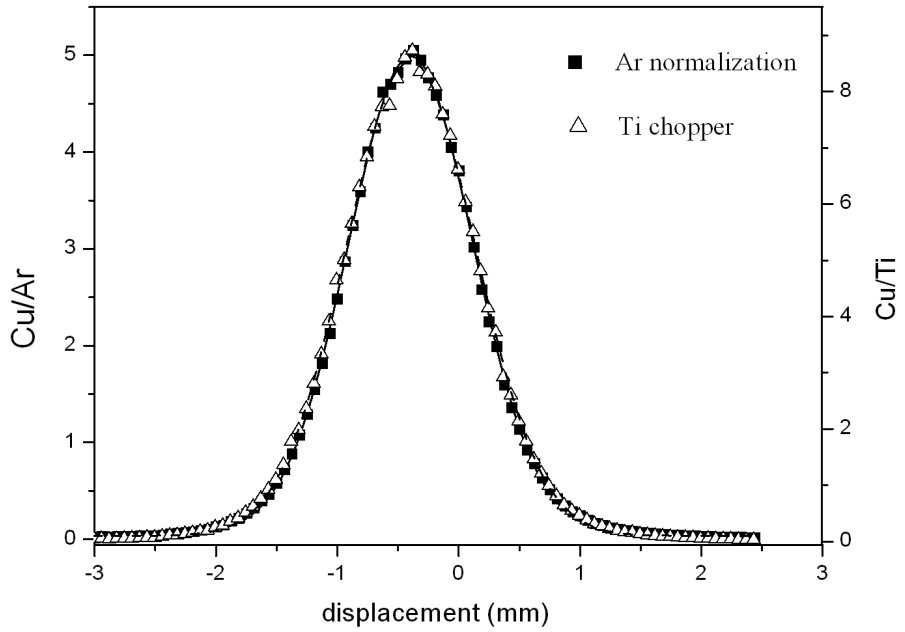

Figure 29: *The measured beam profile for a 2 μm tantalum exit window* and a 1 cm air gap at the position of the target. Normalized according to the Ar signal from the air and the signal from the in-air chopper. The fitted widths (2σ) are 1.029 ± 0.003 mm and 1.070 ± 0.004 mm, accordingly. [62]

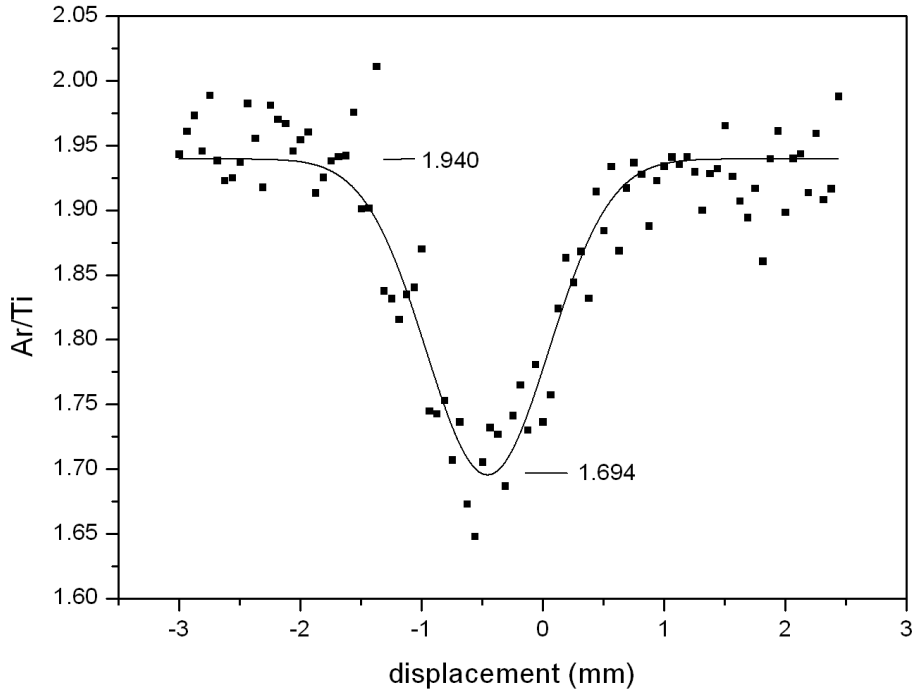

Figure 30: *The ratio between the X-ray intensities from the air argon and titanium chopper*. The wire shadows the Ar signal, but the Ti signal from the chopper is independent of the wire position. The line is a fitted Gaussian. [62]

2.5.8 Cylindrical target in a Gaussian-type beam

The integral in Eqn (35) is appropriate if the beam is homogeneous and N_p is the number of all the protons hitting the target. In reality, only a fraction of the beam hits the target, so N_p is calculated as:

$$N_p = N_p^{tot} \frac{2R}{a}, \tag{40}$$

where N_p^{tot} is the total number of protons in the beam and a is the width of a homogeneous beam. Due to angular scattering in the exit window and atmosphere the beam profile tends towards a two-dimensional Gaussian distribution:

$$N_p^{tot} = \int j_p dS; \qquad j_p = N_p^{tot} \frac{1}{2\pi\sigma^2} e^{\frac{-x^2-y^2}{2\sigma^2}} \tag{41}$$

The fibre is assumed to be parallel with the axis x and centred at $y = 0$. The number of detected X-rays, combining all the parameters that depend on the transverse coordinate y only in the function $F(y)$, reduces to:

$$Y_i \propto \frac{N_p^{tot}}{2R} \int_{-R}^{R} F(y) \sqrt{\frac{2}{\pi}} \frac{R}{\sigma} e^{\frac{-y^2}{2\sigma^2}} dy \tag{42}$$

When σ is large, the exponential function approaches unity. Moving the constants $\sqrt{2/\pi}\,R/\sigma$ can be moved out of the integral we find:

$$Y_i \propto \frac{N_p^{tot}}{\sqrt{2\pi}\,\sigma} \int_{-R}^{R} F(y)\, dy \tag{43}$$

The function $F(y)$ is a shorthand notation for the integral from Eqn (35).

$$F(y) = \int_{E_2(y)}^{E_1} \frac{\sigma_i(E) \exp(-\mu_i \xi)}{S(E)} dE \tag{44}$$

The integration of $F(y)$ across the cylinder gives us the thick target factor T_i^c for an element i in the cylindrical target. The detected number of X-rays i (35) now translates into the formula:

$$N_x^i = N_p^{tot} \sqrt{\frac{2}{\pi}} \frac{R}{\sigma} \frac{\Delta\Omega}{4\pi} \varepsilon_i \eta_i \frac{N_A}{M_i} x_i T_i^c . \tag{45}$$

The number of protons N_p^{tot} is proportional to a proton dose D as measured by one of the current measurement techniques described in the previous chapters.

$$N_p = k \cdot D . \tag{46}$$

The product of constants $\frac{\Delta\Omega}{4\pi} N_A k$ can now be combined into a new instrumental constant H which is supposed to be constant for all energies and thus all elements. The number of detected X-rays is now:

$$N_x^i = H \cdot D \cdot \frac{\varepsilon_i \eta_i}{M_i} x_i T_i^c \begin{cases} \frac{2R}{a}; & homogeneous\ \ beam \\ \frac{2R}{\sqrt{2\pi\sigma}}; & Gaussian\ \ beam \end{cases} . \tag{47}$$

Some uncertainties in the detector efficiency ε_i and the transitivity of X-rays η_i can also be compensated by replacing the instrumental *constant H* with an energy dependent *function H*.

The instrumental constant H was first introduced by J. L. Campbell in Gupix, PIXE spectra evaluation program [161]. For flexibility reasons (when the detector response is not very well known) the H constant in the current Gupix version can be set as a function of the measured X-ray energy.

2.5.9 The determination of the instrumental constant *H*

The instrumental constant H combines the geometric solid angle of the X-ray detector and any systematic normalization factor in the proton-dose normalization system. In practice, with a well defined detector, the instrumental constant is indeed approximately constant for the K series X-rays from elements in the range from calcium to tin (20<Z<50) [162]. A calibration for the measurement performed at the University of Surrey was adequate even down to silicon (Z=14). The calibration with various mono-elemental targets and/or standards with known concentrations can be performed and the instrumental constant H can be applied in further measurements if it does not differ much for different elements.

The H constant does not depend on the sample geometry, so it can be determined separately using a flat standard, preferably with a similar composition as the measured samples. Since silicon is the lightest element in fibres and thus the most sensitive to the absorption, it was important to compare its yield to the standard. Glass standards always contain a large amount of silicon, so we also used it for our measurements. The calculation of the instrumental constant has been made for measurements at the University of Surrey and for measurements at the Jožef Stefan Institute.

2.5.9.1 *H* value calibration at the University of Surrey

At the external beamline at the University of Surry, a lead glass standard BCR® 126A [163] was used, its composition is given in the certificate shown below.

Table 1: *BCR® - 126A lead glass certified reference material*. The mass fraction of oxides contained in a glass standard, and its density at 20 °C. [163]

CERTIFIED REFERENCE MATERIAL

BCR® - 126A (lead glass)

Mass Fraction				
	Certified value [1]	Uncertainty [2]	Unit	p
SiO_2	57.80	0.11	g/100 g	11
PbO	23.98	0.06	g/100 g	14
K_2O	9.99	0.07	g/100 g	9
Al_2O_3	0.126	0.013	g/100 g	8
Fe_2O_3	0.0055	0.0012	g/100 g	8
Sb_2O_3	0.291	0.012	g/100 g	7
BaO	1.053	0.030	g/100 g	13
CaO	1.033	0.030	g/100 g	8
MgO	0.512	0.013	g/100 g	8
ZnO	1.01	0.04	g/100 g	8
Na_2O	3.57	0.07	g/100 g	8
Li_2O	0.494	0.016	g/100 g	7
Physical properties				
	Certified value [1]	Uncertainty [2]	Unit	p
Density at 20 °C	2.9905	0.0016	g/cm^3	10

1) Unweighted mean value of the means of p accepted sets of data, each set being obtained in a different laboratory and/or with a different method of determination. The certified value and its uncertainty are traceable to the International System of Units (SI).
2) The certified uncertainty is the half-width of the 95% confidence interval specified in 1).

European commission, Joint research centre
Institute for Reference Materials and Measurements

The parameters of the beamline (detector filter, air gap to the detector) were optimized, so the calculated concentrations approached the certified values as much as possible. The results of an evaluation using the BCR 126A standard can be seen in the table below:

Table 2: *H value calibration*, performed on a lead glass BCR 126A at IBC, University of Surrey.

Element	Energy of the characteristic peak (keV)	measured instrumental constant	discrepancy of the deduced concentration from the certified values
Si (K)	1.740	123.1	0.947
K (K)	3.313	121.7	0.936
Ca (K)	3.691	139.1	1.070
Zn (K)	8.631	153.6	1.182
Sb (L)	3.604	133.2	1.025
Ba (L)	4.464	113.7	0.875
Pb (L)	10.542	125.6	0.966
mean		**130.0** ± 13.24	1.000 +/- 0.102

The mean calibration factor of 130 ± 13 was determined for all the measured elements (Si, K, Ca, Zn, Sb, Ba and Pb) with the highest deviation of 18% for Zn. Iron was not

included in the calibration due to its low concentration, high uncertainty and the known issue of the non homogeneous distribution in the reference material. With deviations in this range it is safe to use the mean calibration factor for all elements.

2.5.9.2 *H* value calibration at the Jožef Stefan Institute

At the external beamline at the Jožef Stefan Institute a NIST 620 [164] glass was used; its composition is transcribed from the certificate in the table below.

Table 3: *NIST 620 soda-lime flat glass certified reference material*. The mass fraction of oxides contained in a glass standard. [164]

National Bureau of Standards
(in cooperation with American society for testing and materials)

Standard Reference Material 620
NIST - 620 (Soda-Lime Flat Glass)

Mass Fraction			
	Certified value	Uncertainty	Unit
SiO_2	72.08	0.08	g/100 g
Na_2O	14.39	0.06	g/100 g
CaO	7.11	0.05	g/100 g
MgO	3.69	0.05	g/100 g
Al_2O_3	1.80	0.03	g/100 g
K_2O	0.41	0.03	g/100 g
SO_3	0.28	0.02	g/100 g
As_2O_3	0.056	0.003	g/100 g
Fe_2O_3	0.043	0.004	g/100 g
TiO_2	0.018	0.002	g/100 g

The parameters of the beamline (detector filter, air gap to the detector) were optimized, so the calculated concentrations approached the certified values as much as possible. The results of an evaluation using the NIST 620 standard can be seen in the table below.

Table 4: *H value calibration*, performed on a soda-lime glass NIST 620 at MIC.

Element	Energy of the characteristic peak (keV)	measured instrumental constant	discrepancy of the deduced concentration from the certified values
K (K)	3.313	3.884E+07	1.016
Ca (K)	3.691	3.128E+07	0.819
Ti (K)	4.510	4.179E+07	1.094
Fe (K)	6.403	3.290E+07	0.861
As (K)	10.543	4.624E+07	1.210
mean		**3.821E+07** +/- 2.774E+06	1.00 +/- 0.162

The mean instrumental constant of 3.821e7 ± 0.277e7 was determined for the elements from K (3.313 keV) to As (10.543 keV). The highest measured deviation of 21% was observed for As.

2.5.10 The PIXE experimental setup

PIXE measurements were made with a liquid-nitrogen-cooled Si(Li) detector with an energy resolution of 160±5 eV at the energy of the Mn K-α peak (5.898 keV). The detector was positioned 55 mm away from the target, which was 10 mm away from the exit window at an angle 45° to the beam. Between the detector and target there was air. With this setup we can measure elements heavier than Si. The experimental setup is shown in Figure 31.

The signal from the detector preamplifier is led to the NIM crate (Nuclear Instrumentation Module) to be amplified and converted into digital signal, then a Canberra multi channel analyzer (MCA) in a form of a PC card is used to collect the spectrum. An MS-DOS program Axil [165, 166] enables the collection, saving and fitting of the spectra. After the fits are obtained, the concentrations are calculated using dedicated programs written in the Pascal programming language.

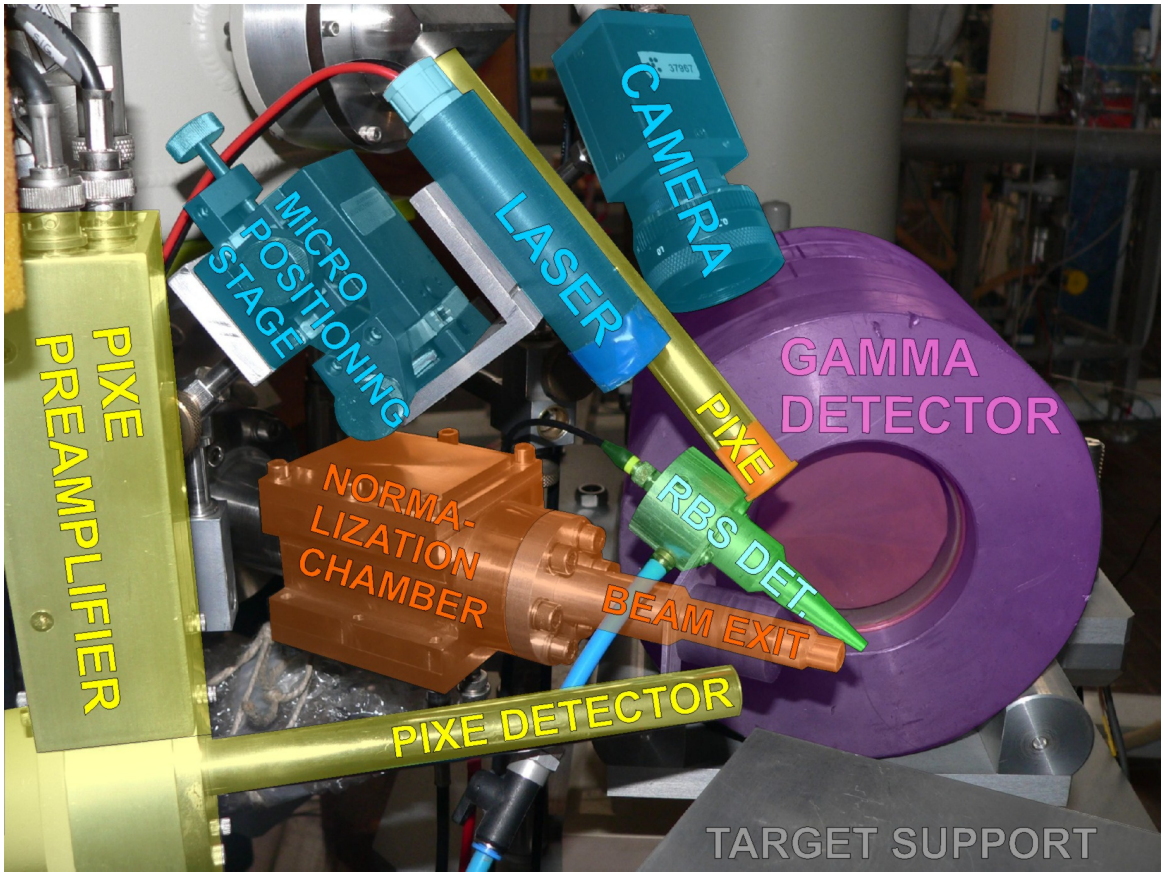

Figure 31: *The external beam experimental setup at Microanalytical center at Jožef Stefan Institute* with the PIXE, PIGE and RBS detectors. Normalization chamber with the wire-mesh-based charge-collecting device is seen, as well as the positioning system with a camera and a laser fixed on a micro-positioning stage.

For heavier elements (starting with Fe) we increase the proton current and use filters in front of the detector, in order to reduce the signal from the light elements. Kapton filters with thicknesses variable in steps of 50 μm were used and sometimes a 100 or 300 μm Al filter, depending on the required absorption of low energy X-rays. The transmission of X-rays [167] at different energies can be seen in Figure 32.

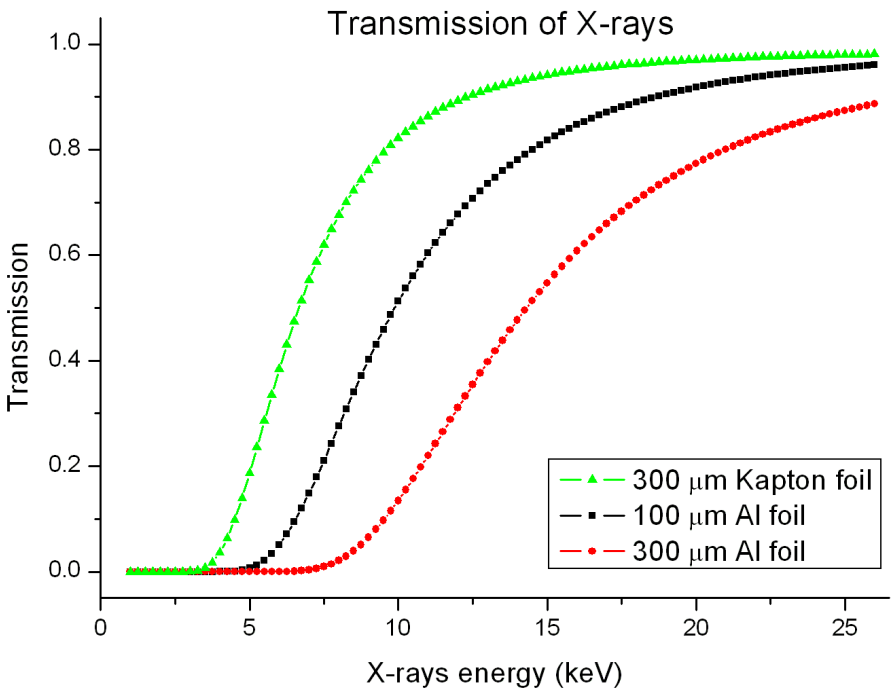

Figure 32: *X-ray transmission of various filters*. X-ray transmission of a 100 μm and 300 μm Al foil and a 300 μm Kapton® ($C_{22}O_5N_2H_{10}$) polymer foil. [167]

2.5.11 The PIXE measurement uncertainty

The parameters which have the strongest influence on the PIXE measurement in air are: the exit window thickness, the distance to the target, the air density, the standard material composition uncertainty, and the proton dose uncertainty. Later, I will discuss each of them.

The exit window has a strong influence on the proton beam. Protons in the material lose part of their energy and also their energy distribution becomes wider due to energy straggling, thus it is important to know the thickness of the exit foil. Typically an 8 μm aluminium exit window lasts several 100 hours of measurements, and a 2 μm tantalum window even longer. So, the exit window thickness is not expected to change during a set of measurements, unless the window breaks and has to be replaced. In this case an additional calibration is necessary.

The distance to the target is probably the most critical of the parameters. Protons are being decelerated by the atmospheric atoms and molecules, thus losing energy. A 3 MeV proton travelling 1 mm in air loses around 13 keV of energy. The variation in the distance to the target also coincides with the variation in the distance to the detector, which means higher absorption. Both effects lead to a lower yield of detected elements, thus a lower measured concentration than expected. This is the only parameter which is different for every sample; moreover, positioning of the previous sample is unrelated to the positioning of the next one.

The air density (atmospheric pressure) has an influence on the PIXE measurements since it changes the attenuation of the X-rays as well as stopping of the protons in air. However, it stays constant within 4% (40 mbar variation of atmospheric pressure around 1 bar in the worst case) during a set of measurements if they are made in one day. So the influence of the air density is included in the instrumental constant *H*.

The standard material which we use for the calibration at least once in a set of measurements is a material with a well known composition, measured many times with various techniques. The uncertainty of standard material composition is given in a certificate. Sometimes, the amount of a certain element in the standard material is close to the detection limit, so the uncertainty is relatively high, in this case another standard should be used for the calibration of that element.

The proton-dose uncertainty depends on the method of measuring the proton dose. With a wire-mesh we got very good results, the charge collected was measured with a charge integrator and digitally measured with an uncertainty of ±1 of the preset unit of charge, typically more than 100 preset units of charge were collected per measurement. The argon calibration takes into account the signal in the Ar peak in the spectrum, obeying a law of counting statistics, which means that for an uncertainty of 3% more than 1000 counts should be collected, and 10000 for a statistical uncertainty of 1%. However, the proton number directly affects only the absolute concentrations, the ratios between elements remain constant regardless of the proton dose. But care should be taken when doing the Ar normalization on a sample containing silver, since its Lα line coincides with the Ar Kα line, and also the thorium Mα line is located close to Ar Kα line.

The stability of the accelerator terminal voltage is better than 100 V at the terminal voltage of 1.5 MV, which means the proton beam energy variation due to the terminal voltage oscillations is insignificant and can be neglected.

Table 5 presents a list of parameters influencing the uncertainty of the measurements.

Table 5: List of parameters and their influence on the absolute and relative results of the measurements, done at the University of Surrey.

parameter	absolute uncertainty	relative uncertainty [%]	uncertainty of absolute results [%]	uncertainty of relative results to Ti [%]
exit window thickness (Kapton)	8 ± 1 μm	±12.5	3.4 (Cu)	1.9 (Si)
distance to the target	4.5 ± 0.25 mm	±5.5	0.70 (Fe)	0.45 (Si)
air density	1.176-1.224 g/dm^3 1000 ± 40 mbar	±4	7.5 (Si) 1.7 (Ca)	6.6 (Si) 0.76 (Ca)
proton dose - chopper	500000 ± 707 (counts)	±0.15	±0.15	<0.01 (negligible)
Stability of beam energy	1.5 MV ± 100 V	<0.01 (negligible)	<0.01 (negligible)	<0.01 (negligible)
sum or squares			3.87	2.10
max. geometrical uncertainty cylinder vs. plane target			30% (Si)	Si/Br = 56% (at diameter with maximal effect)

Table 6: List of parameters and their influence on the absolute and relative results of the measurements, done at the Jožef Stefan Institute.

parameter	absolute uncertainty	relative uncertainty [%]	uncertainty of absolute results [%]	uncertainty of relative results to Ti [%]
exit window thickness (Al foil)	8 ± 1 μm	±12.5	3.6 (Cu)	1.2 (Cu)
distance to the target	10 ± 0.25 mm	±2.5	4.2 (Mn)	0.3 (Mn)
air density	1.137-1.183 g/dm^3 960 ± 40 mbar	±4	1.2 (Ca) 1.5 (Sb)	0.6 (Ca) 0.9 (Sb)
proton dose - argon	1600 ± 40 (counts)	±2.5	±2.5	<0.01 (negligible)
stability of beam energy	1.5 MV ± 100 V	<0.01 (negligible)	<0.01 (negligible)	<0.01 (negligible)
sum or squares			6.25	1.53
max. geometrical uncertainty Cu-(cylinder vs. plane target)			20% (Ca)	Ca/Cu = 14% (at diameter with maximal effect)

The distance to the target has the highest influence on the uncertainty of the measurement, because of the ~30% shadowing of the Ar signal by the exit nozzle [45]. For this reason, much care has to be put into the positioning of the sample. This error will be much reduced when other means of proton dose measurement will be utilized. The air density, however, does not have as high an impact as for the University of Surrey,

because silicon could not be measured at all due to the large distance (5.5 cm) to the detector, and due to 100 μm kapton absorber used for the measurements.

The parameter with largest impact, which was not included in the estimation of the measurement uncertainty, is the geometrical parameter, related to the diameter of the fibres. It is written in the tables above just to put it into perspective. The geometrical uncertainty for some of the most inappropriate cases can play a prominent role in the interpretation of results, especially when measuring the X-ray emission of low-Z elements, like silicon (1.74 keV) or calcium (3.69 keV), and should be investigated in more detail.

2.5.12 Reproducibility

For a measurement to be valuable in future studies it is important that it is reproducible. The PIXE method by itself is reproducible and as such useful in scientific studies. But on the other hand the sensitivity of the PIXE method is so high that it is important to know the uncertainties and detection limits so as not to over-interpret the data. Another thing important to know is the distribution of elements and the inhomogeneity of the sample.

3 Development of measuring equipment and procedures

3.1 Measurements of textile fibres

Textile fibres were measured at two different facilities using an in-air proton beam, and a proton micro-beam in vacuum. The samples were textile fibres extracted from the cloths, which were either treated with various dressings or not. The treated cloths were in most cases easily distinguished from the untreated cloths by their texture, but once a single thread was extracted from the cloth, the difference could not be observed any more. The aim of the measurements was to determine if the distinction could be made on the basis of the composition. We expect to perform more precise measurements with the ion-beam analytical methods than with the methods commonly used for such purposes (optical microscopy, SEM-EDS).

3.1.1 The textile fibre samples

The samples were single threads (yarns) extracted from the weaved cloths. If the warp and weft yarn were different, both were measured (Figure 33 [168]). Sometimes there was more than one warp yarn in a single cloth, in this case all used threads in the cloth were measured.

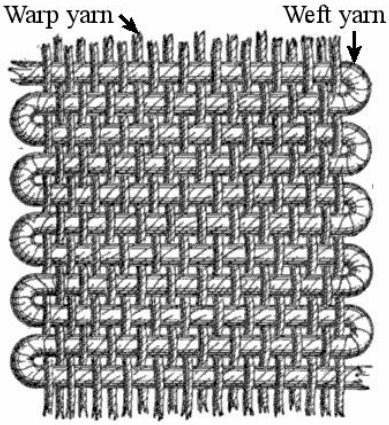

Figure 33: *The plain weaved cloth*. Warp and weft yarns (threads) are indicated. [168]

The cloths were treated with different dressings to achieve various properties of the tissue. The so-called "silver dressing" supposedly containing silver nano-particles was used to achieve an antibacterial effect and was compared to the Actigard® dressing. A one-side anti-slip dressing was used only on one side of the cloth to reduce the wettability of the cloth. The dressing with an unknown composition was used to increase the fire resistance. With the cloth of black colour the Teflon dressing was used to improve the properties. All the samples with the denoted treatment, material and colour are listed in Table 7. The texture of the threads in the standard notation for the textile industry is denoted, where the information was available.

Table 7: *Table of the textile fibre samples*. Various cloths are denoted with number and separate yarns from it with letters.

# of cloth	yarn	treatment	fibre material	fibre colour	fibre texture
1. Silver dressing (antibacterial)					
1	a	dressed	PES	white	167f96x2
	b	dressed	Cotton+Lycra	white	Nm24/1
	c	dressed	Cotton	gray	Nm30/1
	d	dressed	Cotton	white	Nm30/1
2	a	undressed	PES	white	167f96x2
	b	undressed	Cotton+Lycra	white	Nm24/1
	c	undressed	Cotton (brown)	brown	Nm30/1
	d	undressed	Cotton (white)	white	Nm30/1
2. Silver dressing (antibacterial)					
3		dressed 1	Cotton	light yellow	Nm 80/2
		dressed 1	Cotton	light yellow	Nm 80/2
4		dressed 2	Cotton	light yellow	Nm 80/2
		dressed 2	Cotton	light yellow	Nm 80/2
5		undressed	Cotton	light yellow	Nm 80/2
		undressed	Cotton	light yellow	Nm 80/2
Actigard (antibacterial)					
6	a	dressed	PES	white	167f96x2
	b	dressed	Cotton	green	Nm 20/1
	c	dressed	Cotton+Lycra	white	Nm 24/1
	d	dressed	PES	white	167f96x2
7	a	undressed	PES	white	167/96x2
	b	undressed	Cotton	green	Nm 20/1
	c	undressed	Cotton+Lycra	white	Nm 24/1
	d	undressed	PES	white	167f96x2
one-side anti-slip dressing					
8	a	dressed	PES	white	167x1
	b	dressed	Cotton	blue	Nm 20/1
9	a	undressed	PES	white	167x1
	b	undressed	Cotton	blue	Nm 20/1
fire resistant dressing					
10	a	dressed	PES	white	
	b	dressed	PES	yellow	
11	a	undressed	PES	white	
	b	undressed	PES	yellow	
Teflon dressing					
12	a	dressed	PES	black	
	b	dressed	Cotton	black	
13	a	undressed	PES	black	
	b	undressed	Cotton	black	

The fibres were measured at the external beamline at the Ion Beam Centre at the University of Surrey, and at the Microanalytical Center at the Jožef Stefan Institute in Ljubljana. The measurements using the micro-beam were also made in both places.

Both in-air beamlines at the University of Surrey and the Jožef Stefan Institute exhibit similar characteristics. The parameters of both beamlines are compared, side by side, in

the table below.

Table 8: External (in-air) beamline comparison.

institution	University of Surrey	Jožef Stefan Institute
department	Ion Beam Centre - IBC	Microanalytical Center - MIC
beamline type	external beamline	external beamilne
atmosphere	air	air
IBA method	PIXE	PIXE
detector type	Si(Li)-LN cooled	Si(Li)-LN cooled
airgap 1 (to the target)	4.5 mm	10 mm
airgap 2 (to the detector)	9.1 mm	55 mm
angle to the detector	45°	45°
detector window	12.5 µm Be	12.5 µm Be
detector filter	24 µm Kapton	no, Kapton, Al foil
detector resolution	160 eV @ 5.9 keV	160 eV @ 5.9 keV
lightest detectable element	Si	Ar
mapping?	yes, max. 3x3 mm	no
exit window	8 µm Kapton	8 µm Al
projectile energy	3021 keV	3021 keV
beam diameter	1) 0.3 mm, 2) mapping over 1x1 mm	1 mm
beam shape	1) circle (measurement in a point), 2) square (mapping over 1x1 mm)	circle
beam profile	1) presumably Gaussian, 2) homogeneous square	Gaussian
proton dose normalization	chopper	Ar signal in the air, chopper, wire mesh charge collection

The samples were measured with a 3021 keV proton beam, and at IBC the scan over an area of 1x1 mm was performed to simulate a square homogeneous beam. Of course in reality the beam is convoluted with a 300 µm FWHM Gaussian type beam, but the error made by assuming a homogeneous square beam is small enough to be neglected in the calculations. The concentrations of trace elements in a cotton matrix of the textile fibres were calculated using the model of a cylindrical target and the model of a ribbon with a square cross-section (Figure 22). The measurements are collected in Table 9-10.

Table 9: PIXE measurements of textile fibres measured at the University of Surrey, concentrations in mass% were calculated with a cylindrical target model.

sample	1a	1b	1c	1d	2a	2b	2c	2d	3		4		5		6a	6b	6c
matrix	PES	Cotton +Lycra	Cotton	Cotton	PES	Cotton +Lycra	Cotton	Cotton	Cotton		Cotton		Cotton		PES	Cotton	Cotton +Lycra
density	1.38	1.55	1.55	1.55	1.38	1.55	1.55	1.55	1.55		1.55		1.55		1.38	1.55	1.55
width [µm]	550	450	300	300	550	350	300	300	350	350	300	300	300	300	400	350	300
measurement	56	57	59	60	61	62	63	64	65	66	67	68	69	70	71	72	73
Si	0.866	3.52	1.52	3.26	0.0813	0.0559	0.0326	0.146	0.0887	0.0664	0.148	0.0579			0.360	0.683	0.898
P									0.397	0.437	0.217	0.481	0.0852	0.191	0.218	0.294	0.291
S		0.239	0.483	0.263	0.224	0.206	0.500	0.202	0.286	0.323	0.268	0.353	0.209	0.256	0.182	0.231	0.169
Cl	0.326	0.987	0.746	0.959	0.209	0.292	0.214	0.203	0.226	0.251	0.202	0.236	0.384	0.466	0.283	0.528	0.366
K		0.364	0.235	0.352	0.0574	3.65	0.0878	0.141	0.0948	0.111	0.0958	0.123	3.58	2.99	0.0969	0.224	0.126
Ca	0.0778	0.674	0.732	0.553	0.0796	0.522	0.747	0.538	0.848	0.838	0.661	0.945	0.458	0.440	0.0761	0.365	0.0998
Ti	1.30	0.0787	0.0436	0.0656	1.04	0.0058	0.0051	0.0023	0.0351	0.0310	0.0259	0.0402	0.0022	0.0024	1.57	0.0030	1.90
Mn															0.0443		0.0588
Fe		0.0089	0.0313	0.0310	0.0078	0.0336	0.0357	0.0128	0.0039	0.0117	0.0185	0.0194	0.0329	0.0232	0.0015	0.0182	0.0111
Ni																	
Cu			0.100				0.0453						0.0038			0.0479	
Zn				0.0158	0.0039									0.0040			
Br																	

Continues on the next page.

sample	6d	7a	7b	7c	7d	8a	8b	9a	9b	10a	10b	11a	11b	12a	12b	13a	13b
matrix	PES	PES	Cotton	Cotton +Lycra	PES	PES	Cotton	PES	Cotton	Cotton	PES	Cotton	PES	PES	Cotton	PES	Cotton
density	1.38	1.38	1.55	1.55	1.38	1.38	1.55	1.38	1.55	1.55	1.38	1.55	1.38	1.38	1.55	1.38	1.55
width [µm]	550	500	350	400	550	300	450	250	400	375	550	300	500	200	400	200	400
measurement	79	84	81	82	83	85	86	87	88	89	90	91	92	93	94	95	96
Si	1.50	0.199	0.591	0.236	0.0876	1.41	2.90	0.126	0.0392	0.0103	0.0142	0.127	0.131	0.0745	0.0747	0.0935	0.0190
P	0.889	0.165	0.360	0.308	0.271	0.728	1.24	0.241	0.515	0.0921	0.252	0.488	0.150	0.211	0.521	0.121	0.309
S	0.252	0.326	0.714	0.511	0.320	0.447	0.968	0.762	0.824	0.475	0.629	0.577	0.161	0.400	2.96	0.348	1.75
Cl	0.945	0.328	0.435	0.428	0.271	0.455	0.306	0.623	0.290	0.302	0.354	0.505	0.197	1.43	0.442	1.51	0.282
K	0.456	0.105	0.234	0.207	0.0838	0.153	0.179	0.225	0.111	0.113	0.0917	0.140	0.0352	0.0634	0.112	0.109	0.0777
Ca	0.953	0.160	0.935	0.682	0.0747	0.283	0.943	0.239	1.16	0.0914	0.0684	0.209	0.0404	0.296	1.71	0.113	0.809
Ti	0.0150	2.46	0.0066	0.0111	2.06	1.89	0.0098	0.0288	0.0071	0.966	1.42	1.89	1.00	0.426	0.0072	0.472	0.0084
Mn		0.0686			0.0613	0.0037								0.0320		0.0216	
Fe	0.0203	0.0154	0.0213	0.0260	0.0075	0.0080	0.0270	0.0493	0.0148	0.0118	0.0046	0.0343	0.0041	0.0231	0.0255	0.0237	0.0161
Ni				0.0022													0.0042
Cu	0.0126		0.0962	0.0108			0.257		0.309								
Zn	0.0209			0.0270				0.0279						0.0371		0.0357	
Br														1.09		1.36	

Table 10: PIXE measurements of textile fibres measured at the University of Surrey, concentrations in mass% were calculated with a ribbon target model with a square cross-section.

sample	1a	1b	1c	1d	2a	2b	2c	2d	3		4		5		6a	6b	6c
matrix	PES	Cotton +Lycra	Cotton	Cotton	PES	Cotton +Lycra	Cotton	Cotton	Cotton		Cotton		Cotton		PES	Cotton	Cotton +Lycra
density	1.38	1.55	1.55	1.55	1.38	1.55	1.55	1.55	1.55		1.55		1.55		1.38	1.55	1.55
width [µm]	550	450	300	300	550	350	300	300	350	350	300	300	300	300	400	350	300
measurement	56	57	59	60	61	62	63	64	65	66	67	68	69	70	71	72	73
Si	0.978	3.99	1.76	3.77	0.0918	0.0642	0.0378	0.1700	0.1030	0.0769	0.172	0.0672			0.413	0.784	1.04
P									0.4610	0.5070	0.253	0.559	0.0991	0.222	0.250	0.339	0.340
S		0.270	0.558	0.308	0.243	0.232	0.568	0.229	0.327	0.369	0.305	0.404	0.238	0.292	0.205	0.261	0.195
Cl	0.338	1.07	0.825	1.08	0.216	0.3110	0.231	0.219	0.245	0.273	0.219	0.257	0.416	0.505	0.302	0.568	0.402
K		0.360	0.238	0.362	0.0544	3.58	0.0873	0.140	0.0946	0.111	0.0953	0.123	3.57	2.98	0.0950	0.221	0.127
Ca	0.0727	0.648	0.725	0.554	0.0741	0.509	0.729	0.524	0.829	0.820	0.646	0.925	0.456	0.436	0.0732	0.353	0.0981
Ti	1.21	0.0739	0.0423	0.0641	0.968	0.0055	0.0049	0.0023	0.0340	0.0300	0.0251	0.0389	0.0021	0.0023	1.50	0.0029	1.84
Mn															0.0425		0.0569
Fe		0.0085	0.0306	0.0303	0.0074	0.0323	0.0349	0.0125	0.0038	0.0114	0.0181	0.0190	0.0320	0.0226	0.0014	0.0177	0.0108
Ni																	
Cu			0.0987				0.0447						0.0037			0.0471	
Zn				0.0156	0.0038									0.0040			
Br																	

Continues on the next page.

sample	6d	7a	7b	7c	7d	8a	8b	9a	9b	10a	10b	11a	11b	12a	12b	13a	13b
matrix	PES	PES	Cotton	Cotton +Lycra	PES	PES	Cotton	PES	Cotton	Cotton	PES	Cotton	PES	PES	Cotton	PES	Cotton
density	1.38	1.38	1.55	1.55	1.38	1.38	1.55	1.38	1.55	1.55	1.38	1.55	1.38	1.38	1.55	1.38	1.55
width [µm]	550	500	350	400	550	300	450	250	400	375	550	300	500	200	400	200	400
measurement	79	84	81	82	83	85	86	87	88	89	90	91	92	93	94	95	96
Si	1.69	0.226	0.678	0.269	0.0989	1.65	3.28	0.150	0.0447	0.0117	0.0160	0.148	0.149	0.0902	0.0851	0.113	0.0216
P	1.01	0.186	0.415	0.349	0.303	0.864	1.42	0.288	0.584	0.105	0.282	0.567	0.168	0.256	0.591	0.147	0.351
S	0.281	0.359	0.808	0.568	0.350	0.527	1.10	0.887	0.917	0.528	0.687	0.662	0.177	0.474	3.30	0.412	1.94
Cl	1.01	0.344	0.473	0.454	0.282	0.515	0.339	0.698	0.310	0.320	0.369	0.555	0.205	1.63	0.488	1.72	0.305
K	0.445	0.101	0.232	0.201	0.0799	0.158	0.179	0.233	0.108	0.110	0.0875	0.141	0.0337	0.0675	0.112	0.116	0.0763
Ca	0.905	0.151	0.907	0.650	0.0698	0.285	0.913	0.241	1.11	0.0874	0.0640	0.206	0.0380	0.306	1.67	0.116	0.777
Ti	0.0140	2.31	0.0063	0.0105	1.92	1.86	0.0092	0.0284	0.0067	0.917	1.32	1.84	0.940	0.427	0.0068	0.473	0.0079
Mn		0.0644			0.0574	0.0036								0.0316		0.0213	
Fe	0.0193	0.0146	0.0207	0.0251	0.0071	0.0078	0.0257	0.0485	0.0143	0.0114	0.0044	0.0333	0.0039	0.0228	0.0244	0.0234	0.0155
Ni				0.0022													0.0041
Cu	0.0122		0.0944	0.0105			0.249		0.301								
Zn	0.0204			0.0265				0.0275						0.0365		0.0351	
Br														1.07		1.34	

Table 11: PIXE measurements of textile fibres measured at the University of Surrey, ratio between the concentrations calculated with a ribbon target model vs. cylindrical target.

sample	1a	1b	1c	1d	2a	2b	2c	2d	3		4		5		6a	6b	6c
matrix	PES	Cotton +Lycra	Cotton	Cotton	PES	Cotton +Lycra	Cotton	Cotton	Cotton		Cotton		Cotton		PES	Cotton	Cotton +Lycra
density	1.38	1.55	1.55	1.55	1.38	1.55	1.55	1.55	1.55		1.55		1.55		1.38	1.55	1.55
width [µm]	550	450	300	300	550	350	300	300	350	350	300	300	300	300	400	350	300
measurement	56	57	59	60	61	62	63	64	65	66	67	68	69	70	71	72	73
Si	1.129	1.134	1.158	1.156	1.129	1.148	1.160	1.164	1.161	1.158	1.162	1.161			1.147	1.148	1.158
P									1.161	1.160	1.166	1.162	1.163	1.162	1.147	1.153	1.168
S		1.130	1.155	1.171	1.085	1.126	1.136	1.134	1.143	1.142	1.138	1.144	1.139	1.141	1.126	1.130	1.154
Cl	1.037	1.084	1.106	1.126	1.033	1.065	1.079	1.079	1.084	1.088	1.084	1.089	1.083	1.084	1.067	1.076	1.098
K		0.989	1.013	1.028	0.948	0.981	0.994	0.993	0.998	1.000	0.995	1.000	0.997	0.997	0.980	0.987	1.008
Ca	0.934	0.961	0.990	1.002	0.931	0.975	0.976	0.974	0.978	0.979	0.977	0.979	0.996	0.991	0.962	0.967	0.983
Ti	0.931	0.939	0.970	0.977	0.931	0.950	0.966	0.966	0.969	0.968	0.969	0.968	0.964	0.967	0.955	0.953	0.968
Mn															0.959		0.968
Fe		0.954	0.978	0.977	0.952	0.961	0.978	0.977	0.977	0.974	0.978	0.979	0.973	0.974	0.966	0.973	0.973
Ni																	
Cu			0.987				0.987						0.981			0.983	
Zn				0.987	0.977									0.985			
Br																	

Continues on the next page.

sample	6d	7a	7b	7c	7d	8a	8b	9a	9b	10a	10b	11a	11b	12a	12b	13a	13b
matrix	PES	PES	Cotton	Cotton +Lycra	PES	PES	Cotton	PES	Cotton	Cotton	PES	Cotton	PES	PES	Cotton	PES	Cotton
density	1.38	1.38	1.55	1.55	1.38	1.38	1.55	1.38	1.55	1.55	1.38	1.55	1.38	1.38	1.55	1.38	1.55
width [µm]	550	500	350	400	550	300	450	250	400	375	550	300	500	200	400	200	400
measurement	79	84	81	82	83	85	86	87	88	89	90	91	92	93	94	95	96
Si	1.127	1.136	1.147	1.140	1.129	1.170	1.131	1.190	1.140	1.136	1.127	1.165	1.137	1.211	1.139	1.209	1.137
P	1.136	1.127	1.153	1.133	1.118	1.187	1.145	1.195	1.134	1.140	1.119	1.162	1.120	1.213	1.134	1.215	1.136
S	1.115	1.101	1.132	1.112	1.094	1.179	1.136	1.164	1.113	1.112	1.092	1.147	1.099	1.185	1.115	1.184	1.109
Cl	1.069	1.049	1.087	1.061	1.041	1.132	1.108	1.120	1.069	1.060	1.042	1.099	1.041	1.140	1.104	1.139	1.082
K	0.976	0.962	0.991	0.971	0.953	1.033	1.000	1.036	0.973	0.973	0.954	1.007	0.957	1.065	1.000	1.064	0.982
Ca	0.950	0.944	0.970	0.953	0.934	1.007	0.968	1.008	0.957	0.956	0.936	0.986	0.941	1.034	0.977	1.027	0.960
Ti	0.933	0.939	0.956	0.946	0.932	0.984	0.941	0.986	0.942	0.949	0.930	0.974	0.940	1.002	0.948	1.002	0.945
Mn		0.939			0.936	0.976								0.988		0.986	
Fe	0.951	0.948	0.972	0.965	0.944	0.979	0.952	0.984	0.966	0.966	0.948	0.971	0.958	0.987	0.957	0.987	0.963
Ni				0.973													0.974
Cu	0.968		0.981	0.972			0.969		0.974								
Zn	0.976			0.981				0.986						0.984		0.983	
Br														0.982		0.985	

3.1.2 PIGE measurements of textile fibres

3 MeV protons are able to induce certain gamma-ray-producing reactions in material, which enables us to measure some light elements and even isotopes in the sample. A quantification of the PIGE values is difficult though a lower level of detection than with PIXE can be achieved, but nevertheless some limited accuracy of the results can be obtained. For example, elements and isotopes which can be measured are: ^{10}B, ^{11}B, Na, Si, Al, Mg and F. Oxygen can also be detected with a gamma detector, but the problem is that a high concentration of oxygen is present in the air and we always get an oxygen peak using an in-air beam.

In order to increase the solid angle, the gamma detector should be positioned as close to the target as possible. The advantage of the PIGE technique over the PIXE technique is a much stronger penetration of gamma-rays, so the absorption along the path towards the detector is negligible, which eliminates the influence of target geometry.

The results of the PIGE measurements done at the 2 MV HVEE Tandetron accelerator at the University of Surrey can be seen in the table below. The beam energy was 3021 keV, the exit window was an 8 µm Kapton foil, the angle of the detector to the beam directions was 90°, the beam current was around 1.2 nA, the measurement time was 10 minutes and the proton dose was around 0.7 µC. The dose was measured for each measurement with a chopper device (Figure 15).

The concentrations x_i of an element i were calculated using the formula:

$$x_i = x_{st} \frac{Y_i}{N_p} \frac{N_P^{st}}{Y_i^{st}} \frac{\langle S \rangle}{\langle S^{st} \rangle} \tag{48}$$

Where <S> is the average stopping power in the sample, N_p is the proton dose and Y_i is the gamma yield of the sample material. The concentration x_i was calculated with respect to the concentration of the same element in the standard. The superscript "st" denotes the respective quantities in the standard material. For qualitative as well as quantitative analysis the following peaks have been used:

	Energy (keV)	measured counts on the standard	statistical error of the measurement
10B	429	16065 (NIST 93a BS glass)	0.8%
11B	2125	939	3.3%
Na	440 1634 & 1636	19811 5015	0.7% 1.4%
Si	1273	338	5.4%
Al Al	844 1014	713 1071	3.8% 3.1%
O O	495 871 1982	97 35 31	10.2% 16.9% 18.0%
F F	1236 6129	144 (Teflon, 76 wt% F) 131	8.3% 8.7%

The PIGE measurements at the University of Surrey were done in two runs with different settings: for one we used a static beam of 300 µm FWHM. The beam profile was presumably Gaussian due to the scattering in the exit foil and the air. A Gaussian profile was also used in the calculations. In the second run we measured by scanning the beam over an area of 1x1 mm. In the evaluation of the latter measurements the beam was set to

a 1x1 mm homogeneous distribution with a square cross-section, so the beam was larger than the fibres. We took this fact into account by multiplying the result with the ratio of beam and fibre widths (d_b/d_f):

$$x_i = x_{st} \frac{Y_i}{N_p} \frac{N_P^{st}}{Y_i^{st}} \frac{\langle S \rangle}{\langle S^{st} \rangle} \frac{d_b}{d_f} \tag{49}$$

The proton dose was in both runs measured with a chopper in vacuum, but the ratio of the chopper signal to the dose was significantly different, so for both runs we determined two different calibration constants.

The results of the PIGE analysis are presented in the Table 13 and Table 14.

Evaluation of a the influence of distance on the PIGE measurements

The influence of the distance to the target was evaluated measuring the NIST 620 standard at two different locations, one at a distance of 11 mm from the exit window and the other at a distance of 20 mm from the exit window. The differences in gamma-ray yields are presented in Table 12.

Table 12: *Gamma yield of the NIST 620 glass at two different distances from the exit window*. Measurements were performed at the Jožef Stefan Institute.

element	Na	Mg	Al	Al	Si
energy	440 keV	1369 keV	844 keV	1014 keV	1273 keV
MIL77 - 11 mm	362891	1520	2433	3427	984
MIL78 - 20 mm	319802	1280	1824	1599	750
relative difference	-11.9 %	-15.8 %	-25.0%	-53.3%	-23.8 %

The gamma-ray production cross-section for silicon is quite strongly energy dependent. At energies from 3 MeV to 3.5 MeV the gamma-ray yield increases by an order or magnitude [169], unfortunately the information on Si the cross-section at energies below 3 MeV is not available; however according to our measurement the change is not so drastic.

Table 13: PIGE measurements of textile fibres, done at University of Surrey, first run. The concentrations are in mass%. The beam was static with a Gaussian profile and a FWHM of 300 µm. The concentrations are calculated using Eqn 48. The concentrations in bold print are standard values.

	measurement	345	346	344	343	341	347	348	339	338	332	331	340	349	350
	sample	NIST 93a	Teflon	9b	8b	13b	7c	6c	8a	12a	12b	12a	13a	2b	1b
	width [µm]			400	450	400	400	300	300	200	400	200	200	350	450
	chopper	**35.005**	3.582	67.733	81.148	67.100	64.116	60.409	68.574	68.310	64.629	68.412	67.400	57.199	57.113
Elem.	Energy [keV]														
10B	429	**3.9**		0.08	0.09										
11B	2125	**3.9**		0.07	0.06										
Na	440	**3.0**		0.02	0.20	0.04		0.09	0.04					0.02	0.03
Na	1634|1636	**3.0**		0.02	0.21	0.04		0.06	0.04					0.02	0.04
Si	1273	**37.8**		4.58	4.00		2.16		1.63						
Al	844	**1.21**						0.06		0.03		0.19			
Al	1014	**1.21**				0.02	0.02	0.10				0.08			
O	495	**53.8**		27.99	20.15	34.6		25.89	24.59	21.98	25.67	16.54			35.27
O	871	**53.8**			39.66	54.8		56.54	35.47	36.54	46.75	35.55	78.82	70.04	57.50
O	1982	**53.8**				29.8	25.44		26.35				31.09	27.22	36.35
F	1236		**76.0**				2.82	4.05			3.68	1.30		2.04	6.36
F	6129		**76.0**				1.25	1.40			6.88	1.15		0.66	5.02

Table 14: PIGE measurements of textile fibres, done at the University of Surrey, second run. The concentrations are in mass%. The beam was a homogeneous square of 1x1 mm. The concentrations are calculated using Eqn 49, where the width of a fibre was taken into account. The concentrations in bold print are standard values.

	measurement	99	1000	01	02	03	04	07	08	09	10	11	12	14	15
	sample	NIST 93a	1a	1c	1d	2a	2c	3a	4a	4b	5a	5b	2d	3a	6a
	d_f width [µm]	1000	550	300	300	550	300	350	300	300	300	300	300	350	400
	chopper	**37340**	666957	663720	665769	654848	688157	713227	681759	635034	648228	668480	671041	685081	731775
Elem.	Energy [keV]														
10B	429	**3.90**											0.0027	0.0001	0.02
11B	2125	**3.90**											2.01	1.51	1.19
Na	440	**2.95**						0.01	0.02		0.27	0.21	0.03		
Na	1634|1636	**2.95**	0.02	0.05	0.05	0.007	0.008	0.02	0.02	0.03	0.28	0.22		0.03	0.01
Si	1273	**37.8**			6.24	2.78	3.41	4.19	4.20	6.24	6.11	7.56	5.50	5.78	4.53
Al	844	**1.21**	0.19	0.39	0.26	0.04									
Al	1014	**1.21**	0.04	0.18	0.26	0.02	0.04	0.02	0.03	0.03	0.04	0.04	0.05	0.03	0.04
O	495	**53.8**													
O	871	**53.8**		70.4	69.6	35.8	52.7	42.3	51.1	54.0	50.4	42.7	54.3	50.6	40.2
O	1982	**53.8**	34.1	68.0	67.2	36.4	46.7								

3.1.3 The silicon anomaly

For silicon, significant differences in the concentrations were obtained using the two methods. With the PIXE method, Si from the surface layer of fibres is detected, due to the high absorption of soft Si X-rays (1.74 keV) in the material. But when the PIGE method is applied we make use of the gamma peak of 1273 keV energy, which is not affected by the absorption in the material. The concentrations measured with PIXE are in general lower than those measured with PIGE. The detection of Si with 3 MeV protons is hard, since the cross-section for production of gamma rays is very energy dependent, and the statistical error as a consequence of the stochastic nature of counting gamma rays is large in some cases, even close to 20%. Also, the level of detection is high (around 1%), so in some fibres silicon was not detected with the PIGE method, even though its presence was confirmed with the PIXE method.

Silicon is present in the oils used for the treatment of fibres during the fibre production. The result might indicate that silicon concentration is higher at the centre of the fibre than at the surface; however, the high PIGE limit for the detection of silicon calls for additional analysis, possibly with another more sensitive method.

Measurements of the 1273 keV peak in Si excited by the 3 MeV proton beam is somehow delicate since the cross-section for gamma-ray production varies strongly with the energy of the incoming proton beam. The energy of the projectiles varies slightly along the path travelled by protons through the air. The positioning of the sample is critical, however, the silicon peak at 1273 keV is often used for the normalization of the measurements in glass and ceramics [22, 170]. The strong absorption of the Si-K X-ray peak (1.74 keV) in comparison to the gamma Si peak was used to determine the thickness of a thin SnO_2 layer on the surface of Art Nouveau glass [171], but the energy of the proton beam was 3.85 MeV; at this energy the cross-section for the production of the silicon gamma rays (1273 and 1779 keV) is not notably energy dependent.

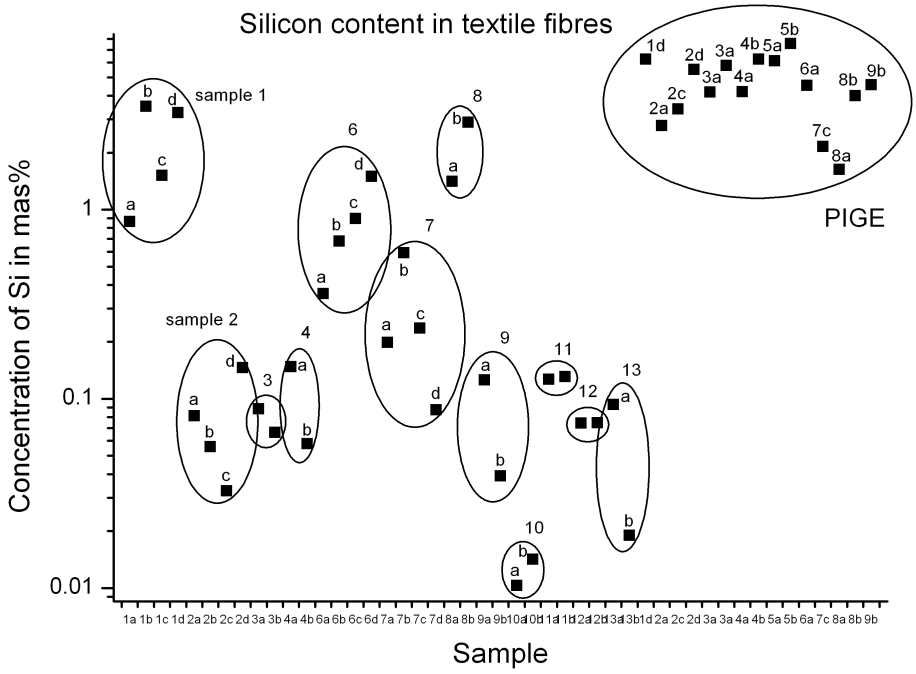

Figure 34: *The concentration of silicon in fibres*. The concentrations of Si measured with the PIGE method is higher than the values obtained by the PIXE method.

3.1.4 White PES fibres

All white polyester fibres (PES) contain around 1 mass% of Ti. This is probably due to TiO_2, which gives a white colour to the transparent polymer material. A low level of Ti was observed in fibres 6d and 9a. Fibre 6d exhibited the highest level of Ca and K among similar fibres, as well as the presence of Cu, Zn and Fe as trace elements. This might indicate that the main pigment was not TiO_2, but $CaCO_3$. The other sample with a low Ti content, fibre 9a, also exhibits a high content of Fe and Zn trace elements, which may indicate contamination, but we did not repeat the measurement at some other spot. The results of the analysis are shown in Figure 35.

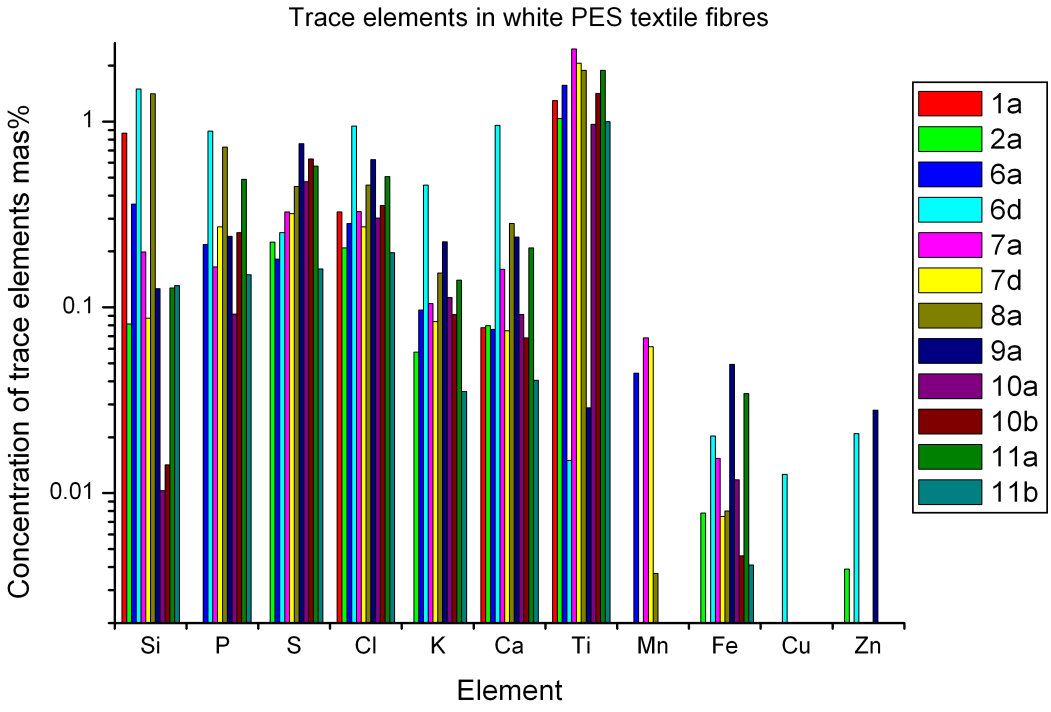

Figure 35: The trace elements in 12 different white PES textile fibres.

3.1.5 Teflon-treated fibres

The treatment of fibres with Teflon left a measurable fluorine signature, which was only detected by the PIGE. In the black PES the presence of Ti, Mn, Zn and Br was observed, most probably due to the use of a different black pigment than in the cotton fibres, where higher amounts of calcium and sulphur were measured, as well as a lower concentration of chlorine. However, the only measured element that is characteristic for Teflon dressing remains fluorine.

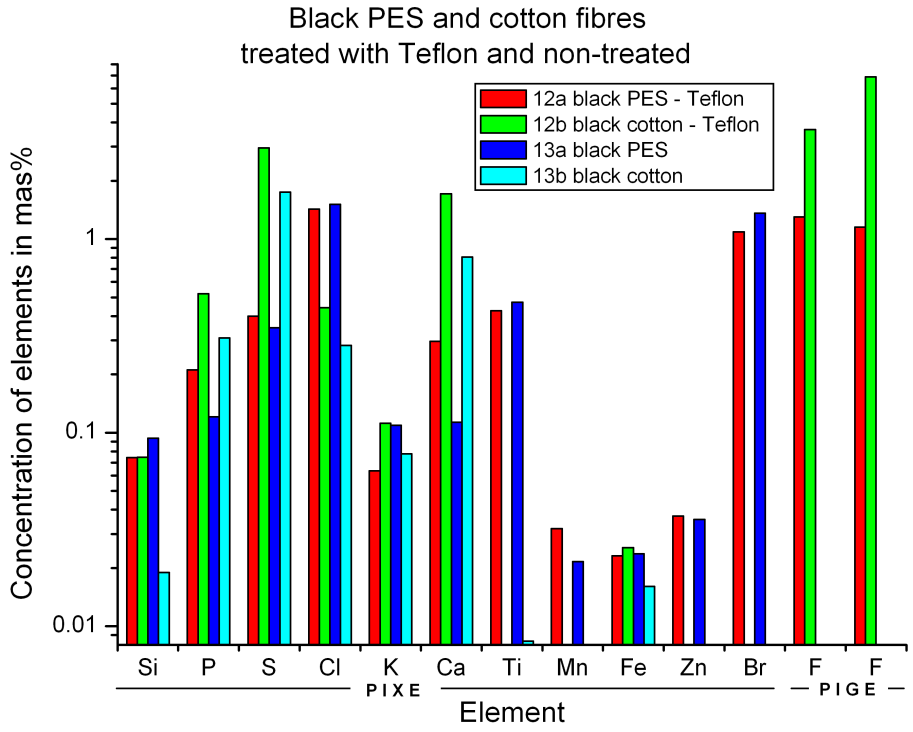

Figure 36: The trace elements of black PES and cotton textile fibres, plain and treated with Teflon.

3.1.6 Nano-silver-treated fibres

Silver was not detected in the sample. The reason might be that the amount of silver was below the limit of detection, which was around 10 ppm.

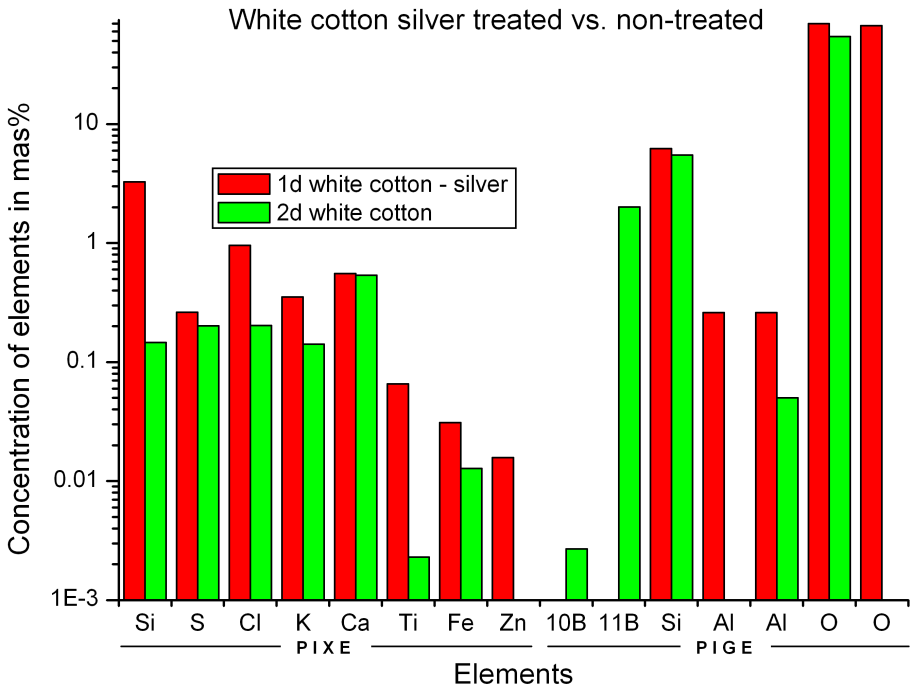

Figure 37: The trace elements in white cotton textile fibres, plain and treated with silver.

3.1.7 Microbeam mapping of textile fibres

The textile fibres have been measured at MIC in Ljubljana. The maps were obtained using two X-ray detectors for PIXE and one particle detector for off-axis STIM measurement. The Si(Li) detector was positioned at the right and HP-Ge detector was positioned at the left side from the beam direction. The direction of a fibre was either horizontal or vertical which means either perpendicular to the plane defined by the beam and detector direction or laying in the plane and perpendicular to the beam. The geometrical effect is much more pronounced with vertical positioning for which we also calculated the mathematical model.

Microbeam elemental maps of a white cotton fibre were recorded at MIC in Ljubljana (Figure 39). The maps were recorded with OMDAQ data acquisition system [172]. The energy of a proton beam was 3 MeV, and the beam diameter was below 1.5 μm. The size of maps is 400x400 μm. The geometrical effect can be observed in light elements maps. A part of the fibre, which is closest to the detector, has the strongest signal, due to the lower absorption of characteristic X-rays. This effect is most noticeable with light elements (Si and Al), where absorption in the material is strong. With increasing energy of characteristic Kα peaks (heavier elements) the geometrical effect diminishes. A STIM (scanning transmission ion microscopy) map shows us the silhouette of the fibre, from which we can determine the fibre width: 200±15 μm. There are two maps of chlorine, recorded with two different X-ray detectors, positioned left and right from the beam. Stronger signal is detected at the side of the fibre, which is closer to the detector, however the same effect is not noticeable with the titanium maps due to higher energy of characteristic Kα peaks (4.51 keV for Ti vs. 2.62 keV for Cl). Elemental distribution is mostly homogeneous, some hairiness can be observed. The PIXE spectrum from Si(Li) and HPGe detectors is seen in Figure 38.

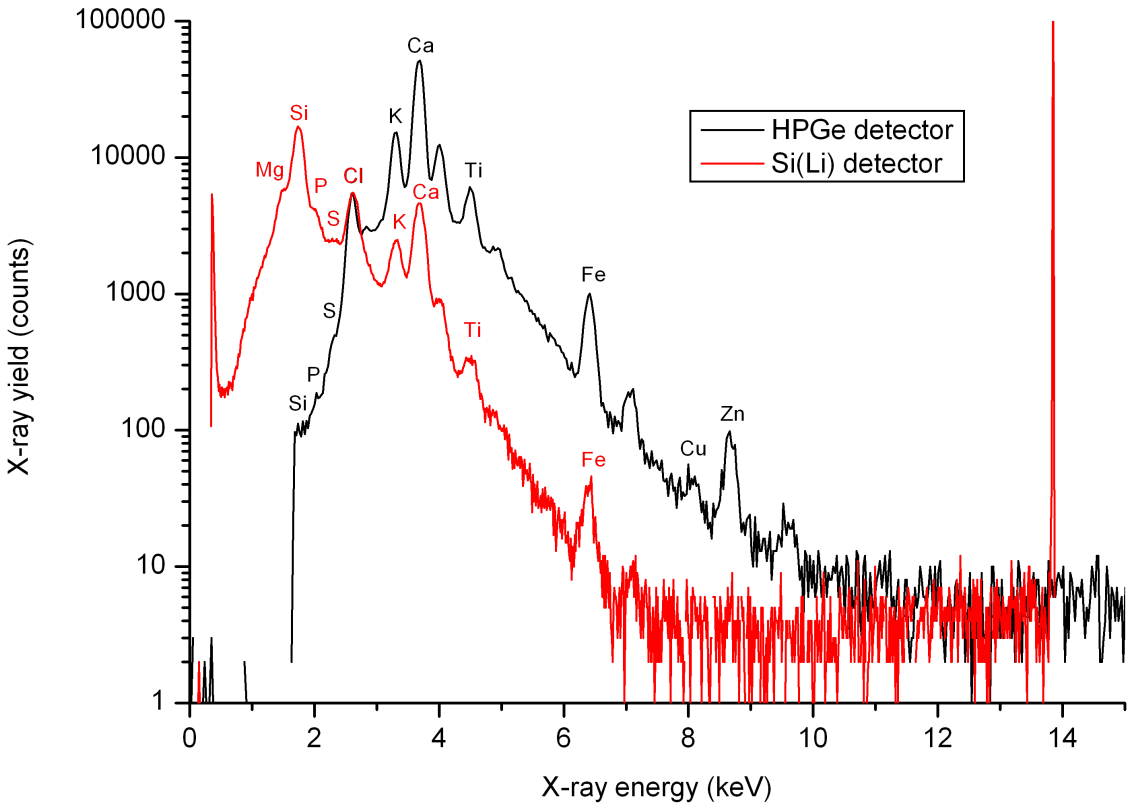

Figure 38: PIXE spectrum from Si(Li) (a) and HPGe (b) detectors. The beam energy was 3.021 MeV, the proton dose was 1.36 µC, the time of measurement was 92.1 min, the resulting average ion-beam current was 0.25 nA. The Si(Li) detector had a 8 µm Be window, 10 nm gold layer and 0.75 µm Si dead layer without additional filters and the HPGe detector had a 25.4 µm thick Be window with 20 nm gold layer and 1.1 µm Ge dead layer with 100 µm Kapton filter. The target to crystal distance of Si(Li) detector was 3.5 cm at a 45° angle and for HPGe detector the distance was 3.1 cm at a 45° angle. Elements Cu and Zn were detected only with the HPGe detector.

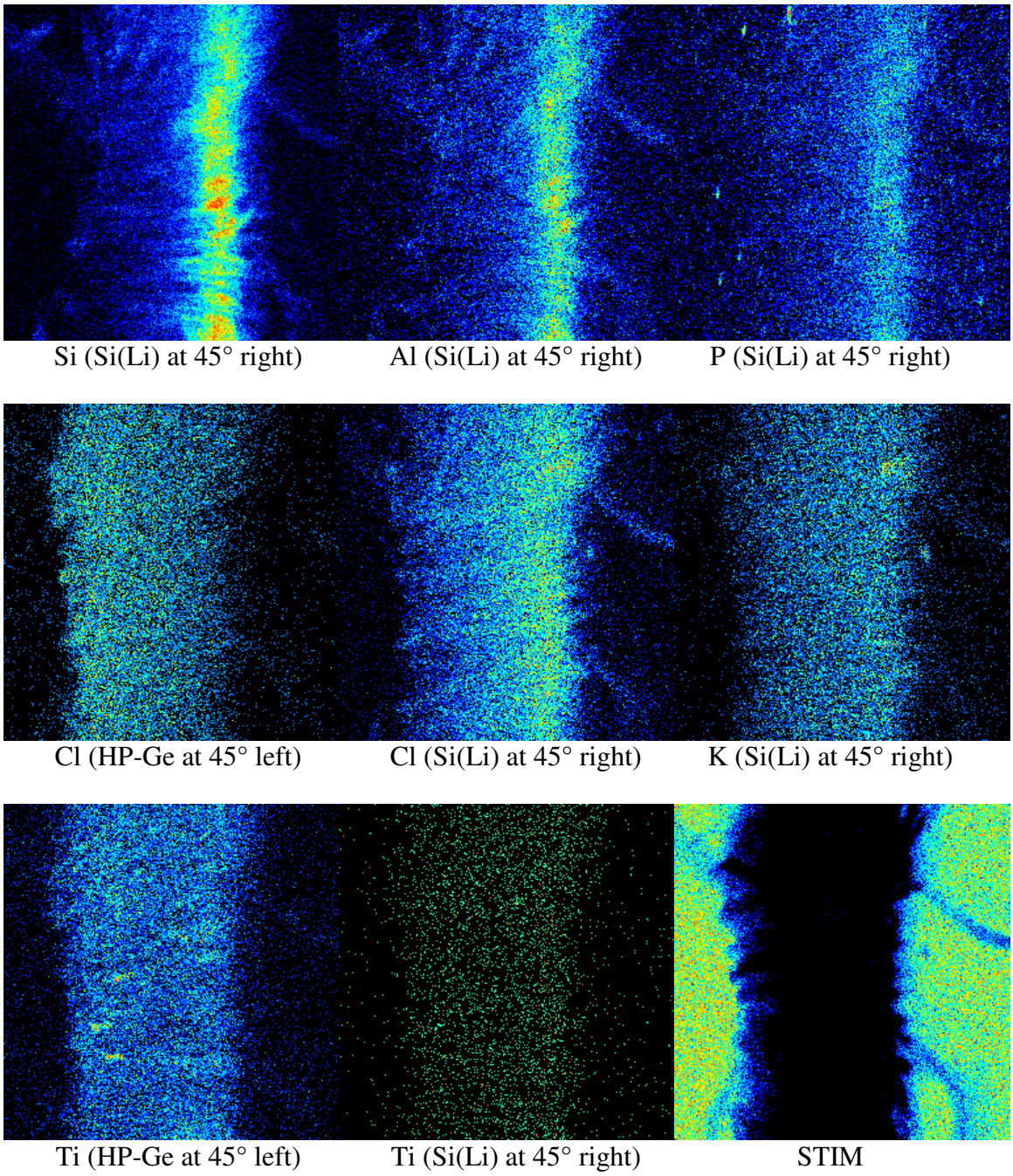

Figure 39: Elemental maps of a white cotton fibre recorded in a vertical position, perpendicular to the beam and the detector direction. Maps were recorded at MIC, Ljubljana. 3 MeV proton microbeam with a diameter below 1.5 µm was used for the measurement. Dimension of a map is 400x400 µm. The geometrical effect can be observed in light elements maps. A part of the fibre, which is closest to the detector, has the strongest signal, due to the lower absorption of characteristic X-rays. This effect is most noticeable with light elements (Si and Al), where absorption in the material is strong. With increasing energy of characteristic Kα peaks (heavier elements) the geometrical effect diminishes. A STIM (scanning transmission ion microscopy) map shows us the silhouette of the fibre, from which we can determine the fibre width: 200±15 µm. There are two maps of chlorine, recorded with two different X-ray detectors, positioned left and right from the beam. Stronger signal is detected at the side of the fibre, which is closer to the detector, however the same effect is not noticeable with the titanium maps due to higher energy of characteristic Kα peaks (4.51 keV for Ti vs. 2.62 keV for Cl). Elemental distribution is mostly homogeneous, some hairiness, typical for natural plant fibres can be observed.

Another example of fibres is a simultaneous measurement of three fibres in a map 2x2 mm. The beam used was the same, but the positioning was horizontal. The fibres are white cotton fibres where the lower two were treated with antibacterial nano-particles of silver, however silver concentration is below the detection limit. Duration of the measurement was 244 minutes at an average beam current of 0.48 nA. Geometrical effect is seen in the maps of P, Cl an K as a pattern typical of two threads spun around each other; two diagonal dark lines, crossing the top two fibres. The third fibre is in the observed part more hairy than the other two, so the pattern is less pronounced. Huge difference in concentration between untreated fibre and the other two treated fibres is observed in a potassium map. Less pronounced, but still noticeable difference is in a chlorine and titanium map. Hairiness, typical for cotton and other natural plant fibres can be best observed in STIM and silicon map. Width of fibres obtained from the STIM map is 270±50 µm. The maps are constructed from X-ray yields, thus not representing the absolute concentrations of the elements.
PIXE spectrum from Si(Li) and HPGe detectors is seen in Figure 40.

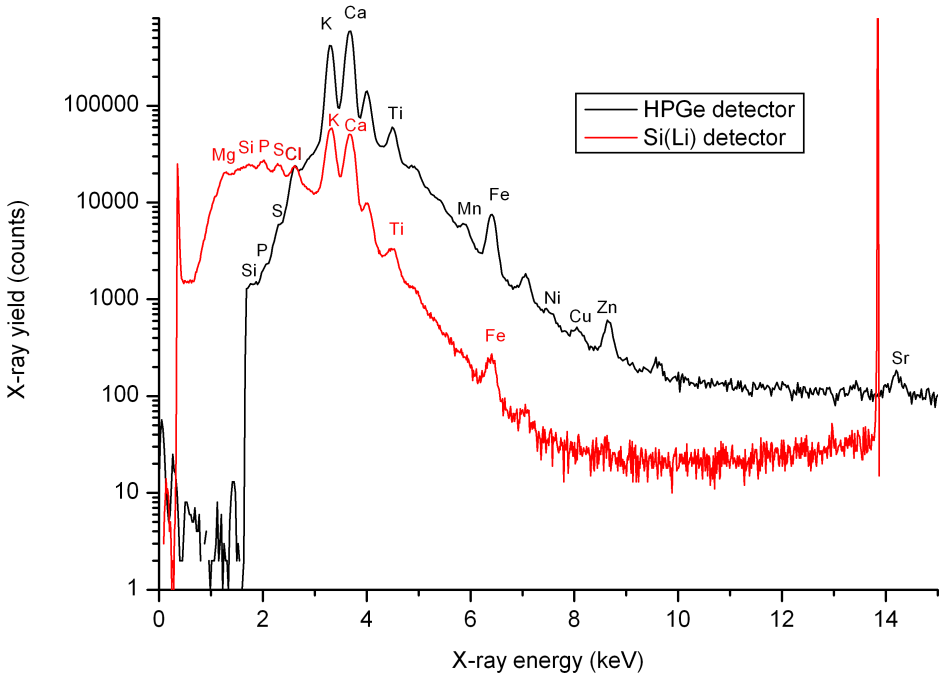

Figure 40: PIXE spectrum from Si(Li) (a) and HPGe (b) detectors. The beam energy was 3.021 MeV, the proton dose was 7.02 µC the time of the measurement was 244 min, the resulting average ion-beam current was 0.48 nA. The Si(Li) detector had a 8 µm Be window, 10 nm gold layer and 0.75 µm Si dead layer without additional filters and the HPGe detector had a 25.4 µm thick Be window with 20 nm gold layer and 1.1 µm Ge dead layer with 100 µm Kapton filter. The target to crystal distance of Si(Li) detector was 3.5 cm at a 45° angle and for HPGe detector the distance was 3.1 cm at a 45° angle. Kα peaks of detected elements are marked: Mg, Si, P, S, Cl, K, Ca, Ti, and Fe. The elements Mn, Ni, Cu, Zn and Sr were detected only with HPGe detector.

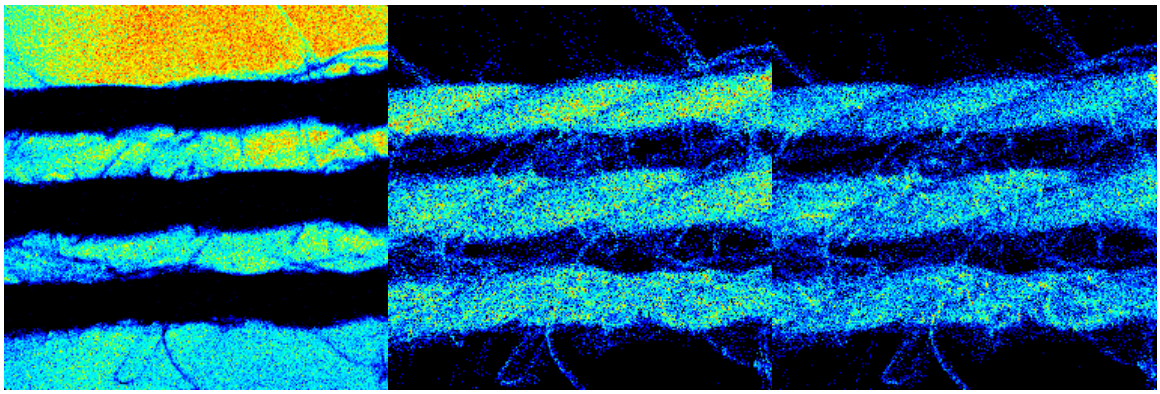

STIM Si (Si(Li) at 45° right) P (Si(Li) at 45° right)

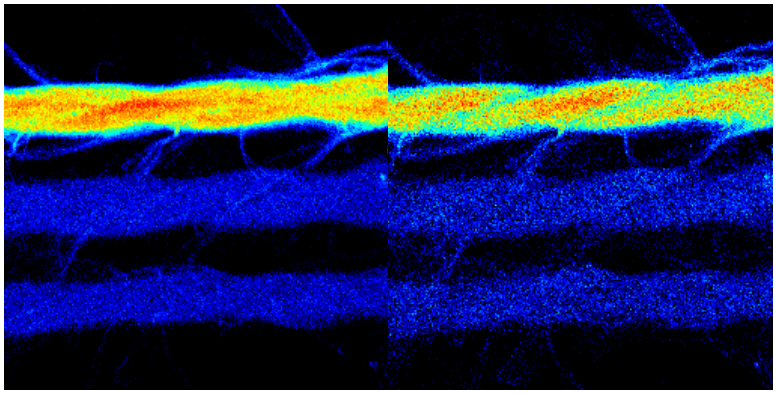

K (HP-Ge at 45° left) K (Si(Li) at 45° right)

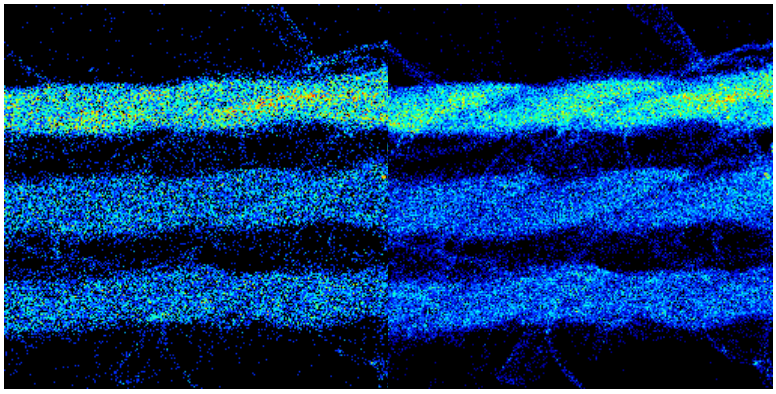

Cl (HP-Ge at 45° left) Cl (Si(Li) at 45° right)

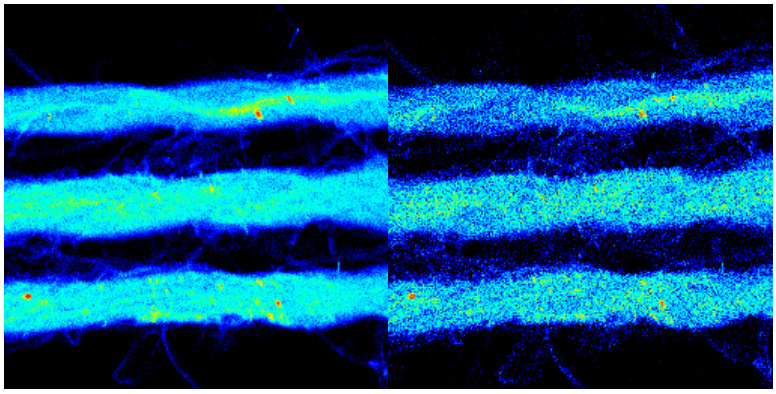

Ca (HP-Ge at 45° left) Ca (Si(Li) at 45° right)

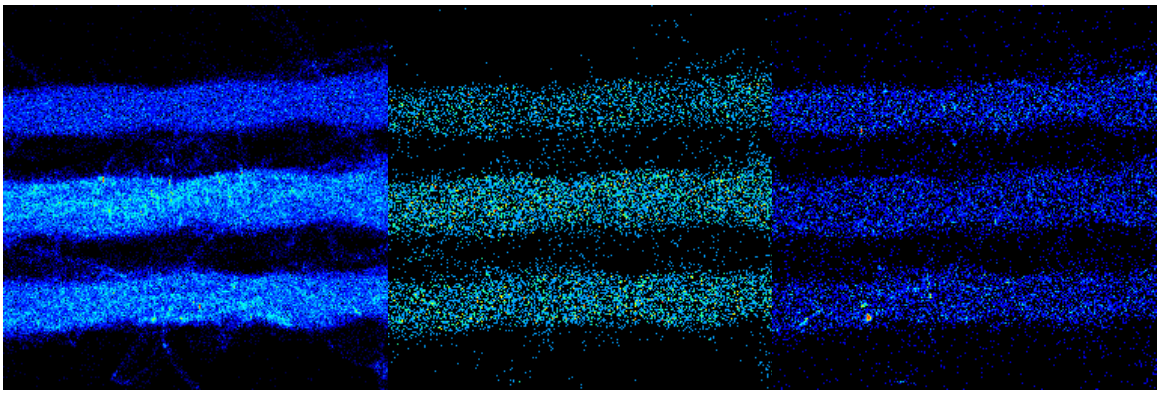

Ti (HP-Ge at 45° left) Ti (Si(Li) at 45° right) Fe (HP-Ge at 45° left)

Figure 41: Elemental maps of three white cotton fibres, recorded in a horizontal position, perpendicular to the beam, but in the same plane as the detector axis. Maps were recorded at MIC, Ljubljana. 3 MeV proton microbeam with a diameter below 1.5 µm was used for the measurement. Dimensions of the map are 2x2 mm. Geometrical effect is seen in the maps of P, Cl an K as a pattern typical of two threads spun around each other; two diagonal dark lines, crossing the top two fibres. The third fibre is in the observed part more hairy than the other two, so the pattern is less pronounced. Huge difference in concentration between untreated fibre and the other two, treated fibres is observed in a potassium map. Less pronounced, but still a noticeable difference is in a chlorine and titanium map. Hairiness, typical for cotton and other natural plant fibres can be best observed in STIM and silicon map. Fibres are mostly homogeneous, with some particles (<20 µm) containing high amount of calcium or iron. Average width of the fibres obtained from the STIM map is 270±50 µm.

3.2 RBS measurements

The RBS technique is an ion-beam analytical technique complementary to PIXE and PIGE. The information gathered from it is mainly focused on the depth distribution of the elements, which is impossible to measure with the conventional PIXE/PIGE technique. The samples where most information can be obtained from the RBS technique are plated targets, where the surface layer is sufficiently thin for protons to penetrate it twice, first on the way into the material and then on their way out of the material to the detector. Besides plated samples, we can also measure some light elements, which due to resonant nuclear reactions express a response up to few hundred times higher than expected for elastic scattering in a Coulomb field.

3.2.1 Nuclear scattering cross-sections

Nuclear scattering cross-sections are very different from Rutherford cross-sections, which may be erroneously expected when observing the back-scattered projectiles. The differences to the Rutherford value are higher for light target elements. With protons as projectiles, the non-Rutherford cross-sections are especially important. The known nuclear scattering cross-sections, calculated for a scattering angle of 151° with the SigmaCalc [15] program based on IBANDL [12] database, are displayed in the following figures. The cross-sections are displayed relative to the Rutherford elastic cross-section.

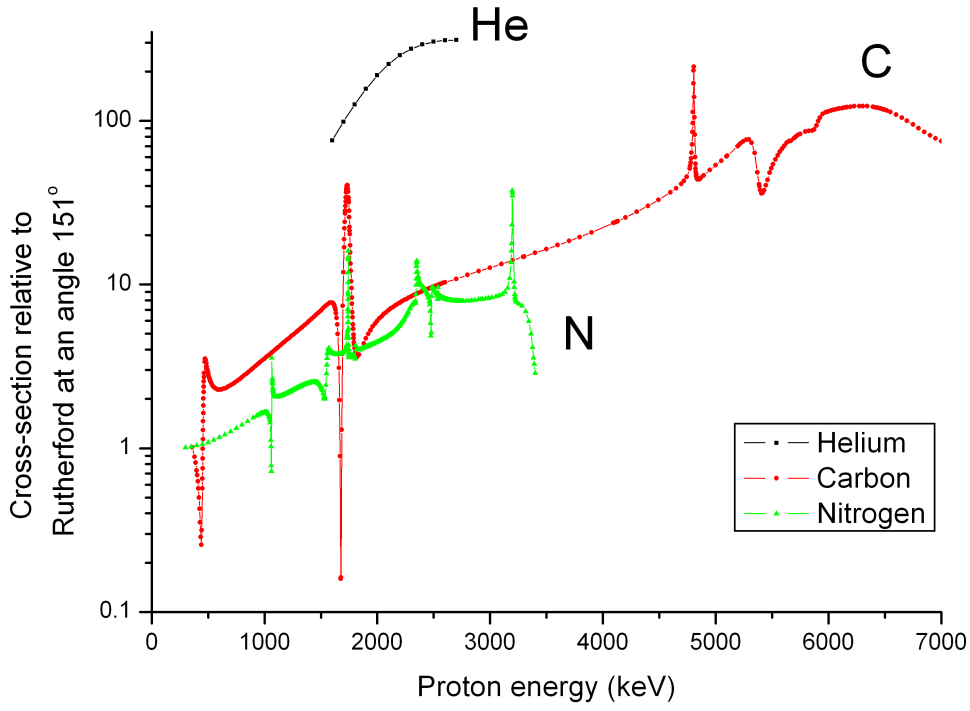

Figure 42: Non-Rutherford nuclear scattering cross-section for protons on helium, carbon and nitrogen. The vertical axis is in a logarithmic scale. [15]

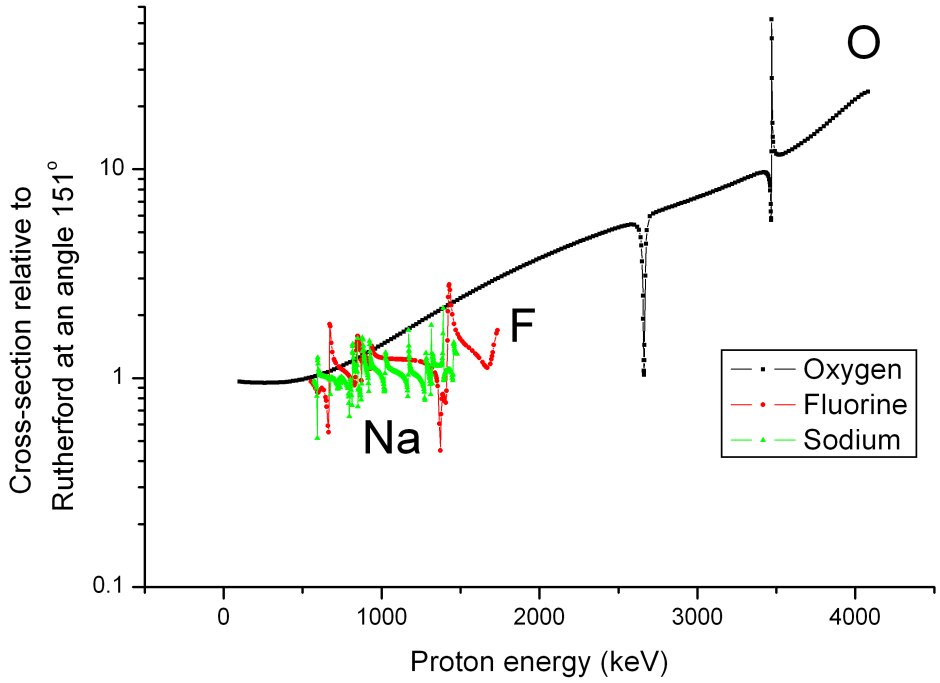

Figure 43: Non-Rutherford nuclear scattering cross-section for protons on oxygen, fluorine and sodium. The vertical axis is in a logarithmic scale. [15]

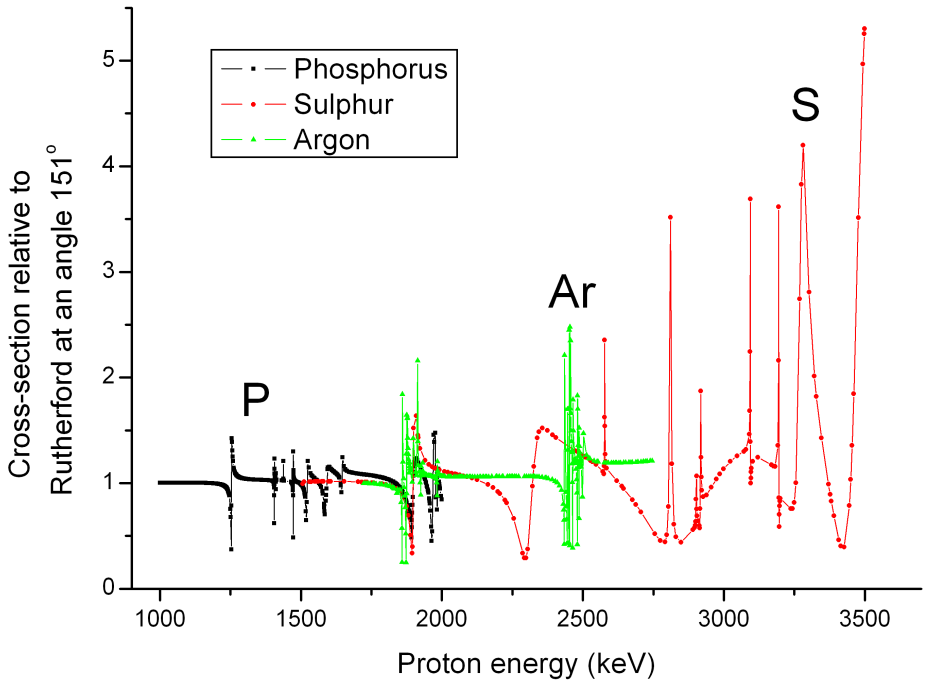

Figure 44: Non-Rutherford nuclear scattering cross-section for protons on phosphorus, sulphur and argon. The vertical axis has a linear scale. [15]

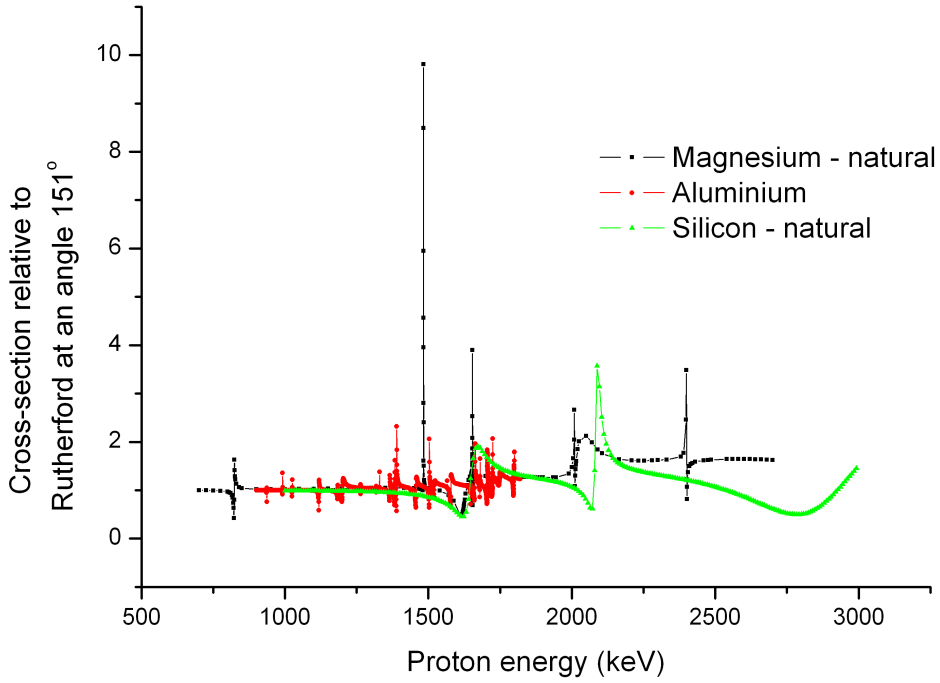

Figure 45: Non-Rutherford nuclear scattering cross-section for protons on natural magnesium, aluminium and natural silicon. The vertical axis has a linear scale. [15]

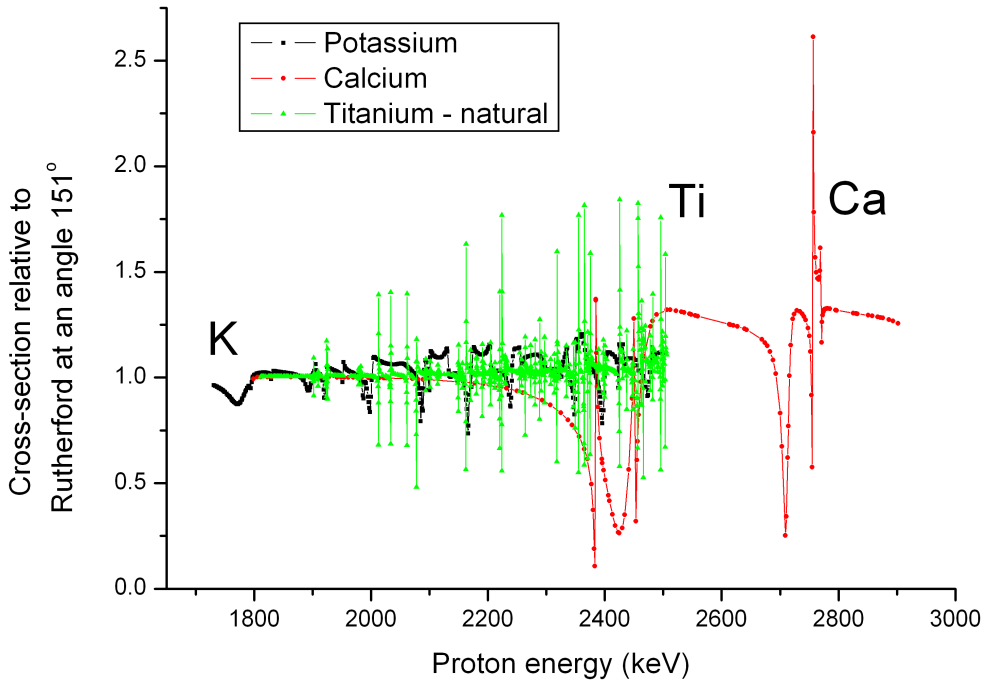

Figure 46: Non-Rutherford nuclear scattering cross-section for protons on potassium, calcium and natural titanium. The vertical axis has a linear scale. [15]

3.2.2 Calibration of the RBS system

An RBS spectrum depends on various parameters. Some of them can be determined from the measured geometrical quantities and some by using the SRIM database for proton stopping in materials. The others have to be determined by fitting a simulated spectrum to the measured data in a process of calibration. Each parameter and its uncertainty will be described later on.

3.2.2.1 Beam Energy

The beam energy in vacuum is set by the voltage at the terminal of the accelerator and by the initial voltage at the ion source. The beam energy in a vacuum was checked by NRA measurements [173]. The corrections based on this work were taken into account when calculating the beam energy in a vacuum. The beam energy used in a simulation program like SIMNRA is the energy of the beam with which the projectiles hit the first layer of the measured material. In our case this is the energy of projectiles in a vacuum, decreased by the energy lost in the exit window and in the atmosphere between the exit window and the target. Additionally, energy scattering of the beam occurs. The thickness of the Al exit window was confirmed to be 8.0 μm, with a good fit to one of the first measured spectra shown in Figure 47.

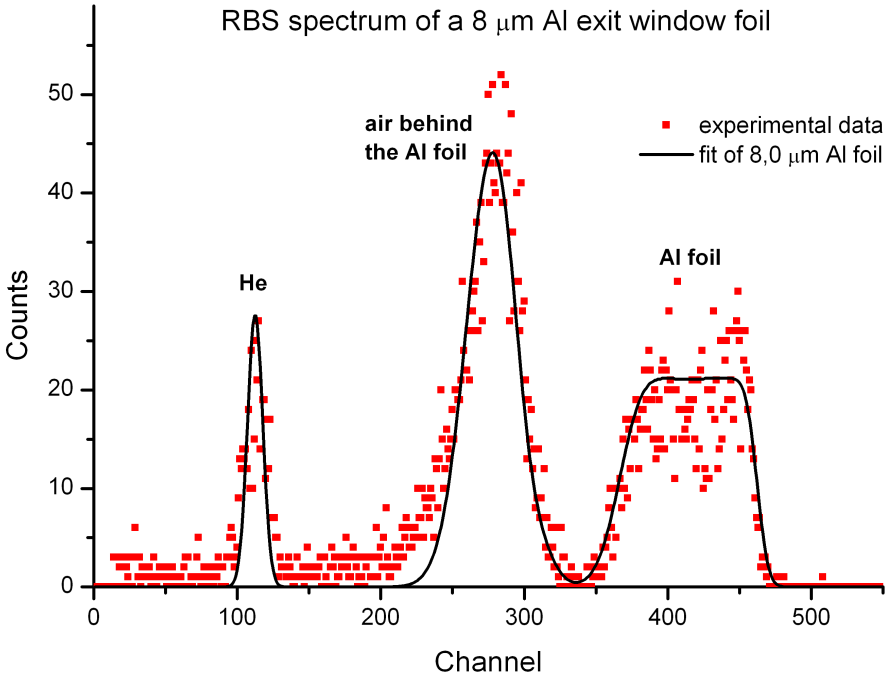

Figure 47: *RBS spectrum of an 8 μm Al exit window*. The width of the Al foil "peak" depends on the actual width of the Al foil. A He resonance peak and a peak due to scattering in air behind the Al foil is also denoted.

An important variable that is not very well determined is the composition of the atmosphere in the space between the exit window and the target. Since we are using He gas to reduce the stopping of backscattered protons along their path to the detector, some He is spilled in front of the target, mixing with the air and reducing the stopping of the

beam. Taking into account the correction of the beam energy and all the uncertainties in the target position and composition of the atmosphere, the beam energy was set to 2880 keV with an estimated error of 50 keV. The energy spread of the incident beam was set to 65 keV.

3.2.2.2 The scattering angle

The scattering angle is the angle between the beam and the detector directions. It is set by the detector holder which is fixed to the exit nozzle. The only parameter determining the scattering angle is the inclination holder. The angle is 29°±0.2°, which translates to a scattering angle of 151°. All the cross-sections which vary significantly from the Rutherford cross-sections were extracted for an angle of 151° from the SigmaCalc [15] tool based on the IBANDL [12] database in an R33 format used by the SIMNRA. Non-Rutherford cross-sections for He, B, C, N, O, Na, Al, Si, S, all calculated for a scattering angle 151°, were used.

3.2.2.3 The foil in SIMNRA

The term "foil" in SIMNRA denotes the material between the target and the detector. This distance was filled with He gas, to reduce the stopping of the projectiles. With our early experiments also a 1.5 μm Al foil was used to reduce the light that could influence the measurement with an additional noise at low-energy channels. Since the RBS nozzle was made of Al, which is not transparent to light, the thin foil was removed. In the case of using a transparent (*e.g.* white plastic) nozzle, the light protection foil should be mounted back. The distances were carefully measured and the thickness of the He layer was set accordingly to 207011e15 at/cm^2. The foil thickness depends very much on the flow. If the He flux is interrupted, the air rushes into the RBS nozzle and increases the stopping of the projectiles, which would result in a spectrum moved towards lower energies. The same effect on the spectrum would be achieved by lowering the beam energy, or increasing the layer of air or He in front of the target, which corresponds to increasing the distance from the exit nozzle to target.

3.2.2.4 Energy calibration with a set of thick targets

When all the other parameters described in the previous sub-chapters were set we can perform a calibration of the RBS system with a set of thick targets. The remaining two parameters that we can adjust are the energy and the dose calibration.

The energy calibration is made by setting the energy/channel parameter in the SIMNRA program. The edge of the simulated spectrum of a mono-elemental thick target should agree with the edge of the experimental data. The energy/channel parameter is set accordingly, and should not change when the sample is changed, hence exact positioning is of utmost importance. An energy calibration with a set of thick targets makes sense only if we have a reproducible positioning, with an error margin below 0.2 mm. With a higher positioning uncertainty we cannot say if the misfit in the energy axis is the consequence of the positioning error or of the thin layer of light (low Z) element on the top of a heavier (high Z) substrate.

The high-energy edge of the simulated spectrum and the spectrum measured on a mono-elemental thick target without a surface layer, should agree perfectly, otherwise the parameters have changed between the measurements. If a disagreement is observed, the parameters which were modified should be identified. The calibration should then be

repeated with the identified parameters kept constant.

3.2.2.5 Dose calibration with a set of thick targets

The dose calibration was done with the program SIMNRA [102], which we also used for an interpretation of the measured spectra. The number of protons which hit the target is proportional to the counts in the spectrum and has to be set for each measurement correctly. The proton dose has to be measured independently in order to properly calibrate the system. The dose calibration is a process in which we determine the number of particles hitting the target and flying back in the detector solid angle. In the program SIMNRA the parameter we are looking for is denoted as "particles*sr". To properly determine this parameter, the proton dose is measured and multiplied by a calibration factor. The calibration factor is determined by fitting the parameter "particles*sr" on the mono-elemental thick target and correcting it for the dead time. The mean calibration factor is the average of the calibration factors for different mono-elemental thick targets and is used further for measuring all the unknown samples. The "particle*sr" parameter is calculated according to Eqn 50.

$$particle*sr = dose \cdot mean\_calibration\_factor \cdot (1+DT) \qquad (50)$$

The uncertainty of the calibration factor indicates the accuracy of the measurement. The results of the thick target measurement for the dose calibration is shown in Table 15.

Table 15: *Calculation of the dose calibration factor.* Dead time was up to 30.6% for tantalum.

Element	dose [µC]	DT [%]	fitted particles*sr [1e10]	calibration factor [1e10/µC]
Ta	0.1	27.0%	1.08	13.72
Cu	0.1	7.5%	1.25	13.45
Al	0.1	3.0%	1.25	12.88
Al	0.1	3.4%	1.25	12.93
Ta	0.3	30.6%	2.4	10.45
Cu	0.3	8.3%	3.36	12.13
S	0.3	3.5%	3.36	11.59
			average	**12.45**
			st. dev.	**1.14**
			rel. error	**9.2%**

To calculate the dose calibration factor, the projectile dose has to be measured by a chopper or a wire-mesh charge-collecting device, and also the influence of the dead time (DT) is taken into account. The calibration factor is a fitted parameter "particles*sr" in the SIMNRA program. The results for thick target measurements are divided by the dose and multiplied by the dead-time correction factor. The average calibration factor for a given set of measurements is 12.45 ± 1.14 1e10/µC, which shows a 9.2% standard deviation (Table 15).

A much more precise calibration was obtained using a low count-rate, with a dead time of up to 2%, Table 16. Each count of a dose measurement represents a collected charge of 1 nC, which is roughly proportional to 1 nC on the target (the transmission of the wire mesh is 58%).

Table 16: *Calculation of the dose calibration factor, using careful calibration, measurements at a low count-rate.* The proton dose is determined with the wire-mesh charge integration, where each count is 1 nC.

Element	dose [cnt]	DT [%]	fitted particles*sr [1e10]	calibration factor [1e10/cnt]
Rh	1013	2%	1.10	0.001086
Cu	1005	0.95%	1.05	0.001045
Si	1012	0.50%	1.10	0.001087
C	1010	1%	1.05	0.001040
Al	1004	0.25%	1.10	0.001096
			average	**0.001071**
			st. dev.	**2.62E-05**
			rel. error	**2.45%**

A much better uncertainty of the calibration factor was achieved with a measurement at low count-rates. This might be a consequence of an improper correction for the dead time as well as a lower precision of the positioning.

3.2.3 The samples for RBS measurements

First some samples with a known structure were measured to check the system. We measured plated targets, some targets we expected to be plated, and also some multi-elemental targets, which turned out not to be plated, or the plating was too thick for the 3 MeV protons to penetrate it.

Samples of copper, plated with tin and alternatively with a tin-lead alloy were produced to test the method further. The actual structure (thickness) of the samples was observed in the electron microscope and tested using the SEM-EDS elemental analysis technique. The effect of the roughness was observed.

Samples of thin hard layers on substrates of silicon and glass were measured and the thicknesses were determined.

Another set of measurements was made on archaeological samples. One was a presumably tinned Roman brooch, and another was a gilded bronze fragment of a cross with a motive of Mary's annunciation. The effect of roughness as well as the porosity of the archaeological samples was observed. Two medals of bravery from the 2nd World War were also measured. Both had the same motive of a partisan with a rifle on the face side and were produced for Yugoslav partisans. But one was produced in Russia during 1944-1945 and the other one in Yugoslavia in later years. The thickness and roughness of the gold layer on both medals were determined.

3.2.4 Results of BS measurements of representative samples

A tantalum foil with a declared 2 µm thickness was measured with a 3 MeV proton beam. The RBS detector was positioned at a scattering angle of 135°. The graph shows good agreement between the simulated spectrum of a 2 µm thick Ta layer and the experimental data. However the incident angle might deviate from the usual 0° due to a loose sample surface.

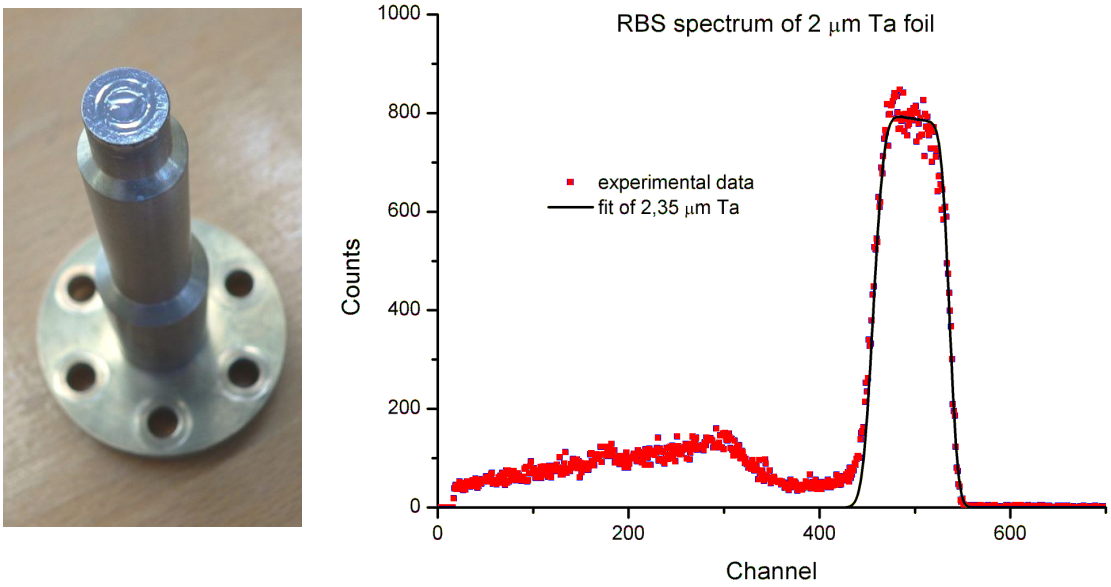

Figure 48: *RBS spectrum of a 2 μm Ta foil.* The structure left of the Ta signal corresponds to air behind the foil. The fitted thickness is 2.35 μm (13000e15 at/cm^2).

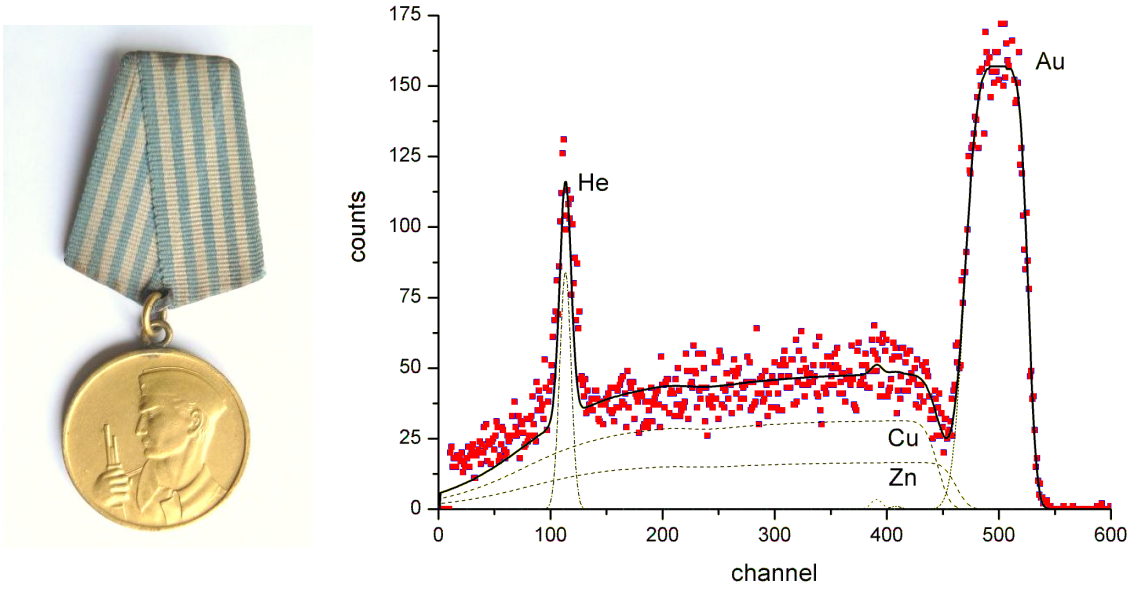

Figure 49: *Medal of bravery produced for Yugoslav partisans in Russia in 1944-45.* The fitted thickness of the Au layer is 1.6 μm (9700e15 at/cm^2). [8]

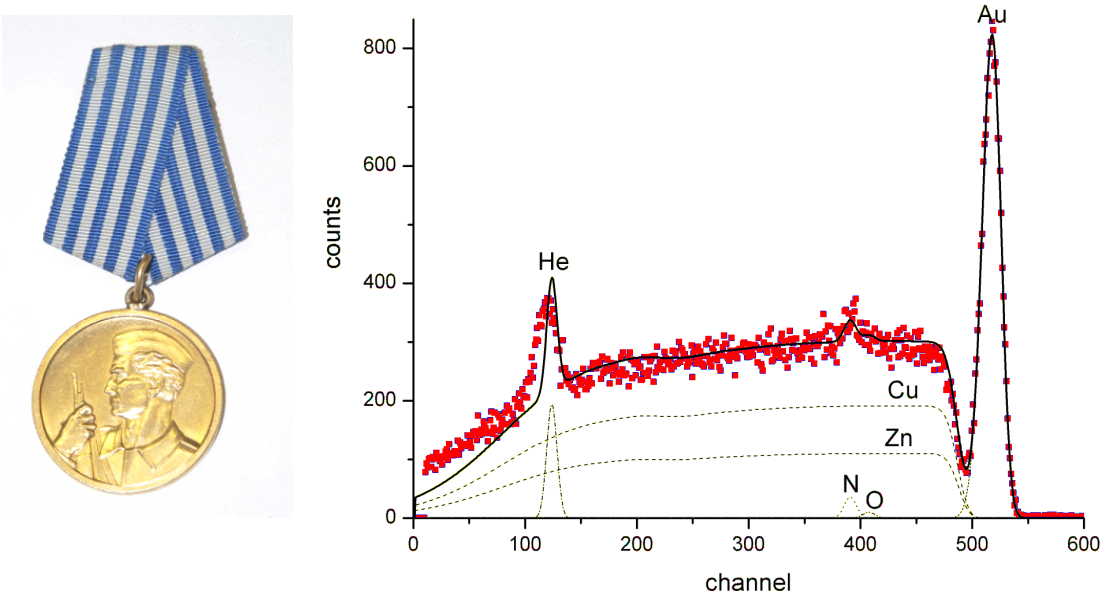

Figure 50: Y*ugoslav medal of bravery produced in Yugoslavia after 1945.* The fitted thickness of the Au layer is 0.4 µm (2400e15 at/cm^2). [8]

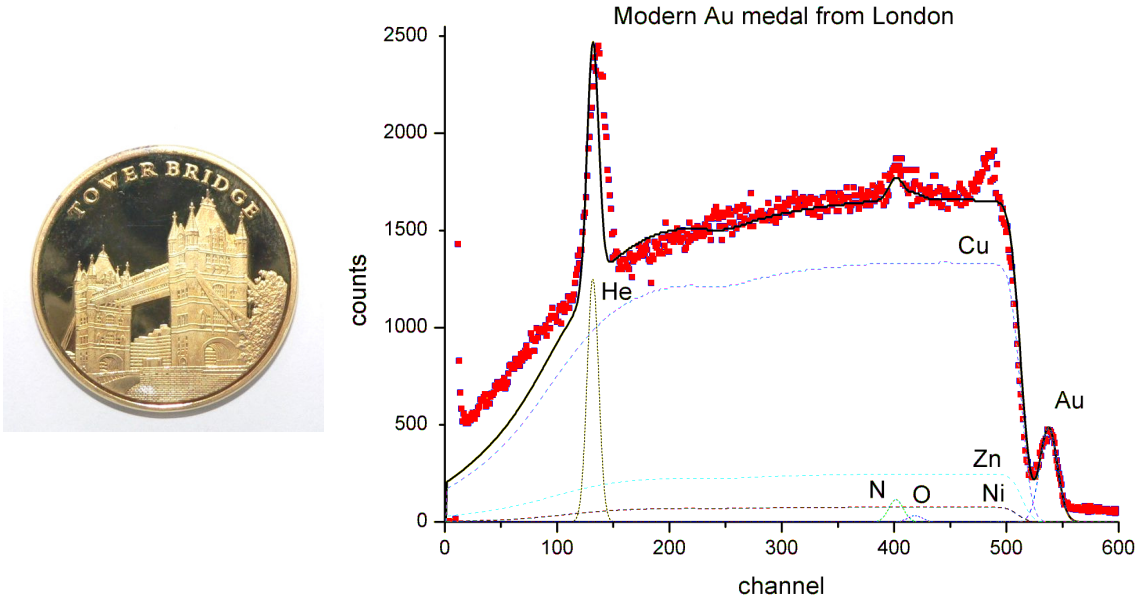

Figure 51: *Modern Au plated commemorative medal from London.* The thickness of the Au layer is 42 nm (250e15 at/cm^2). The substrate is brass (alloy of Cu, Zn and Ni). The energy of the peak on the top of the slope corresponds very well to a 2000e15 at/cm^2 Cl in the layer between the Au and the substrate, but such a constitution is improbable and thus not fitted.

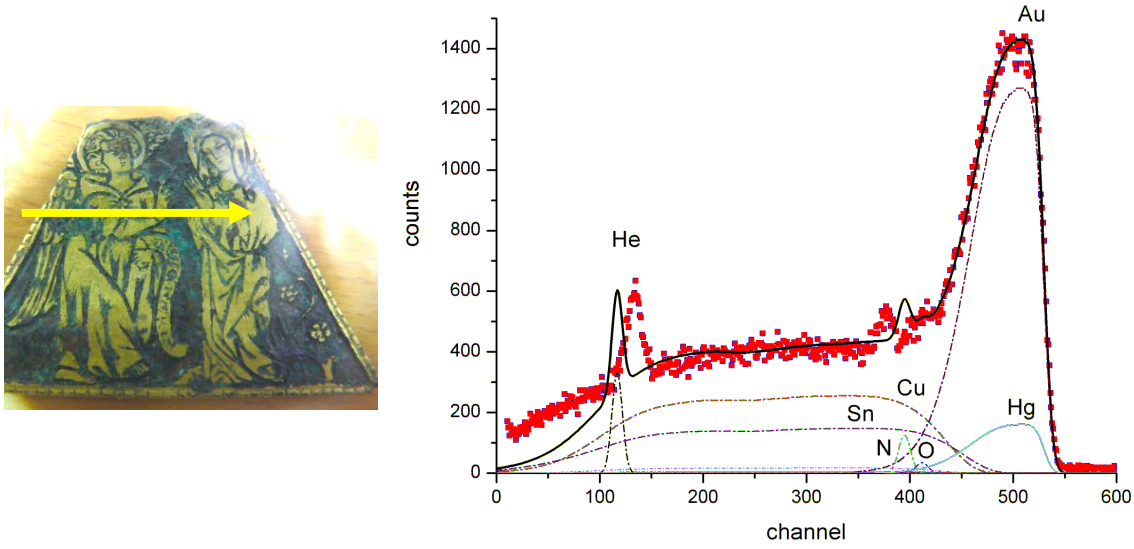

Figure 52: *Gilded artefact with a motive of Mary's annunciation.* Arrow shows the place of the proton impact. The thickness of the Au layer is 2.25 µm (13300e15 at/cm^2) with 11 at% Hg as a consequence of amalgamation. The fitted roughness FWHM is 1.86 µm (11000e15 at/cm^2). The substrate is bronze with traces of iron and silver.

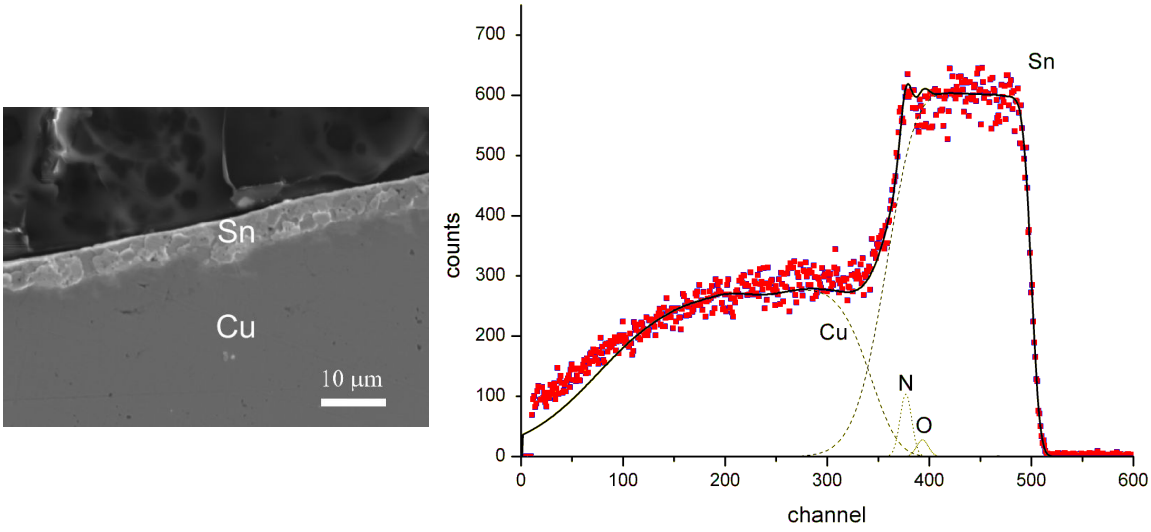

Figure 53: *Sn layer on the top of copper substrate.* A fitted Sn layer thickness is 8.3 µm (30500e15 at/cm^2) and roughness FWHM is 2.7 µm (10000e15 at/cm^2). [8]

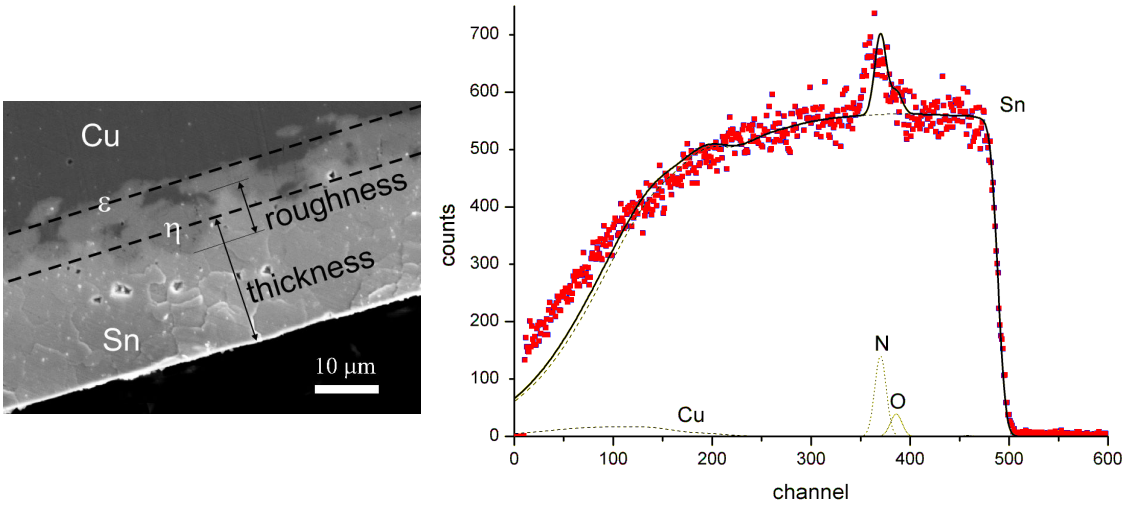

Figure 54: *Sn layer on the top of a copper substrate, annealed for 10 min at 250°C.* η phase (Cu_6Sn_5) and a thin layer of ε phase (Cu_3Sn) can be seen. The fitted Sn layer is 18.9 µm (70000e15 at/cm^2) and the roughness FWHM is 8.1 µm (30000e15 at/cm^2). A fitted η layer: 7.3 µm (27000e15 at/cm^2) and the roughness FWHM of 2.7 µm (10000e15 at/cm^2). [8]

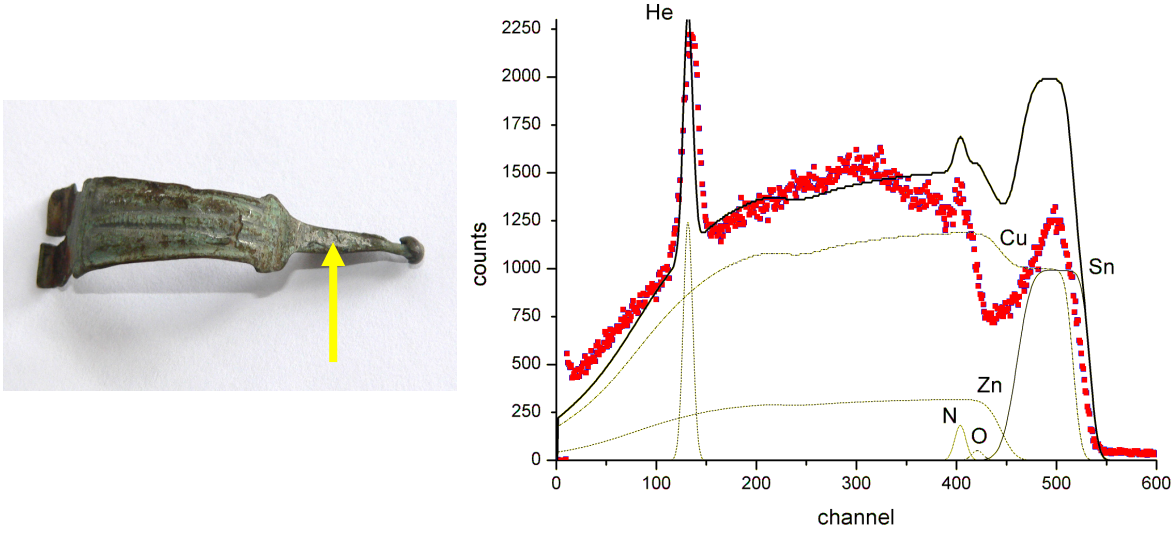

Figure 55: *Tinned Roman brooch.* Arrow shows the place of proton impact. The effect of porosity of the top tin layer is seen. η layer: 10000e15 at/cm^2 (2 µm) and ε layer: 5000e15 at/cm^2 (1 µm). The arrow denotes the point of proton impact. [8]

4 Conclusions

The aim of the work was the development of experimental equipment and numerical procedures for the analysis of targets that depart from simple plane geometry. The achievements were in two directions. One is represented in a construction of a BS analytical system that is now part of the external beamline and is intended for the analysis of layered objects. The second part of the work was development of numerical procedures for the analysis of textile fibres that were assumed to be of cylindrical symmetry.

A BS detector holder with an aluminium nozzle was produced. The volume between the detector and the target was filled with helium to reduce the stopping of back-scattered protons. A flow-meter with a high-precision needle valve was added to regulate the flow of He. During the first trials of the BS energy calibration, we realized that positioning is of utmost importance, and that an energy calibration with a positioning uncertainty above 1 mm is not good enough. Positioning by hand by measuring the distance with a ruler is simply not precise enough. A positioning system with laser triangulation was used to achieve positioning with a reproducibility below 100 μm. The system consists of a red laser with a spot size of 100 μm, and a camera connected to the computer. When the cross on the computer screen and the laser spot overlap, the target is at the required distance from the exit window.

The measurement of proton dose was made with a wire-mesh charge-collecting device, which gives results with low uncertainty as long as the secondary electrons are adequately suppressed. This technique offers more reproducible results than Ar normalization, however some additional restrictions apply. The beam current cannot be reduced using beam deflection, as was common practice before. The distribution of the beam across the beam area has to be homogeneous, so the current has to be changed by defocusing the beam at the injector of the accelerator, which is unpractical. For the same reason the wire-mesh is not useful for beams with a diameter smaller than 0.7 mm. For such beams a chopper method has been developed and can be used as an alternative to the wire-mesh-based device in the same normalization chamber.

Through the analysis of textile fibres we recognized that a geometrical effect is important for evaluation of concentrations in cylindrical targets. The qualitative PIXE analysis of a hypothetical cotton fibre showed that with certain sample diameters (in the case of a 3 MeV proton beam and cotton matrix, these are around 50 μm) the concentration of Si is overestimated by 50% when an intermediate-thickness target model is used instead of our cylindrical target model. What we learn from this example is that we cannot trust the ratios of concentrations between light and heavy elements measured with PIXE without taking the proper geometry into consideration. The geometrical effect is also clearly seen in the microbeam maps of light elements (Si, Cl) in a cotton fibre. We proposed a mathematical model, correcting for the effect; however, the diameter of a fibre enters the equation as a parameter and thus should be measured separately. The model could be used for evaluation of light element concentrations in human hair, which has cylindrical geometry. The concentrations are expected to be more accurate, and thus achieving better agreement with results of the methods like INAA or ICP-MS; however, additional measurements should be done to confirm the suitability of the model for a specific application.

The efficiency of the BS system was demonstrated by the analysis of several layered objects similar to typical cultural heritage samples. Thin layers of Al and Ta foil were measured, and their thicknesses were determined. The thickness and roughness of a gold layer on brass was measured on two military medals and a modern commemorative medal. A layer of gold with traces of mercury was determined on a bronze substrate and thus the process of amalgamation was confirmed on a historic sample. Artificial samples with a layer of tin on copper were produced and annealed. Various phases of inter-metallic alloys were identified with SEM-EDS and with a good agreement confirmed employing the RBS method. An antique sample of a Roman brooch was measured with RBS, confirming the corroded layer of tin on the surface.

The textile fibres showed contents of silicon, probably due to the silicone oil used in the textile production. The PIGE measurements on average showed much higher contents of silicon than PIXE, but on the other hand, the sensitivity for silicon in PIGE is worse than in PIXE, so it was impossible to measure low silicon concentrations with PIGE. Another reason could be that the concentration of silicon in the centre of the fibre is much higher and the information depth is much larger for PIGE than it is for PIXE. A set of white polyester fibres were tested. An average content of 1 mas% of Ti was detected with 9 of 11 fibres, leaving two fibres with content of Ti below 0.05 mas%. Those two fibres contained higher amounts of Ca, which might indicate the use of $CaCO_3$ substance instead of TiO_2 as a whitening medium. Trace elements Mn, Fe, Cu and Zn were present in concentrations below 0.1 mas%. In fibres treated with Teflon, fluorine was detected by PIGE. In anti-bacterial treatment of cotton fibre with nano-silver, the silver itself was not detected, however, the elevated amount of Ti, Zn and Fe were detected in the treated fibre compared to the non-treated.

The results of the fibre analysis employing ion-beam techniques might be useful for forensics, since the detection limit values with PIXE are much lower compared to SEM-EDS, a technique commonly used in forensics. More trace elements could be detected with PIXE, but there is always a question how representative the sample is. To answer this question, further studies should be done. What we can offer to forensic scientists is the model to extract the concentrations of sample with a known cylindrical geometry.

The present achievements are however, not final but represent a good starting point for further development of the beamline This should include the transition to a digital acquisition system. The spectra from all the detectors should be measured simultaneously instead of sequentially, which would also minimize the radiation damage to the sample. The spectrum from a particle detector measured simultaneously with PIXE also enables the use of a self-normalizing measurement where the back-scattered spectrum is used as a measure of projectile beam dose. Further on, the NDF software with the "simulated annealing" data reduction procedures could be used to gather additional information on the sample composition and structure. Digital acquisition would also significantly shorten the acquisition times, due to the possibility of measuring at up to 1000 times higher count-rates. This feature would be most welcome where the PIXE detector is equipped with a nozzle for He flow to reduce the X-ray attenuation in air, thus enabling the measurement of elements down to sodium. Another possibility for the beamline upgrade is a sample-moving PIXE mapping. This can be realized with the xyz positioning table, already installed at the beamline, enabling the mapping of a large area (around 0.5x0.5 m). By such technique it is possible to follow the elemental variations in paintings, coloured decorations, soldered junctions and other examples.

5 References

1. Vogel-Mikuš, K.; Simčič, J.; Pelicon, P.; Budnar, M.; Kump, P.; Nečemer, M.; Mesjasz-Przybyłowicz, J.; Przybyłowicz, W.J.; Regvar, M. Comparison of essential and non-essential element distribution in leaves of the Cd/Zn hyperaccumulator Thlaspi praecox as revealed by micro-PIXE. *Plant, Cell and Environment* **31** (10), 1484-1496 (2008).
2. Gellert, R.; Rieder, R.; Brückner, J.; Clark, B.C.; Dreibus, G.; Klingelhöfer, G.; Lugmair, G.; Ming, D.W.; Wänke, H.; Yen, A.; Zipfel, J.; Squyres, S.W. Alpha Particle X-Ray Spectrometer (APXS): Results from Gusev crater and calibration report. *Journal of Geophysical Research E: Planets* **111** (2), (2006).
3. Mallett, C.L.; O'Meara, J.M.; Maxwell, J.A.; Campbell, J.L. Calibration of the MER α-particle x-ray spectrometer for detection of 'invisible' OH and H2O possibly present in Martian rocks and soils. *X-Ray Spectrometry* **35** (6), 329-337 (2006).
4. Bauman, S.; Houmere, P.D.; Nelson, J.W.; Eldred, R.A.; Cahill, T.A. PIXE analysis of intermediate and thick targets via line intensity ratios. *Nuclear Inst. and Methods in Physics Research, B* **3** (1-3), 203-205 (1984).
5. Jeynes, C.; Bailey, M.J.; Bright, N.J.; Christopher, M.E.; Grime, G.W.; Jones, B.N.; Palitsin, V.V.; Webb, R.P. "Total IBA" - Where Are We?
6. Gurbich, A.F. Evaluated differential cross-sections for IBA. *Nuclear Instruments and Methods in Physics Research, Section B: Beam Interactions with Materials and Atoms* **268** (11-12), 1703-1710 (2010).
7. Grime, G. The "Q factor" method: quantitative microPIXE analysis using RBS normalisation. *Nuclear Instruments and Methods in Physics Research, Section B: Beam Interactions with Materials and Atoms* **109-110**, 170-174 (1996).
8. Jezeršek, D.; Šmit, Z.; Pelicon, P. External beamline setup for plated target investigation. *Nuclear Instruments and Methods in Physics Research, Section B: Beam Interactions with Materials and Atoms* **268** (11-12), 2006-2009 (2010).
9. Brandt, W.; Lapicki, G. Energy-loss effect in inner-shell Coulomb ionization by heavy charged particles. *Physical Review A* **23** (4), 1717-1729 (1981).
10. Šmit, Ž. K-shell ECPSSR cross sections for analytical applications. *Nuclear Inst. and Methods in Physics Research, B* **36** (3), 254-258 (1989).
11. Liu, Z.; Cipolla, S.J. ISICS: A program for calculating K-, L- and M-shell cross sections from ECPSSR theory using a personal computer. *Computer Physics Communications* **97** (3), 315-330 (1996).
12. IAEA - Nuclear Data Service, the Ion Beam Analysis Nuclear Data Library (IBANDL) . http://www-nds.iaea.org/ibandl/ (accessed January 2011).
13. IAEA - Nuclear Data Service, the Experimental Nuclear Reaction Data (EXFOR). http://www-nds.iaea.org/exfor/ (accessed August 2011).

14. Gurbich, A.F. Evaluation of non-Rutherford cross sections for IBA: Theory and results. *Nuclear Instruments and Methods in Physics Research, Section B: Beam Interactions with Materials and Atoms* **261** (1-2 SPEC. ISS.), 401-404 (2007).

15. SigmaCalc 1.6: This service provides evaluated (recommended) differential scattering cross-sections for Ion Beam Analysis. http://www-nds.iaea.org/sigmacalc/ (accessed January 2011).

16. Gosser, D.C.; Ohnersorgen, M.A.; Simon, A.W.; Mayer, J.W. PIXE analysis of Salado polychrome ceramics of the American Southwest. *Nuclear Instruments and Methods in Physics Research, Section B: Beam Interactions with Materials and Atoms* **136-138**, 880-887 (1998).

17. Šmit, Z.; Istenič, J.; Knific, T. Plating of archaeological metallic objects - studies by differential PIXE. *Nuclear Instruments and Methods in Physics Research, Section B: Beam Interactions with Materials and Atoms* **266** (10), 2329-2333 (2008).

18. Yin, M.; Rehren, T.; Zheng, J. The earliest high-fired glazed ceramics in China: the composition of the proto-porcelain from Zhejiang during the Shang and Zhou periods (c. 1700-221 BC). *Journal of Archaeological Science* (Articles not published yet, but available online).

19. Podsiadlo, P.; Shim, B.S.; Kotov, N.A. Polymer/clay and polymer/carbon nanotube hybrid organic-inorganic multilayered composites made by sequential layering of nanometer scale films. *Coordination Chemistry Reviews* **253** (23-24), 2835-2851 (2009).

20. Reuter, F.W.; Smith Jr., H.P. Full-range solution for the measurement of thin-film surface densities with proton-excited x rays. *Journal of Applied Physics* **43** (10), 4228-4232 (1972).

21. Demortier, G.; Ruvalcaba-Sil, J.L. Differential PIXE analysis of Mesoamerican jewelry items. *Nuclear Instruments and Methods in Physics Research, Section B: Beam Interactions with Materials and Atoms* **118** (1-4), 352-358 (1996).

22. Šmit, Ž.; Holc, M. Differential PIXE measurements of thin metal layers. *Nuclear Instruments and Methods in Physics Research, Section B: Beam Interactions with Materials and Atoms* **219-220** (1-4), 524-529 (2004).

23. Pabst, W. Depth profile determination by ion-induced X-ray spectroscopy. *Nuclear Instruments and Methods* **120** (3), 543-545 (1974).

24. Weber, G.; Delbrouck, J.M.; Strivay, D.; Kerff, F.; Martinot, L. Use of a variable incidence angle PIXE arrangement for studying pigment multilayers. *Nuclear Instruments and Methods in Physics Research, Section B: Beam Interactions with Materials and Atoms* **139** (1-4), 196-201 (1998).

25. Weber, G., Strivay, D., Martinot, L., Garnir, H.P. Use of PIXE-PIGE under variable incident angle for ancient glass corrosion measurements. *Nuclear Instruments and Methods in Physics Research, Section B: Beam Interactions with Materials and Atoms* **189** (1-4), 350-357 (2002).

26. Weber, G., Martinot, L., Strivay, D., Garnir, H.P., George, P. Application of PIXE and PIGE under variable ion beam incident angle to several fields of archaeometry. *X-Ray Spectrometry* **34** (4), 297-300 (2005).

27 Bouquillon, A.; Dran, J.-C.; Lagarde, G.; Martinetto, P.; Mathis, F.; Moignard, B.; Salomon, J.; Walter, Ph. In situ dynamic analysis of solids or aqueous solutions undergoing chemical reactions by RBS or PIXE with external beams. *Nuclear*

Instruments and Methods in Physics Research, Section B: Beam Interactions with Materials and Atoms **188** (1-4), 156-161 (2002).

28. Salomon, J.; Dran, J.-C.; Guillou, T.; Moignard, B.; Pichon, L.; Walter, P.; Mathis, F. Ion-beam analysis for cultural heritage on the AGLAE facility: Impact of PIXE/RBS combination. *Applied Physics A: Materials Science and Processing* **92** (1), 43-50 (2008).
29. Ynsa, M.D.; Chamón, J.; Gutiérrez, P.C.; Gomez-Morilla, I.; Enguita, O.; Pardo, A.I.; Arroyo, M.; Barrio, J.; Ferretti, M.; Climent-Font, A. Study of ancient Islamic gilded pieces combining PIXE-RBS on external microprobe with sem images. *Applied Physics A: Materials Science and Processing* **92** (1), 235-241 (2008).
30. De Viguerie, L., Beck, L., Salomon, J., Pichon, L., Walter, Ph. Composition of renaissance paint layers: Simultaneous particle induced X-ray emission and backscattering spectrometry. *Analytical Chemistry* **81** (19), 7960-7966 (2009).
31. Beck, L., Jeynes, C., Barradas, N.P. Characterization of paint layers by simultaneous self-consistent fitting of RBS/PIXE spectra using simulated annealing. *Nuclear Instruments and Methods in Physics Research, Section B: Beam Interactions with Materials and Atoms* **266** (8), 1871-1874 (2008).
32. Bailey, M.J.; Howard, K.T.; Kirkby, K.J.; Jeynes, C. Characterisation of inhomogeneous inclusions in Darwin glass using ion beam analysis. *Nuclear Instruments and Methods in Physics Research, Section B: Beam Interactions with Materials and Atoms* **267** (12-13), 2219-2224 (2009).
33. Bailey, M.J., Jeynes, C. Characterisation of gunshot residue particles using self-consistent ion beam analysis. *Nuclear Instruments and Methods in Physics Research, Section B: Beam Interactions with Materials and Atoms* **267** (12-13), 2265-2268 (2009).
34. Barradas, N.P.; Jeynes, C.; Webb, R.P. Simulated annealing analysis of Rutherford backscattering data. *Applied Physics Letters* **71** (2), 291-293 (1997).
35. Šmit, Ž.; Petru, S.; Grime, G.; Vidmar, T.; Budnar, M.; Zorko, B.; Ravnikar, M. Usewear-induced deposition on prehistoric flint tools. *Nuclear Instruments and Methods in Physics Research, Section B: Beam Interactions with Materials and Atoms* **140** (1-2), 209-216 (1998).
36. Šmit, Ž.; Grime, G.W.; Petru, S.; Rajta, I. Microdistribution and composition of usewear polish on prehistoric stone tools. *Nuclear Instruments and Methods in Physics Research, Section B: Beam Interactions with Materials and Atoms* **150** (1-4), 565-570 (1999).
37. Šmit, Ž.; Budnar, M.; Pelicon, P.; Zorko, B.; Knific, T.; Istenič, J.; Trampuž-Orel, N.; Demortier, G. Analyses of gold artifacts from Slovenia. Nuclear Instruments and Methods in Physics Research, Section B: Beam Interactions with Materials and Atoms **161**, 753-757 (2000).
38. Šmit, Ž.; Pelicon, P. Analysis of copper-alloy fitments on a Roman gladius from the river Ljubljanica. *Arheološki Vestnik* **51**, 183-187 (2000).
39. Šmit, Ž.; Pelicon, P.; Simčič, J.; Istenič, J. Metal analysis with PIXE: The case of Roman military equipment. *Nuclear Instruments and Methods in Physics Research, Section B: Beam Interactions with Materials and Atoms* **239** (1-2), 27-34 (2005).
40. Doberšek, M., Istenič, J., Šmit, Ž. A uniface medallion with a portrait of Augustus from the River Ljubljanica (Slovenia). *Germania* **81** (1), 266-276 (2003).

41. Šmit, Ž.; Istenič, J.; Perovšek, S. PIXE analysis of Late La Téne scabbards with non-ferrous open work plates (and associated swords from Slovenia = Analize PIXE poznolatenskih nočnic s predrtimi okovi (in pripadajočih mečev) iz Slovenije. *Arheološki Vestnik* **61**, 165-173 (2010).

42. Šmit, Ž., Istenič, J., Gerdun, V., Milić, Z., Mladenovič, A. Archaeometric analysis of Alesia group brooches from sites in Slovenia | [Arheometrične analize fibul skupine Alesia s Slovenskih najdišč] *Arheloski Vestnik* **56**, 213-233 (2005).

43. Civici, N.; Gjongecaj, Sh.; Stamati, F.; Dilo, T.; Pavlidou, E.; Polychroniadis, E.K.; Smit, Z. Compositional study of IIIrd century BC silver coins from Kreshpan hoard (Albania) using EDXRF spectrometry. *Nuclear Instruments and Methods in Physics Research, Section B: Beam Interactions with Materials and Atoms* **258** (2), 414-420 (2007).

44. Šmit, Ž.; Šemrov, A. Early medieval coinage in the territory of Slovenia. *Nuclear Instruments and Methods in Physics Research, Section B: Beam Interactions with Materials and Atoms* **252** (2), 290-298 (2006).

45. Šmit, Ž.; Uršič, M.; Pelicon, P.; Trček-Pečak, T.; Šeme, B.; Smrekar, A.; Langus, I., Nemec, I.; Kavkler, K. Concentration profiles in paint layers studied by differential PIXE. *Nuclear Instruments and Methods in Physics Research, Section B: Beam Interactions with Materials and Atoms* **266** (9), 2047-2059 (2008).

46. Šmit, Ž.; Jezeršek, D.; Knific, T.; Istenič, J. PIXE-PIGE analysis of Carolingian period glass from Slovenia. *Nuclear Instruments and Methods in Physics Research, Section B: Beam Interactions with Materials and Atoms* **267** (1), 121-124 (2009).

47. Šmit, Ž.; Pelicon, P.; Vidmar, G.; Zorko, B.; Budnar, M.; Demortier, G.; Gratuze, B.; Šturm, S.; Nečemer, M.; Kump, P.; Kos, M. Analysis of medieval glass by X-ray spectrometric methods. *Nuclear Instruments and Methods in Physics Research, Section B: Beam Interactions with Materials and Atoms* **161**, 718-723 (2000).

48. Šmit, Ž.; Pelicon, P.; Holc, M.; Kos, M. PIXE/PIGE characterization of medieval glass. *Nuclear Instruments and Methods in Physics Research, Section B: Beam Interactions with Materials and Atoms* **189** (1-4), 344-349 (2002).

49. Šmit, Ž.; Janssens, K.; Schalm, O.; Kos, M. Spread of façon-de-Venise glassmaking through central and western Europe. *Nuclear Instruments and Methods in Physics Research, Section B: Beam Interactions with Materials and Atoms* **213**, 717-722 (2004).

50. Šmit, Ž.; Janssens, K.; Bulska, E.; Wagner, B.; Kos, M.; Lazar, I. Trace element fingerprinting of façon-de-Venise glass. *Nuclear Instruments and Methods in Physics Research, Section B: Beam Interactions with Materials and Atoms* **239** (1-2), 94-99 (2005).

51. Šmit, Ž.; Stamati, F.; Civici, N.; Vevecka-Priftaj, A.; Kos, M.; Jezeršek, D. Analysis of Venetian-type glass fragments from the ancient city of Lezha (Albania). *Nuclear Instruments and Methods in Physics Research, Section B: Beam Interactions with Materials and Atoms* **267** (15), 2538-2544 (2009).

52. Kos, M.; Šmit, Ž. PIXE-PIGE analysis of 18-th and early 19th century creamware from Slovenia and Northern Italy. *Journal of Cultural Heritage* **12** (2), 236-242 (2011).

53. Budnar, M.; Vodopivec, J.; Mandò, P.A.; Casu, F.L.G.; Signorini, O. Distribution of chemical elements of iron-gall ink writing studied by the PIXE method. *Restaurator* **22** (4), 228-241 (2001).

54. Kolar, J.; Strlič, M.; Budnar, M.; Malešič, J.; Šelih, V.S.; Simčič, J. Stabilisation of corrosive iron gall inks. *Acta Chimica Slovenica* **50** (4), 763-770 (2003).

55. Budnar, M.; Simčič, J.; Rupnik, Z.; Uršič, M.; Pelicon, P.; Kolar, J.; Strlič, M. In-air PIXE set-up for automatic analysis of historical document inks. *Nuclear Instruments and Methods in Physics Research, Section B: Beam Interactions with Materials and Atoms* **219-220** (1-4), 41-47 (2004).

56. Kolar, J.; Štolfa, A.; Strlič, M.; Pompe, M.; Pihlar, B.; Budnar, M.; Simčič, J.; Reissland, B. Historical iron gall ink containing documents - Properties affecting their condition. *Analytica Chimica Acta* **555** (1), 167-174 (2006).

57. Budnar, M.; Uršič, M.; Simčič, J.; Pelicon, P.; Kolar, J.; Šelih, V.S.; Strlič, M. Analysis of iron gall inks by PIXE. *Nuclear Instruments and Methods in Physics Research, Section B: Beam Interactions with Materials and Atoms* **243** (2), 407-416 (2006).

58. Uršič, M.; Budnar, M.; Simčič, J.; Pelicon, P. The influence of matrix composition and ink layer thickness on iron gall ink determination by the PIXE method. *Nuclear Instruments and Methods in Physics Research, Section B: Beam Interactions with Materials and Atoms* **247** (2), 342-348 (2006).

59. Štupar, J.; Dolinšek, F.; Simicic, J.; Bizjak, M.; Budic, B. Trace element analysis of the hair of Duke Mirko Petrovic-Njegos - A possible means of clarification of his death. *Trace Elements and Electrolytes* **22** (2), 118-126 (2005).

60. Šmit, Ž. Analiza fragmenata tkanina metodom PIXE = Analysis of the textile fragments by the PIXE method. *Diana (Beogr.)* **10**, 147-148 (2004/2005).

61. Vodopivec, J.; Budnar, M.; Pelicon, P. Application of the PIXE method to organic objects. *Nuclear Instruments and Methods in Physics Research, Section B: Beam Interactions with Materials and Atoms* **239** (1-2), 85-93 (2005).

62. Jezeršek, D.; Jakomin, S.; Šmit, Ž. Analysis of textile fibers by in-air PIXE. *Surface and Interface Analysis* **42** (5), 423-428 (2010).

63. Pelicon, P.; Kavčič, M.; Budnar, M.; Simčič, J.; Šmit, Ž.; Mihevc, A.; Duggan, J.L.; McDaniel, F.D. Ion microbeam studies of speleothems in stalagmites from Slovenian Karst. *Int. j. PIXE* **12** (3/4), 181-188 (2002).

64. Šmit, Ž.; Jezeršek, D.; Pelicon, P.; Vavpetič, P.; Jeršek, M.; Mirtič, B. Analysis of a chondrite meteorite from Slovenia. *X-ray Spectrometry* **40** (3), 205-209 (2011).

65. Houck, M.M.; Siegel, J.A. *Fundamentals of Forensic Science*. (Academic Press is an imprint of Elsevier, US/UK, 2010).

66. Enguita, O., Climent-Font, A., García, G., Montero, I., Fedi, M.E., Chiari, M., Lucarelli, F. Characterization of metal threads using differential PIXE analysis. *Nuclear Instruments and Methods in Physics Research, Section B: Beam Interactions with Materials and Atoms* **189** (1-4), 328-333 (2002).

67. Manhita, A., Costa, C., Ferreira, T., Mirão, J., Vargas, H., Ribeiro, I., Seruya, I., (...), Candeias, A. Rediscovering the materials of Arraiolos tapestries: Fibre and mordant analysis by SEM-EDS and μ-PIXE. *Microscopy and Microanalysis* **14** (SUPPL. 3), 91-94 (2008).

68. ASTM E2228 - 10 Standard Guide for Microscopic Examination of Textile Fibers. http://www.astm.org/Standards/E2228.htm (accessed August 2011).

69. Bailey, M.J., Kirkby, K.J., Jeynes, C. Trace element profiling of gunshot residues by PIXE and SEM-EDS: a feasibility study. *X-Ray Spectrometry* **38** (3), 190-194 (2009).

70. Maxwell, J.A.; Campbell, J.L.; Teesdale, W.J. The Guelph PIXE software package. *Nuclear Instruments and Methods in Physics Research, B* **43** (2), 218-230 (1989).

71. Pascual-Izarra, C.; Reis, M.A.; Barradas, N.P. Simultaneous PIXE and RBS data analysis using Bayesian inference with the DataFurnace code. *Nuclear Instruments and Methods in Physics Research, Section B: Beam Interactions with Materials and Atoms* **249** (1-2 SPEC. ISS.), 780-783 (2006).

72. Pascual-Izarra, C.; Barradas, N.P.; Reis, M.A. LibCPIXE: A PIXE simulation open-source library for multilayered samples. *Nuclear Instruments and Methods in Physics Research, Section B: Beam Interactions with Materials and Atoms* **249** (1-2 SPEC. ISS.), 820-822 (2006).

73 Bos, A.J.J.; Van Der Stap, C.C.A.H.; Valković, V.; Vis, R.D.; Verheul, H. On the incorporation of trace elements into human hair measured with micro-PIXE. *Nuclear Inst. and Methods in Physics Research, B* **3** (1-3), 654-659 (1984).

74 Valković, V., Limić, N. Hair analysis: How useful it is and can it be done properly. *Nuclear Inst. and Methods in Physics Research, B* **22** (1-3), 159-162 (1987).

75 Hosseini, A.A.; Amirabadi, A.; Afarideh, H.; Hadji-Saeid, S.M.; Behrozi, A.H. Determination of toxic and non-toxic hair trace elements in tobacco smokers using PIXE and NAA techniques. *Nuclear Instruments and Methods in Physics Research, Section B: Beam Interactions with Materials and Atoms* **109-110**, 239-242 (1996).

76 Chen Jian-xin; Guo Yuan-zhuang; Li Hong-kou; Ren Chi-gang; Tang Guo-hun; Wang Xi-de; Yang Fu-chia; Yao Hui-ying. TRACE ELEMENT ANALYSIS OF HUMAN HAIR BY PIXE. *Nuclear instruments and methods* **181** (1-3), 269-273 (1980).

77. Montenegro, E.C; Baptista, G.B.; De Castro Faria, L.V.; Paschoa, A.S. Correction factor for hair analysis by PIXE. *Nuclear Instruments and Methods* **168** (1-3), 479-483 (1980).

78 Li, H.-K.; Akselsson, K.R. Rutherford backscattering - A tool for quantification of the results of PIXE analysis of single hair strands. *Nuclear Inst. and Methods in Physics Research, B* **12** (2), 265-268 (1985).

79 Li, H.-K.; Akselsson, K.R. A quantitative basis for hair analysis using PIXE. *Nuclear Inst. and Methods in Physics Research, B* **12** (2), 248-256 (1985).

80 Li, H.-K.; Malmqvist, K.G. A simple method for determining the elemental distribution over the transverse cross section of a hair. *Nuclear Inst. and Methods in Physics Research, B* **12** (2), 257-264 (1985).

81 Campbell, J.L.; Faiq, S.; Gibson, R.S.; Russell, S.B. Proton backscatter as a means of mass measurement in PIXE analysis of hair. *Nuclear Instruments and Methods* **178** (2-3), 601-606 (1980).

82. Beasley, D.; Gomez-Morilla, I.; Spyrou, N. Elemental analysis of hair using PIXE-tomography and INAA. *Journal of Radioanalytical and Nuclear Chemistry* **276** (1), 101-105 (2008).

83. Kertész, Zs.; Szikszai, Z.; Pelicon, P.; Simčič, J.; Telek, A.; Bíró, T. Ion beam microanalysis of human hair follicles. *Nuclear Instruments and Methods in Physics Research, Section B: Beam Interactions with Materials and Atoms* **260** (1), 218-221 (2007).

84. Ziegler, J. F. Energy loss. In: Tesmer, J. R.; Natasi, M. (ed.) *Handbook of Modern Ion Beam Materials Analysis*. 3-21 (Materials research society (MRS), Pittsbourgh, Pennsylvania, 1995).

85. Ziegler, J. F.; Biersack, J. P.; Littmark, U. *The Stopping and Range of Ions in Solids*, Vol. 1 (Pergamon Press, New York, 1985).

86. Chu, W.K. *Accelerators in Atomic Physics* (Richard, P. (ed.), Academic Press, New York 1979).

87. Bauer, P. How to measure absolute stopping cross sections by backscattering and by transmission methods : Part I. backscattering. *Nuclear Instruments and Methods in Physics Research Section B: Beam Interactions with Materials and Atoms* **27** (2), 301 (1987).

88. Mertens, P. How to measure absolute stopping cross sections by backscattering and transmission methods : Part II. transmission. *Nuclear Instruments and Methods in Physics Research Section B: Beam Interactions with Materials and Atoms* **27** (2), 315 (1987).

89. Powers, D. An overview of current stopping power phenomena, measurements, and related topics. *Nuclear Instruments and Methods in Physics Research Section B: Beam Interactions with Materials and Atoms* **40/41**, 324 (1989).

90. Paul, H. New developments in stopping power for fast ions. *Nuclear Instruments and Methods in Physics Research, Section B: Beam Interactions with Materials and Atoms* **261** (1-2 SPEC. ISS.), 1176-1179 (2007).

91. James Ziegler SRIM & TRIM. http://www.srim.org/ (accessed March 2010).

92. Ziegler, J.F., Ziegler, M.D., Biersack, J.P. SRIM - The stopping and range of ions in matter (2010). *Nuclear Instruments and Methods in Physics Research, Section B: Beam Interactions with Materials and Atoms* **268** (11-12), 1818-1823 (2010).

93. Ziegler, J.F. SRIM-2003. *Nuclear Instruments and Methods in Physics Research, Section B: Beam Interactions with Materials and Atoms* **219-220** (1-4), 1027-1036 (2004).

94. Scopus - Document search result (Author: Ziegler, J.F.; Title: SRIM-2003). http://www.scopus.com (accessed June 2011).

95. Šmit, Ž. Metoda PIXE. In: *Spektroskopske metode s pospešenimi ioni*. (DMFA - založništvo, Ljubljana 2003).

96. Leavitt, A.; McIntyre Jr., L. C. Backscattering Spectrometry. In: Tesmer, J. R.; Natasi, M. (ed.) *Handbook of Modern Ion Beam Materials Analysis*. 37- 83 (Materials research society - MRS, Pittsbourgh, Pennsylvania, 1995).

97. Honerkamp, J.; Römer, H. *Klassische Theoretische Physik. Eine Einführung*. 42 (Springer-Verlag, Berlin, 1989).

98. Šmit, Ž. Light-ion-induced K-shell ionization in the adiabatic region. *Physical Review A* **46** (3), 1367-1373 (1992).

99. Andersen, H. H.; Besenbacher, F.; Loftager, P.; Möller, W. Large-angle scattering of light ions in the weakly screened Rutherford region. *Physical Review A* **21** (6), 1891-1901 (1980).

100. Langley, R.A. In: Walson, J. S. ; Wiffen, F. W. (eds.) *Proceedings of International Conference on Radiation Effect and Tritium Technology for Fusion Reactors, vol IV*. 158 (US Department of Commerce, Springfield, VA, USA, 1976).

101. Ramos, A.R. et al. Measurement of (p,p) elastic differential cross-sections for carbon, nitrogen, oxygen, aluminium and silicon in the 500-2500 keV range at 140° and 178° laboratory scattering angles. *Nuclear Instruments and Methods in Physics*

Research, Section B: Beam Interactions with Materials and Atoms 190 (1-4), 95-99 (2002).

102. Mayer, M. *SIMNRA User's Guide 6.05*. (Max-Planck-Institut für Plasmaphysik, Garching, Germany, 2009).

103. Mayer, M.; Arstila, K.; Nordlund, K.; Edelmann, E.; Keinonen, J. Multiple scattering of MeV ions: Comparison between the analytical theory and Monte-Carlo and molecular dynamics simulations. *Nuclear Instruments and Methods in Physics Research, Section B: Beam Interactions with Materials and Atoms* **249**, 823 (2006).

104. Barradas, N.P.; Arstila, K.; Battistig, G.; Bianconi, M.; Dytlewski, N.; Jeynes, C.; Kótai, E.; Lulli, G.; Mayer, M.; Rauhala, E.; Szilágyi, E.; Thompson, M. International Atomic Energy Agency intercomparison of ion beam analysis software. *Nuclear Instruments and Methods in Physics Research, Section B: Beam Interactions with Materials and Atoms* **262** (2), 281-303 (2007).

105. Barradas, N.P.; Arstila, K.; Battistig, G.; Bianconi, M.; Dytlewski, N.; Jeynes, C.; Kótai, E.; Lulli, G.; Mayer, M.; Rauhala, E.; Szilágyi, E.; Thompson, M. Summary of "IAEA intercomparison of IBA software". *Nuclear Instruments and Methods in Physics Research, Section B: Beam Interactions with Materials and Atoms* **266** (8), 1338-1342 (2008).

106. Jeynes, C.; Barradas, N.P.; Marriott, P.K.; Boudreault, G.; Jenkin, M.; Wendler, E.; Webb, R.P. Elemental thin film depth profiles by ion beam analysis using simulated annealing - A new tool. *Journal of Physics D: Applied* Physics **36** (7), R97-R126 (2003).

107. Wielopolski, L.; Gardner, R.P. Prediction of the pulse-height spectral distortion caused by the peak pile-up effect. *Nuclear Instruments and Methods* **133** (2), 303-309 (1976).

108. Wielopolski, L.; Gardner, R.P. A generalized method for correcting pulse-height spectra for the peak pile-up effect due to double sum pulses. Part II. The inverse calculation for obtaining true from observed spectra. *Nuclear Instruments and Methods* **140**, 297-303 (1977).

109. Szilágyi, E.; Pászti, F.; Amsel, G. Theoretical approximations for depth resolution calculations in IBA methods. *Nuclear Instruments and Methods in Physics Research, B* **100** (1), 103-121 (1995).

110. Eckstein, W.; Mayer, M. Rutherford Backscattering from Layered Structures beyond the Single Scattering Model. *Nuclear Instruments and Methods in Physics Research Section B: Beam Interactions with Materials and Atoms* **153**, 337 (1999).

111. Szilágyi, E. Energy spread in ion beam analysis. *Nuclear Instruments and Methods in Physics Research, Section B: Beam Interactions with Materials and Atoms* **161**, 37-47 (2000).

112. L'Ecuyer, J.; Davies, J.A.; Matsunami, N. How accurate are absolute rutherford backscattering yields. *Nuclear Instruments and Methods* **160** (2), 337-346 (1979).

113. Knudson, A.R. Effects of surface roughness on backscattering spectra. *Nuclear Instruments and Methods in Physics Research, B* **168** (1-3), 163-167 (1980).

114. Mayer, M. Ion Beam Analysis of Rough Thin Films. *Nuclear Instruments and Methods in Physics Research, Section B: Beam Interactions with Materials and Atoms* **194**, 177 (2002).

115. Barradas, N.P. Rutherford backscattering analysis of thin films and superlattices with roughness. *Journal of Physics D: Applied Physics* **34** (14), 2109 (2001).

116. Mayer, M. *SIMNRA User Guide. Technical Report IPP 9/113.* (Max Plank Institut Fur Plasmaphysik, Garching, Germany, 1997).

117. Simon, A.; Pászti, F.; Uzonyi, I.; Manuaba, A.; Kiss, Á.Z. Application of grazing exit angle in RBS microprobe measurements. *Nuclear Instruments and Methods in Physics Research, Section B: Beam Interactions with Materials and Atoms* **136-138**, 350-356 (1998).

118. Merchant, M.J.; Mistry, P.; Browton, M.; Clough, A.S.; Gauntlett, F.E.; Jeynes, C.; Kirkby, K.J.; Grime, G.W. Characterisation of the University of Surrey Ion Beam Centre in-air scanning microbeam. *Nuclear Instruments and Methods in Physics Research, Section B: Beam Interactions with Materials and Atoms* **231** (1-4), 26-31 (2005).

119. Salomon, J.; Dran, J.-C.; Guillou, T.; Moignard, B.; Pichon, L.; Walter, P.; Mathis, F. Present and future role of ion beam analysis in the study of cultural heritage materials: The example of the AGLAE facility. *Nuclear Instruments and Methods in Physics Research, Section B: Beam Interactions with Materials and Atoms* **266** (10), 2273-2278 (2008).

120. Dran, J.-C.; Salomon, J.; Calligaro, T.; Walter, P. Ion beam analysis of art works: 14 Years of use in the Louvre. *Nuclear Instruments and Methods in Physics Research, Section B: Beam Interactions with Materials and Atoms* **219-220** (1-4), 7-15 (2004).

121. Ortega, R.; Devès, G.; Moretto, Ph. In-air scanning transmission ion microscopy of cultured cancer cells. *Nuclear Instruments and Methods in Physics Research, Section B: Beam Interactions with Materials and Atoms* **181** (1-4), 475-479 (2001).

122. Giuntini, L.; Massi, M.; Calusi, S. The external scanning proton microprobe of Firenze: A comprehensive description. *Nuclear Instruments and Methods in Physics Research, Section A: Accelerators, Spectrometers, Detectors and Associated Equipment* **576** (2-3), 266-273 (2007).

123. Calcagnile, L.; Quarta, G.; D'Elia, M.; Muscogiuri, D.; Maruccio, L.; Butalag, K.; Gianfrate, G.; Sanapo, C.; Toma, U. Instrumental developments at the IBA-AMS dating facility at the University of Lecce. *Nuclear Instruments and Methods in Physics Research, Section B: Beam Interactions with Materials and Atoms* **240** (1-2), 22-25 (2005).

124. Reiche, I.; Britzke, R.; Bukalis, G.; Reinholz, U.; Weise, H.-P.; Gadebusch, R.D. An external PIXE study: Mughal painting pigments. *X-Ray Spectrometry* **34** (1), 42-45 (2005).

125. Fazinić, S. Utilization of the RBI tandem accelerator facility for analytical applications. *International Topical Meeting on Nuclear Research Applications and Utilization of Accelerators*, 31 (2009).

126. Sokaras, D.; Bistekos, E.; Georgiou, L.; Salomon, J.; Bogovac, M.; Aloupi-Siotis, E.; Paschalis, V.; Aslani, I.; Karabagia, S.; Lagoyannis, A.; Harissopulos, S.; Kantarelou, V., Karydas, A.-G. The new external ion beam analysis setup at the Demokritos Tandem accelerator and first applications in cultural heritage. *Nuclear Instruments and Methods in Physics Research, Section B: Beam Interactions with Materials and Atoms* **269** (5), 519-527 (2011).

127. Respaldiza, M. A.; Ager, F. J.; Carmona, A.; Ferrer, J.; García-León, M.; García-López, J.; García-Orellana, I.; Gómez-Tubío, B.; Morilla, Y.; Ontalba, M. A.; Ortega-

Feliu, I. Accelerator-based research activities at "Centro Nacional de Aceleradores", Seville (Spain) *Nuclear Instruments and Methods in Physics Research, Section B: Beam Interactions with Materials and Atoms* **266** (10), 2105-2109 (2008).

128. Enguita, O.; Fernández-Jiménez, M.T.; García, G.; Climent-Font, A.; Calderón, T.; Grime, G.W. The new external microbeam facility at the 5 MV Tandetron accelerator laboratory in Madrid: Beam characterisation and first results. *Nuclear Instruments and Methods in Physics Research, Section B: Beam Interactions with Materials and Atoms* **219-220** (1-4), 384-388 (2004).

129. Andrade, E.; Murillo, G.; Policroniades, R.; Acosta, L.; Zavala, E.P.; Rocha, M.F.; Centeno, S.A. IBA analysis of some precolumbian gilded-copper samples. *Nuclear Instruments and Methods in Physics Research, Section B: Beam Interactions with Materials and Atoms* **240** (1-2), 570-575 (2005).

130. MacLaren, S.A.; Correll, F.D.; Huddle, J.R.; Vanhoy, J.; Kulp III, W.D. A simple external-beam ion milliprobe system for in-air PIXE. *Nuclear Instruments and Methods in Physics Research, B* **56-57** (2), 708-711 (1991).

131. Doyle, B.L.; Walsh, D.S.; Lee, S.R. External micro-ion-beam analysis (X-MIBA). *Nuclear Instruments and Methods in Physics Research, B* **54** (1-3), 244-257 (1991).

132. Sakai, T; Kamiya, T.; Oikawa, M.; Sato, T.; Tanaka, A.; Ishii, K. Development of in-air micro-pixe analysis and data sharing systems in JAERI Takasaki. *International Journal of PIXE* **10** (3-4), 91-95 (2000).

133. Yasuda, K.; Ito, Y.; Ishigami, R.; Takagi, K.; Hatashita, M.; Hatori, S. PIXE measurement system at the Wakasa Wan Energy Research Center. *International Journal of PIXE* **10** (3-4), 97-100 (2000).

134. Yasuda, K.; Nomachi, M.; Sugaya, Y.; Yamamoto, H.; Komatsu, H. Progress of in-air microbeam system at the Wakasa Wan Energy Research Center. *Nuclear Instruments and Methods in Physics Research, Section B: Beam Interactions with Materials and Atoms.* [Article in Press, DOI: 10.1016/j.nimb.2011.02.026] (2011).

135. Giuntini L. A review of external microbeams for ion beam analyses. *Analytical and Bioanalytical Chemistry*. [Available online 17 April 2011. DOI: 10.1007/s00216-011-4889-3] (2011).

136. Yang, C.; Jamieson, D.N.; Hearne, S.M.; Pakes, C.I.; Rout, B.; Gauja, E.; Dzurak, A.J.; Clark, R.G. Ion-beam-induced-charge characterisation of particle detectors. *Nuclear Instruments and Methods in Physics Research, Section B: Beam Interactions with Materials and Atoms* **190** (1-4), 212-216 (2002).

137. Chiari, M.; Lucarelli, F.; Mazzei, F.; Nava, S.; Paperetti, L.; Prati, P.; Valli, G.; Vecchi, R. Characterization of airborne particulate matter in an industrial district near Florence by PIXE and PESA. *X-Ray Spectrometry* **34** (4), 323-329 (2005).

138. Chiari, M.; Migliori, A.; Mandò, P.A. Measurement of low currents in an external beam set-up. *Nuclear Instruments and Methods in Physics Research, Section B: Beam Interactions with Materials and Atoms* **188** (1-4), 162-165 (2002).

139. Pászti, F.; Manuaba, A.; Hajdu, C.; Melo, A.A.; Da Silva, M.F. Current measurement on MeV energy ion beams. *Nuclear Instruments and Methods in Physics Research, B* **47** (2), 187-192 (1990).

140. Musket, R.G.; Daley, R.S.; Patterson, R.G. Spinning-wire dosimetry for ion-beam analysis of materials. *Nuclear Instruments. and Methods in Physics Research, B* **83** (3), 425-429 (1993).

141. Piel, N.; Berheide, M.; Polaczyk, Ch.; Rolfs, C.; Schulte, W.H. Ion dose determination using beam chopper techniques. *Nuclear Inst. and Methods in Physics Research, A* **349** (1), 18-26 (1994).

142. Bartha, L.; Uzonyi, I. Ion beam dose measurement in nuclear microprobe using a compact beam chopper. *Nuclear Instruments and Methods in Physics Research, Section B: Beam Interactions with Materials and Atoms* **161**, 339-343 (2000).

143. Auzelyte, V.; Andersson, F.; Elfman, M.; Kristiansson, P.; Pallon, J.; Wegdén, M.; Nilsson, C.: Arteaga Marrero, N. On-line measurement of proton beam current in pA range. *Nuclear Instruments and Methods in Physics Research, Section B: Beam Interactions with Materials and Atoms* **249** (1-2 SPEC. ISS.), 760-763 (2006).

144. Calligaro, T.; Dran, J.-C.; Ioannidou, E.; Moignard, B.; Pichon, L.; Salomon, J. Development of an external beam nuclear microprobe on the aglae facility of the Louvre museum. *Nuclear Instruments and Methods in Physics Research, Section B: Beam Interactions with Materials and Atoms* **161**, 328-333 (2000).

145. El Bouanani, M.; Pelicon, P.; Razpet, A.; Cadez, I.; Budnar, M.; Simcic, J.; Markelj, S. Simple and accurate spectra normalization in ion beam analysis using a transmission mesh-based charge integration. *Nuclear Instruments and Methods in Physics Research Section B: Beam Interactions with Materials and Atoms* **243**, 392-396 (2006).

146. Ohmori, C.; Kanazawa, M.; Takagi, A.; Noda, K.; Uesugi, T.; Shirakabe, Y.; Sugiura, A.; Mori, Y.; Muto, M.; Chou, W. Beam diagnostics using a chopped beam. *Nuclear Instruments and Methods in Physics Research, Section A: Accelerators, Spectrometers, Detectors and Associated Equipment* **526** (3), 215-221 (2004).

147. Chiari, M.; Carmine, P.D.; Orellana, I.G.; Lucarelli, F.; Nava, S.; Paperetti, L. Hourly elemental composition and source identification of fine and coarse PM10 in an Italian urban area stressed by many industrial activities. *Nuclear Instruments and Methods in Physics Research, Section B: Beam Interactions with Materials and Atoms* **249** (1-2 SPEC. ISS.), 584-587 (2006).

148. Kertész, Zs.; Szikszai, Z.; Gontier, E.; Moretto, P.; Surlève-Bazeille, J.-E.; Kiss, B.; Juhász, I.; Hunyadi, J.; Kiss, Á.Z. Nuclear microprobe study of TiO2-penetration in the epidermis of human skin xenografts. *Nuclear Instruments and Methods in Physics Research, Section B: Beam Interactions with Materials and Atoms* **231** (1-4), 280-285 (2005).

149. Beckhoff, B.; Kanngießer, B.; Langhoff, N.; Wedell, R.; H.Wolff, H. *Handbook of Practical X-Ray Fluorescence Analysis* (Springer, Berlin 2005).

150. X-ray Fluorescence (XRF): Oxford Instruments. http://oxinst.eu/applications-markets/environment/environmental-monitoring/rohs/Pages/x-ray-fluorescence-xrf.aspx (accessed November 2010).

151. XR-100CR Additional Performance Spectra and Detector Properties. http://www.amptek.com/xrspectr.html (accessed July 2011).

152. DeYoung, P.A.; Hall, C.C.; Mears, P.J.; Padilla, D.J.; Sampson, R.; Peaslee, G.F. Comparison of glass fragments using particle-induced X-ray emission (PIXE) spectrometry. *Journal of Forensic Sciences* **56** (2), 366-371 (2011).

153. Jisonna, L.J.; DeYoung, P.A.; Ferens, J.; Hall, C.; Lunderberg, J.M.; Mears, P.; Padilla, D.; Peaslee, G.F.; Sampson, R. Forensic analysis of tempered sheet glass by particle induced X-ray emission (PIXE). *Nuclear Instruments and Methods in Physics Research, Section B: Beam Interactions with Materials and Atoms* **269** (10), 1067-1070 (2011).

154. Fischbeck, H.J.; Ryan, S.R.; Snow, C.C. Detection of bullet residue in bone using proton-induced X-ray emission (PIXE) analysis. *Journal of Forensic Sciences* **31** (1), 79-85 (1986).

155. Vogt, C.; Becker, A.; Vogt, J. Investigation of ball point pen inks by capillary electrophoresis (CE) with UV/Vis absorbance and laser induced fluorescence detection and Particle Induced X-Ray Emission (PIXE). *Journal of Forensic Sciences* **44** (4), 819-831 (1999).

156. Lane, D.W.; Wicks, D.C. PIXE, a new technique for the trace element analysis of high explosives. *Nuclear Instruments and Methods in Physics Research, Section B: Beam Interactions with Materials and Atoms* **161**, 792-796 (2000).

157. Grime, G.W.; Abraham, M.H.; Marsh, M.A. The new external beam facility of the Oxford scanning proton microprobe. *Nuclear Instruments and Methods in Physics Research, Section B: Beam Interactions with Materials and Atoms* **181** (1-4), 66-70 (2001).

158. Akselsson, R.; Johansson, T. B. X-Ray Production by 1.5-11 MeV Protons. *Zeitschrift für Physik A Hadrons and Nuclei* **266** (4), 245-255 (1974).

159. Basbas, G.; Brandt, W.; Laubert, R. Universal cross sections for K-shell ionization by heavy charged particles. II. Intermediate particle velocities. *Physical Review A* **17** (5), 1655-1674 (1978).

160. Barradas, N.P.; Marriott, P.K.; Jeynes, C.; Webb, R.P. The RBS data furnace: Simulated annealing. *Nuclear Instruments and Methods in Physics Research, Section B: Beam Interactions with Materials and Atoms* **136-138**, 1157-1162 (1998).

161. Maxwell, J. A.; Teesdale, W. J.; Campbell, J. L. The Guelph PIXE software package II. *Nuclear Instruments and Methods in Physics Research B* **95**, 407-421(1995).

162. Campbell, J. L.; Hopman, T. L.; Maxwell, J. A.; Nejedly, Z. The Guelph PIXE software package III: Alternative proton database. *Nuclear Instruments and Methods in Physics Research B* **170**, 193-204 (2000).

163. Certified reference material BCR - 126A. http://www.irmm.jrc.be/html/reference_materials_catalogue/catalogue/attachements/BCR-126A_cert.pdf (accessed May 2011).

164. Certificate SRM 620 - Soda Lime, Flat. https://www-s.nist.gov/srmors/view_cert.cfm?srm=620 (accessed May 2011).

165. Maenhaut, W.; Vandenhaute, J. Accurate Analytic Fitting of Pixe Spectra. *Bulletin des Sociétés Chimiques Belges* **95** (5-6), 407–418 (1986).

166. Vekemans, B.; Janssens, K.; Vincze, L.; Adams, F.; Van Espen P. Analysis of X-ray spectra by iterative least squares (AXIL): New developments. *X-Ray Spectrometry* **23** (6), 278–285 (1994).

167. Center for X-ray optics at Lawrence Berkeley National Laboratory: Filter Transmission. http://henke.lbl.gov/optical_constants/filter2.html (accessed January 2011).

168. Weaving - Wikipedia, the free encyclopedia. http://en.wikipedia.org/wiki/Weaving (accessed May 2010).

169. Savidou, A.; Aslanoglou, X.; Paradellis, T.; Pilakouta, M. Proton induced thick target γ-ray yields of light nuclei at the energy region Ep = 1.0-4.1 MeV. *Nuclear*

Instruments and Methods in Physics Research, Section B: Beam Interactions with Materials and Atoms **152** (1), 12-18 (1999).

170. Felicissimo, M. P.; Peixoto, J. L.; Barbosa, M. S.; Demortier, G.; Pireaux, J.-J.; Rodrigues-Filho, U. P. PIXE and PIGE analysis of pre-colonial pottery from Patanal – MS, Brazil. *Journal of Radioanalytical and Nuclear Chemistry* **267**, 209–217 (2006).
171. Jembrih, D.; Neelmeijer, C.; Schreiner, M.; Mäder, M.; Ebel, M.; Svagera, R.; Peev, M. Iridescent Art Nouveau glass - IBA and XPS for the characterisation of thin iridescent layers. *Nuclear Instruments and Methods in Physics Research, Section B: Beam Interactions with Materials and Atoms* **181** (1-4), 698-702 (2001).
172. Grime, G.W.; Dawson, M. A PC-based data acquisition package for nuclear microbeam systems. *Nuclear Inst. and Methods in Physics Research, B* **89** (1-4), 223-228 (1994).
173. Markač, Dejan. *Energijska kalibracija pospeševalnika Tandetron.* Diploma work (2009).

Index of Figures

Figure 1: *The scattering geometry of Rutherford backscattering*. The energy of the incoming projectiles is E_0, the energy just before scattering from the atom is E', immediately after scattering it is kE', and the energy of an outgoing projectile when leaving the target is E. [12] 10

Figure 2: The scattering cross-section relative to the Rutherford backscattering cross-section for collisions of protons on He atoms corrected with the SigmaCalc program for an angle of 151°. Continuous increase from 80 to 310 times at energies from 1.6 to 2.7 MeV is shown. [15] 12

Figure 3: The scattering cross-section relative to the Rutherford backscattering for an (α,α) reaction on ^{16}O atom corrected with the SigmaCalc program for an angle of 151°. A sharp non-Rutherford resonance (12 times larger cross-section compared to the Rutherford value) at an energy of 3.038 MeV can be observed. [15] 12

Figure 4: *RBS spectra of a homogeneous sample simulated by SIMNRA program* [102]. Spectrum of a thick mono-elemental target (copper) (a), thick homogeneous multi-element target (Al77Fe20Pb3) (b). Spectra are calculated for scattering of 3 MeV protons with geometry (α=0, ψ=45°, θ=135°) in the full energy range with a cut-off energy of 10 keV. In graph (b) a multiple-scattering calculation was used to get better agreement at low energies. 15

Figure 5: *RBS spectra of a two-layered sample simulated in the SIMNRA program* [102]. The top layer consisting of two sorts of atoms and the second layer being a light mono-elemental substrate (a, b). Spectra are calculated for scattering of 3 MeV protons with geometry (α=0, ψ=45°, θ=135°). The horizontal energy axis is limited to the highest 30% of the whole spectrum to zoom in the affected part. Spectrum (a) is calculated for a 5000e15 at/cm^2 layer of Zn97Pb3 on top of the aluminium substrate and spectrum (b) is calculated for a thicker layer (12000e15 at/cm^2) on the same substrate. The detector resolution and the energy spread of the incident beam were set to zero to simplify the understanding. Some energy spread still remains as a consequence of the energy straggling of protons in a helium atmosphere along the path to the detector. 15

Figure 6: *Geometry of a scattering experiment as treated by SIMNRA* [102]. Incident angle α, exit angle β and scattering angle θ. Angles α and β are always positive and always measured from the target normal. 17

Figure 7: *A simulated signal from a thin layer vs. incident angle*. Detection of a thin layer can be increased up to a factor of 60 when the incident angle reaches 89°. 17

Figure 8: *The schematics of the RBS experimental setup*. The incident angle is 0° and the scattering angle is 151°. [8] 19

Figure 9: *An RBS spectrum simulated in a SIMNRA program, with realistic parameters*. The red line is a simulated graph of particles backscattered from a gold plated silicon with helium filling the space between the target and the detector and the black line is the same sample with the same setup, the only difference is that the gap is filled with air. A much worse energy resolution can be observed. 19

Figure 10: *A flow-meter with precision needle valve at external beamline at Microanalytical center at Jožef Stefan Institute*. The flow-meter is necessary to ensure the constant flow of helium gas to the target. 20

Figure 11: *Count-rate vs. distance to the target.* Optimal distance d_{opt} was determined in the region of the count-rate maximum. 20

Figure 12: *The positioning system at Microanalytical center at Jožef Stefan Institut*. A focused laser mounted on a micro-positioning stage and a camera connected to the computer are parts of the laser-triangulation positioning system. 21

Figure 13: *The wire-mesh based charge-collecting normalization device*. The negative bias at the shield electrodes in front and behind the central wire-mesh prevents variation of the positive current on account of the emission of secondary electrons. [145] 23

Figure 14: *The wire-mesh charge-collecting device installed on external beamline at Microanalytical center at Jožef Stefan Institut*. The collimator is made of tantalum, with a hole of 0.7 mm diameter. Wire-mesh is Pt-Rh alloy 80 x 80 mesh, the wire diameter is 0.003 inch (76.2 μm). [8] 23

Figure 15: *The chamber with a chopper propeller at the external beamline at the University of Surrey with a projected path of the beam*. RBS detector with the possibility of changing filters and a turn table for observing the beam on a quartz screen. 25

Figure 16: *Upper and lower cover of the chopper-based normalization device at MIC with a projected path of the beam.* An in-vacuum motor with a chopper propeller is fixed to the upper cover and an RBS detector on the lower cover of the normalization chamber. The gold plated carbon pieces on the chopper propeller are missing. 26

Figure 17: *Secondary X-ray production scheme.* XRF is based on detection of secondary X-rays induced by incident X-rays. [150] 28

Figure 18: *X-ray fluorescence (XRF) of multi-element sample from ^{109}Cd cathode.* Spectrum is in linear scale. It depictures the capability of simultaneous multi-elemental analyses of XRF method. [151] 28

Figure 19: *SEM-EDS vs. PIXE spectrum.* Comparison of SEM-EDS and PIXE spectrum of textile fibre in a logarithmic scale. Both spectra were measured for 10 minutes. Spectra are normalized to the height of the highest identified peak, however the height of a detected peak in a SEM-EDS spectrum was 106 times lower than the height of a peak in PIXE spectrum. 29

Figure 20: *The schematics of PIXE thick target geometry*. The energy of the incident projectiles E_1 decreases to E along the path z. Absorption along the escape path ξ is taken into account in Eqn (28). [95] 32

Figure 21: *A schematic for the integration of a cylindrical target.* Exit length ξ varies across the diameter of the cylinder. [62] 35

Figure 22: *The influence of cylindrical geometry*. The model for the cylindrical target was compared to the simpler model of ribbon geometry, assuming a square cross-section with a side of 2*R*. Much higher concentrations in a target are assumed with the light elements (Si, Ca) when the ribbon geometry model is used, however when the diameter of a cylindrical target approaches zero, the concentrations calculated with ribbon geometry model are underestimated due to difference in the area of the cross-section (square vs. circle area, where side of a square is a diameter of a circle). 37

Figure 23: *The improved ribbon model vs. model of cylindrical geometry*. The area of both cross-sections are the same. 38

Figure 24: *The improved ribbon model vs. cylindrical geometry model*. The model for a cylindrical target was compared to an improved ribbon model. The cross-section area of both mathematical models are the same. The concentrations calculated with the improved ribbon model are overestimated, but accurate when the diameter approaches zero. The largest difference is with lightest elements (Si, Ca). 39

Figure 25: *The model for the calculation of the projectile density P* on the target for a broad exit collimator of radius R_d. Area fractions dS contribute dN_p to the projectile areal density. [62] 40

Figure 26: *The calculated projectile areal density at the target.* The primary beam diameter was 0.5 mm and three different values of σ' were assumed. The distribution tends towards a Gaussian with a decreasing R_d/σ' ratio. [62] 41

Figure 27: *The external chopper with Ti wire at MIC, JSI*, used as an alternative to the Ar dose measurement, before the in-vacuum wire-mesh was installed. 42

Figure 28: *The measured beam profile for an 8 μm aluminium exit window* and a 1 cm air gap at the position of the target. Fitted width (2σ) is 0.483 ± 0.005 mm. [62] 42

Figure 29: *The measured beam profile for a 2 μm tantalum exit window* and a 1 cm air gap at the position of the target. Normalized according to the Ar signal from the air and the signal from the in-air chopper. The fitted widths (2σ) are 1.029 ± 0.003 mm and 1.070 ± 0.004 mm, accordingly. [62] 43

Figure 30: *The ratio between the X-ray intensities from the air argon and titanium chopper*. The wire shadows the Ar signal, but the Ti signal from the chopper is independent of the wire position. The line is a fitted Gaussian. [62] 43

Figure 31: *The external beam experimental setup at Microanalytical center at Jožef Stefan Institute* with the PIXE, PIGE and RBS detectors. Normalization chamber with the wire-mesh-based charge-collecting device is seen, as well as the positioning system with a camera and a laser fixed on a micro-positioning stage. 48

Figure 32: *X-ray transmission of various filters*. X-ray transmission of a 100 μm and 300 μm Al foil and a 300 μm Kapton® ($C_{22}O_5N_2H_{10}$) polymer foil. [167] 49

Figure 33: *The plain weaved cloth*. Warp and weft yarns (threads) are indicated. [168] 53

Figure 34: *The concentration of silicon in fibres*. The concentrations of Si measured with the PIGE method is higher than the values obtained by the PIXE method. 66

Figure 35: The trace elements in 12 different white PES textile fibres. 67

Figure 36: The trace elements of black PES and cotton textile fibres, plain and treated with Teflon. 68

Figure 37: The trace elements in white cotton textile fibres, plain and treated with silver.....69

Figure 38: PIXE spectrum from Si(Li) (a) and HPGe (b) detectors. The beam energy was 3.021 MeV, the proton dose was 1.36 μC, the time of measurement was 92.1 min, the resulting average ion-beam current was 0.25 nA. The Si(Li) detector had a 8 μm Be window, 10 nm gold layer and 0.75 μm Si dead layer without additional filters and the HPGe detector had a 25.4 μm thick Be window with 20 nm gold layer and 1.1 μm Ge dead layer with 100 μm Kapton filter. The target to crystal distance of Si(Li) detector was 3.5 cm at a 45° angle and for HPGe detector the distance was 3.1 cm at a 45° angle. Elements Cu and Zn were detected only with the HPGe detector.....71

Figure 39: Elemental maps of a white cotton fibre recorded in a vertical position, perpendicular to the beam and the detector direction. Maps were recorded at MIC, Ljubljana. 3 MeV proton microbeam with a diameter below 1.5 μm was used for the measurement. Dimension of a map is 400x400 μm. The geometrical effect can be observed in light elements maps. A part of the fibre, which is closest to the detector, has the strongest signal, due to the lower absorption of characteristic X-rays. This effect is most noticeable with light elements (Si and Al), where absorption in the material is strong. With increasing energy of characteristic Kα peaks (heavier elements) the geometrical effect diminishes. A STIM (scanning transmission ion microscopy) map shows us the silhouette of the fibre, from which we can determine the fibre width: 200±15 μm. There are two maps of chlorine, recorded with two different X-ray detectors, positioned left and right from the beam. Stronger signal is detected at the side of the fibre, which is closer to the detector, however the same effect is not noticeable with the titanium maps due to higher energy of characteristic Kα peaks (4.51 keV for Ti vs. 2.62 keV for Cl). Elemental distribution is mostly homogeneous, some hairiness, typical for natural plant fibres can be observed.....72

Figure 40: PIXE spectrum from Si(Li) (a) and HPGe (b) detectors. The beam energy was 3.021 MeV, the proton dose was 7.02 μC the time of the measurement was 244 min, the resulting average ion-beam current was 0.48 nA. The Si(Li) detector had a 8 μm Be window, 10 nm gold layer and 0.75 μm Si dead layer without additional filters and the HPGe detector had a 25.4 μm thick Be window with 20 nm gold layer and 1.1 μm Ge dead layer with 100 μm Kapton filter. The target to crystal distance of Si(Li) detector was 3.5 cm at a 45° angle and for HPGe detector the distance was 3.1 cm at a 45° angle. Kα peaks of detected elements are marked: Mg, Si, P, S, Cl, K, Ca, Ti, and Fe. The elements Mn, Ni, Cu, Zn and Sr were detected only with HPGe detector.....73

Figure 41: Elemental maps of three white cotton fibres, recorded in a horizontal position, perpendicular to the beam, but in the same plane as the detector axis. Maps were recorded at MIC, Ljubljana. 3 MeV proton microbeam with a diameter below 1.5 µm was used for the measurement. Dimensions of the map are 2x2 mm. Geometrical effect is seen in the maps of P, Cl an K as a pattern typical of two threads spun around each other; two diagonal dark lines, crossing the top two fibres. The third fibre is in the observed part more hairy than the other two, so the pattern is less pronounced. Huge difference in concentration between untreated fibre and the other two, treated fibres is observed in a potassium map. Less pronounced, but still a noticeable difference is in a chlorine and titanium map. Hairiness, typical for cotton and other natural plant fibres can be best observed in STIM and silicon map. Fibres are mostly homogeneous, with some particles (<20 µm) containing high amount of calcium or iron. Average width of the fibres obtained from the STIM map is 270±50 µm. 75

Figure 42: Non-Rutherford nuclear scattering cross-section for protons on helium, carbon and nitrogen. The vertical axis is in a logarithmic scale. [15]..... 76

Figure 43: Non-Rutherford nuclear scattering cross-section for protons on oxygen, fluorine and sodium. The vertical axis is in a logarithmic scale. [15] 77

Figure 44: Non-Rutherford nuclear scattering cross-section for protons on phosphorus, sulphur and argon. The vertical axis has a linear scale. [15] 77

Figure 45: Non-Rutherford nuclear scattering cross-section for protons on natural magnesium, aluminium and natural silicon. The vertical axis has a linear scale. [15] 78

Figure 46: Non-Rutherford nuclear scattering cross-section for protons on potassium, calcium and natural titanium. The vertical axis has a linear scale. [15] 78

Figure 47: *RBS spectrum of an 8 µm Al exit window*. The width of the Al foil "peak" depends on the actual width of the Al foil. A He resonance peak and a peak due to scattering in air behind the Al foil is also denoted. 79

Figure 48: *RBS spectrum of a 2 µm Ta foil.* The structure left of the Ta signal corresponds to air behind the foil. The fitted thickness is 2.35 µm (13000e15 at/cm^2). 83

Figure 49: *Medal of bravery produced for Yugoslav partisans in Russia in 1944-45.* The fitted thickness of the Au layer is 1.6 µm (9700e15 at/cm^2). [8]..... 83

Figure 50: Y*ugoslav medal of bravery produced in Yugoslavia after 1945.* The fitted thickness of the Au layer is 0.4 µm (2400e15 at/cm^2). [8] 84

Figure 51: *Modern Au plated commemorative medal from London.* The thickness of the Au layer is 42 nm (250e15 at/cm^2). The substrate is brass (alloy of Cu, Zn and Ni). The energy of the peak on the top of the slope corresponds very well to a 2000e15 at/cm^2 Cl in the layer between the Au and the substrate, but such a constitution is improbable and thus not fitted. 84

Figure 52: *Gilded artefact with a motive of Mary's annunciation.* Arrow shows the place of the proton impact. The thickness of the Au layer is 2.25 µm (13300e15 at/cm^2) with 11 at% Hg as a consequence of amalgamation. The fitted roughness FWHM is 1.86 µm (11000e15 at/cm^2). The substrate is bronze with traces of iron and silver. 85

Figure 53: *Sn layer on the top of copper substrate.* A fitted Sn layer thickness is 8.3 µm (30500e15 at/cm^2) and roughness FWHM is 2.7 µm (10000e15 at/cm^2). [8] 85
Figure 54: *Sn layer on the top of a copper substrate, annealed for 10 min at 250°C.* η phase (Cu_6Sn_5) and a thin layer of ε phase (Cu_3Sn) can be seen. The fitted Sn layer is 18.9 µm (70000e15 at/cm^2) and the roughness FWHM is 8.1 µm (30000e15 at/cm^2). A fitted η layer: 7.3 µm (27000e15 at/cm^2) and the roughness FWHM of 2.7 µm (10000e15 at/cm^2). [8] 86
Figure 55: *Tinned Roman brooch.* Arrow shows the place of proton impact. The effect of porosity of the top tin layer is seen. η layer: 10000e15 at/cm^2 (2 µm) and ε layer: 5000e15 at/cm^2 (1 µm). The arrow denotes the point of proton impact. [8] 86

Index of Tables

Table 1: *BCR® - 126A lead glass certified reference material*. The mass fraction of oxides contained in a glass standard, and its density at 20 °C. [163] 46
Table 2: *H value calibration*, performed on a lead glass BCR 126A at IBC, University of Surrey. 46
Table 3: *NIST 620 soda-lime flat glass certified reference material*. The mass fraction of oxides contained in a glass standard. [164] 47
Table 4: *H value calibration*, performed on a soda-lime glass NIST 620 at MIC. 47
Table 5: List of parameters and their influence on the absolute and relative results of the measurements, done at the University of Surrey. 51
Table 6: List of parameters and their influence on the absolute and relative results of the measurements, done at the Jožef Stefan Institute. 51
Table 7: *Table of the textile fibre samples*. Various cloths are denoted with number and separate yarns from it with letters. 54
Table 8: External (in-air) beamline comparison. 55
Table 9: PIXE measurements of textile fibres measured at the University of Surrey, concentrations in mass% were calculated with a cylindrical target model. 56
Table 10: PIXE measurements of textile fibres measured at the University of Surrey, concentrations in mass% were calculated with a ribbon target model with a square cross-section. 58
Table 11: PIXE measurements of textile fibres measured at the University of Surrey, ratio between the concentrations calculated with a ribbon target model vs. cylindrical target. 60
Table 12: *Gamma yield of the NIST 620 glass at two different distances from the exit window*. Measurements were performed at the Jožef Stefan Institute. 63
Table 13: PIGE measurements of textile fibres, done at University of Surrey, first run. The concentrations are in mass%. The beam was static with a Gaussian profile and a FWHM of 300 µm. The concentrations are calculated using Eqn 48. The concentrations in bold print are standard values. 64
Table 14: PIGE measurements of textile fibres, done at the University of Surrey, second run. The concentrations are in mass%. The beam was a homogeneous square of 1x1 mm. The concentrations are calculated using Eqn 49, where the width of a fibre was taken into account. The concentrations in bold print are standard values. 65
Table 15: *Calculation of the dose calibration factor.* Dead time was up to 30.6% for tantalum. 81
Table 16: *Calculation of the dose calibration factor, using careful calibration, measurements at a low count-rate.* The proton dose is determined with the wire-mesh charge integration, where each count is 1 nC. 82

Appendix: Personal bibliography for the period of 2003-20011

Original scientific article

1. MCGUINESS, Paul J., JEZERŠEK, David, KOBE, Spomenka, MARKOLI, Boštjan, SPAIĆ, Savo. 100-micrometer-thick Nd-Fe-B magnets for MEMS applications produced via a low-temperature sintering route. *J. magn. magn. mater.*. [Print ed.], October 2006, vol. 305, issue 1, str. 177-181.

2. ŠMIT, Žiga, JEZERŠEK, David, KNIFIC, Timotej, ISTENIČ, Janka. Pixe-PIGE analysis of Carolingian glass from Slovenia. *Nucl. instrum. methods phys. res., B Beam interact. mater. atoms*. [Print ed.], 2009, vol. 267, no. 1, str. 121-124, doi: 10.1016/j.nimb.2008.10.090.

3. ŠMIT, Žiga, STAMATI, F., CIVICI, N., VEVECKA-PRIFTAJ, A., KOS, Mateja, JEZERŠEK, David. Analysis of Venetian-type glass fragments from the ancient city of Lezha (Albania). *Nucl. instrum. methods phys. res., B Beam interact. mater. atoms*. [Print ed.], 2009, vol. 267, no. 15, str. 2538-2544.

4. JEZERŠEK, David, ŠMIT, Žiga, PELICON, Primož. External beamline setup for plated target investigation. *Nucl. instrum. methods phys. res., B Beam interact. mater. atoms*. [Print ed.], 2010, vol. 268, no. 11/12, str. 2006-2009.

5. JEZERŠEK, David, JAKOMIN, Sabina, ŠMIT, Žiga. Analysis of textile fibers by in-air PIXE. *Surf. interface anal.*, 2010, vol. 42, no. 5, str. 423-428.

6. KAVKLER, Katja, ŠMIT, Žiga, JEZERŠEK, David, EICHERT, Diane, DEMŠAR, Andrej. Investigation of biodeteriorated historical textiles by conventional and synchrotron radiation FTIR spectroscopy. *Polym. degrad. stab.*. [Print ed.], 2011, vol. 96, no. 6, str. 1081-1086, doi: 10.1016/j.polymdegradstab.2011.03.011.

7. ŠMIT, Žiga, JEZERŠEK, David, PELICON, Primož, VAVPETIČ, Primož, JERŠEK, Miha, MIRTIČ, Breda. Analysis of a chondrite meteorite from Slovenia. *X-ray spectrom.*, 2011, vol. 40, no. 3, str. 205-209, doi: 10.1002/xrs.1307.

Short scientific article

8. MCGUINESS, Paul J., JEZERŠEK, David, KOBE, Spomenka, SAJE, Boris. Microscale sintered magnets for MEMS type applications. *Powder Metall.*, 2006, vol. 49, str. 15-17.

9. ŠMIT, Žiga, JEZERŠEK, David, KNIFIC, Timotej, ISTENIČ, Janka. Raziskave zgodnjesrednjeveškega stekla z ozemlja Slovenije. *Argo*, 2010, [Letn.] 53, [št.] 1, str. 87-89, ilustr.

Published scientific conference contribution

10. JEZERŠEK, David, MIHELIČ, Matjaž, RUPNIK, Zdravko, ŠTUHEC, Matjaž, ZORKO, Benjamin. The new IJS MR200 TLD measuring system. V: KRAJCAR BRONIĆ, Ines (ur.), MILJANIĆ, Saveta (ur.), OBELIĆ, Bogomil (ur.). *Zbornik radova V. simpozija hrvatskog društva za zaščitu od zračenja [s međunarodnim sudjelovanjem, Stubičke Toplice, Hrvatska, 9.-11. travnja 2003]*. Zagreb: HDZZ-CRPA, 2003, str. 121-124.

11. MCGUINESS, Paul J., JEZERŠEK, David, KOBE, Spomenka, SAJE, Boris. 100-[mu]m-thick sintered magnets for MEMS-type applications. V: *Euro PM2005 Congress : 2-5 October, Prague, Czech Republic*. [S.l.]: EPMA, 2005, str. 427-432.

12. ZORKO, Benjamin, JEZERŠEK, David, ŠTUHEC, Matjaž, GOBEC, Sandi. Energy dependance of TL dosemeters using CaF[sub]2 : Mn pellets. V: GARAJ VRHOVAC, Verica (ur.), KOPJAR, Nevenka (ur.), MILJANIĆ, Saveta (ur.). *Zbornik radova VI. simpozija Hrvatskog društva za zaštitu od zračenja s međunarodnim sudjelovanjem, Stubiške Toplice, Hrvatska, 18.-20. travnja 2005*. Zagreb: HDZZ-CRPA, 2005, str. 97-104.

Published scientific conference contribution abstract

13. JEZERŠEK, David, MCGUINESS, Paul J., PODMILJŠAK, Benjamin, KOBE, Spomenka, PODMILJŠAK, Benjamin, KOBE, Spomenka. Ultra tanki sintrani in vezani magneti Nd-Fe-B za MEMS = Ultra-thin sintered and bonded Nd-Fe-B magnets for MEMS applications. V: JENKO, Monika (ur.). 13. konferenca o materialih in tehnologijah, 10.-12. oktober 2005, Portorož, Slovenija = 13th Conference on Materials and Technology, 10-12 October, 2005 Portorož, Slovenia. *Program in knjiga povzetkov*. Ljubljana: Inštitut za kovinske materiale in tehnologije, 2005, str. 39.

14. JEZERŠEK, David, KOBE, Spomenka, NOVAK, Saša, MCGUINESS, Paul J. Klub navdušencev nad projektom ITER - priložnost biti del mednarodne skupnosti za fuzijo = Unofficial ITER fan club - an opportunity to be a part of international fusion community. V: JENKO, Monika (ur.). 14. konferenca o materialih in tehnologijah = 14th Conference on Materials and Technology, 16-18 October, 2006, Portorož, Slovenia. *Program in knjiga povzetkov*. Ljubljana: Inštitut za kovinske materiale in tehnologije, 2006, str. 142.

15. JEZERŠEK, David, JAKOMIN, Sabina, ŠMIT, Žiga. Analysis of txtile fibers by in-air PIXE. V: CAARI 2008, 20th International Conference on the Application of Accelerators in Research & Industry, August 10 - 15, 2008, Fort Worth, Texas, USA. *Program & abstracts*. Denton: University of North Texas, 2008, str. 3.

16. ŠMIT, Žiga, JEZERŠEK, David, KNIFIC, Timotej, ISTENIČ, Janka. Pixe-PIGE analysis of Carolingian glass from Slovenia. V: CAARI 2008, 20th International Conference on the Application of Accelerators in Research & Industry, August 10 - 15, 2008, Fort Worth, Texas, USA. *Program & abstracts*. Denton: University of North Texas, 2008, str. 21.

17. JEZERŠEK, David, ŠMIT, Žiga, PELICON, Primož. External beamline setup for plated target investigation. V: 19th International Conference on Ion Beam Analysis, IBA 2009, 7-11 September 2009, Cambridge, UK. *Abstract book : celebrating 100 years of Rutherford Backscattering*. [S. l.]: Institut of Physics, 2009, str. 257.

18. ŠMIT, Žiga, STAMATI, F., CIVICI, N., VEVECKA-PRIFTAJ, A., KOS, Mateja, JEZERŠEK, David. Analysis of Venetian-type glass from Lezha, Albania. V: *Symposium program, book of abstract*. [S. l.: s. n.], 2009, str. 87.

19. JEZERŠEK, David. Use and application of ion beam analysis methods. V: ŠETINA, Barbara (ur.), JUNKAR, Ita (ur.), KALUŽA, Boštjan (ur.), ELERŠIČ, Kristina (ur.). 1. študentska konferenca Mednarodne podiplomske šole Jožefa Stefana, 19.-20. maj 2009, Ljubljana, Slovenija = 1st Jožef Stefan International Postgraduate School Student's Conference, 19th-20th May 2009, Ljubljana, Slovenia. *Zbornik prispevkov*. Ljubljana: Mednarodna podiplomska šola Jožefa Stefana, 2009, str. 24-25.

20. ŠMIT, Žiga, JERŠEK, Miha, JEZERŠEK, David, MIRTIČ, Breda, PELICON, Primož, VAVPETIČ, Primož. Analysis of a chondrite meteorite from Slovenia. V: 12th International Conference on Particle Induced X-ray Emission and its Applications, 27th June - 2nd July, 2010, Guildford, U. K. *Abstracts*. [S. l.: s. n.], 2010.

21. JEZERŠEK, David, BAILEY, Michael John, JEZERŠEK, David, ŠMIT, Žiga, PELICON, Primož, JEYNES, Chris, CHRISTOPHER, M. E., WARD, N. I., JAKOMIN, Sabina. Analysis of fibres for forensic applications. V: 12th International Conference on Particle Induced X-ray Emission and its Applications, 27th June - 2nd July, 2010, Guildford, U. K. *Abstracts*. [S. l.: s. n.], 2010.

22. JEZERŠEK, David, PELICON, Primož, GRLJ, Nataša, VAVPETIČ, Primož, ŽITNIK, Matjaž, ŠMIT, Žiga, ČADEŽ, Iztok, RUPNIK, Zdravko, MARKELJ, Sabina, PONGRAC, Paula, KAVČIČ, Matjaž. Upgrade of ion beam analysis at Jožef Stefan Institute and transnational access. V: KOKKORIS, M. (ur.), MISAELIDES, Panagiotis (ur.). ECCART 10, 10th European Conference on Accelerators in Applied Research and Technology, Athens, Greece, September 13-17, 2010. *Book of abstracts*. [S. l.: s. n.], 2010.

23. JEZERŠEK, David, ŠMIT, Žiga. Recent upgrade of the external beamline at MIC. V: KALUŽA, Boštjan (ur.), ELERŠIČ, Kristina (ur.), POGORELC, Bogdan (ur.), ŠETINA, Barbara (ur.), VAHČIČ, Mitja (ur.). 2. študentska konferenca Mednarodne podiplomske šole Jožefa Stefana = 2nd Jožef Stefan International Postgraduate School Students Conference, 27. maj 2010, Ljubljana, Slovenija. *Zbornik prispevkov*. Ljubljana: Mednarodna podiplomska šola Jožefa Stefana, 2010, str. 54.

Treatise, preliminary study, study

24. ŠTUHEC, Matjaž, MIHELIČ, Matjaž, JEZERŠEK, David, ZORKO, Benjamin, GOBEC, Sandi. *Validation of the TLD IJS MR 200 (C) measuring system : laboratorij za termoluminiscenčno dozimetrijo*, (IJS delovno poročilo, 9031). 2004.

25. ZORKO, Benjamin, GOBEC, Sandi, ČRNIČ, Boštjan, JEZERŠEK, David, MIHELIČ, Matjaž, ŠTUHEC, Matjaž. *Validation of the TLD IJS MR 200C (3) measuring system*, (IJS delovno poročilo, 9519). 2007.

Unpublished conference contribution

26. ŠMIT, Žiga, KNIFIC, Timotej, JEZERŠEK, David, ŽITNIK, Matjaž, ISTENIČ, Janka. Analysis of early medieval glass beads : glass in the transition period : presented at CAARI 2010, 21st International Conference on the Application of Accelerators in Research & Industry, August 8-13, 2010, Fort Worth, Texas, USA. 2010.